

1

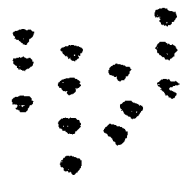
AD-A237 458



# Hamiltonian 3-D Ray Tracing in the Oceanic Waveguide on the Ellipsoidal Earth

by J. George Dworski and James A. Mercer

Technical Report  
**APL-UW TR 8929**  
December 1990



*ONR Grant N00014-89-J-1979*

**91-03779**



*Approved for Public Release - Distribution is Unlimited*

# Hamiltonian 3-D Ray Tracing in the Oceanic Waveguide on the Ellipsoidal Earth

by J. George Dworski and James A. Mercer

Accession For	
NTIS GRAB	<input checked="" type="checkbox"/>
DTIC TAB	<input type="checkbox"/>
Unannounced	<input type="checkbox"/>
Justification	
By	
Distribution/	
Availability Codes	
Dist	Avail and/or Special
A-1	

Technical Report  
**APL-UW TR 8929**  
December 1990



**Applied Physics Laboratory University of Washington**  
**Seattle, Washington 98105-6698**

*ONR Grant N00014-89-J-1979*

*Approved for Public Release – Distribution is Unlimited*

*Acknowledgments*

*This research was supported by the Office of Naval Research, Code 11250A, Marshall Orr.*

## ABSTRACT

Ray equations based on an acoustic Hamiltonian, and formulated by Jones et al. (1986) for spherical coordinates in NOAA's 3-D ray tracer HARPO, are adapted to ellipsoidal coordinates in the oceanic waveguide. The ensuing modified HARPO is used to model very long range (up to antipodal) acoustic paths in which the difference between geodesics and great circles is measurable. The eventual objective of this modeling is to extract the predictable part of the travel-time trend and fluctuations along several long paths that will be used to monitor hypothetical global warming effects. The requirements for easy assimilation and representation of realistic environmental inputs are discussed. These requirements, when coupled with the possibility of classical chaos in the ray paths, dictate a new software architecture. We use the existing software, however, to breadboard and test features of new ray tracers in the global boundary layer, and to support the experimental design of a forthcoming pilot experiment that will use a transmitter located at Heard Island in the Indian Ocean near Antarctica. A path of particular interest links Heard Island, through the Tasman gap, to the Washington-Oregon Coast in the northeast Pacific. A 3-D sound speed model is formulated for the Indian/Pacific Ocean in the region of this path, and a 3-D antarctic circumpolar current model with 180 Sverdrup transport is specified to cross the path. Eigenrays are computed to within 2 m error on 18 Mm in the presence and in the absence of currents. We draw conclusions specific to the acoustic communication channel on this path. In particular, we infer a significant out-of-(geodesic)-plane deflection (of about 500 km) of the acoustic eigenpaths. This 3-D deflection is due to the thermohaline structure and can be quantified, at the present time, only by ray tracing.

TABLE OF CONTENTS

	<i>Page</i>
1. Introduction .....	1
Section Preview .....	4
2. Earth Coordinates and the 3-D Hamiltonian Formalism .....	4
What "Fully" 3-D Means to Ray Tracing .....	4
Global and Local Coordinates .....	4
How to "Flatten" the Earth's Curvature .....	5
Beyond the Flat Earth: The Perfect Sphere.....	5
Beyond the Sphere: The Ellipsoid.....	5
The Oblate Spheroid.....	6
Relations Between Spheroidal Coordinates .....	8
Numerical Geometry of the Ellipsoid .....	9
Approximations .....	9
What Latitude?.....	9
Which Radius?.....	10
Azimuthal Steering on the Spheroid .....	13
Horizontally Refracted Geodesics on the Spheroid .....	14
Antipodal Acoustic Paths on the Spheroid .....	14
Hamiltonian.....	18
3. Indian/Pacific Sound Speed Model and the Antarctic Circumpolar Current Model.....	20
Sound Speed Model.....	21
Circumpolar Current Model.....	31
4. General Modeling Results and the Specific Eigenpaths to a Receiver Near Coos Bay, Oregon .....	33
Eigenpaths .....	36
The "Ridge" Concept.....	42
5. Discussion.....	48
Perspective .....	48
The "Classical" Chaos.....	51
Technical Results.....	54
Software Considerations .....	54
Geophysical.....	55
Oceanographic .....	57
References.....	59

Appendix A, Reduced Dimensionality Ray Tracers and the Hamiltonian..... A1-A5  
Appendix B, Effective Axis of Sound Channel..... B1-B5

## LIST OF FIGURES

	<i>Page</i>
Figure 1. Geodesics bounding the westward Atlantic window from Heard Island .....	2
Figure 2. Geodesics bounding the Tasman and Polynesian eastward windows from Heard Island .....	3
Figure 3. Coordinate surfaces on the spheroid and a cross section through the rotational axis.....	7
Figure 4. Deviations of $r_m$ and of $r_v$ from $\bar{r}$ as a function of latitude.....	12
Figure 5. Geodesics from a location south of Perth .....	16
Figure 6. The actual pattern of geodesics in the vicinity of the Atlantic antipode.....	17
Figure 7. Image of the analytical sound speed model used for modeling propagation through the Tasman window as a function of latitude.....	23
Figure 8. Sample sound speed profiles for the Tasman window indexed by latitude and offset by 20 m/s from one another .....	25
Figure 9. A canonical sound speed profile and its partial derivatives with respect to $H_c$ and $\epsilon$ .....	27
Figure 10. Canonical parameters $H_c$ and $\epsilon$ as a function of latitude.....	28
Figure 11. Tasman window sound speeds at the surface, channel axis, and 4400 dbar depth as function of latitude .....	29
Figure 12. Tasman window sound channel axis depth versus latitude .....	30
Figure 13. The Antarctic Circumpolar Current versus depth .....	32
Figure 14. The surface projection of an eigenpath through the Tasman window and corresponding geodesic and great circle paths.....	34
Figure 15. Vertical oscillations of the Tasman eigenpath, with an elevation angle of $-1.6148^\circ$ , along the 18,000 km path .....	35
Figure 16. Average zonal wind stress and wind stress curl for the month of July 1979 .....	37
Figure 17. Vertical oscillations of the Tasman eigenpath, having an elevation angle of $0^\circ$ , along the 18,000 km path.....	38
Figure 18. The initial elevations and azimuths of 16 search rays and 4 corresponding eigenrays through a Tasman window with circumpolar current.....	41
Figure 19. Positions at which various rays pass through the depth of the receiver in the vicinity of the receiver .....	44

Figure 20.	Blowup of the insert area from Fig. 19 showing the cut set for ridge number 917 at elevation angles of $-1.6^\circ$ and $-1.7^\circ$ .....	45
Figure 21.	Along-path miss distance versus initial elevation angle for ridge numbers 917 through 920.....	47
Figure 22.	Cross-path miss distance versus initial elevation angle for ridge numbers 917 through 920.....	49
Figure 23.	Initial elevations and azimuths of 16 search rays and 4 corresponding eigenrays through a Tasman window without the circumpolar current .....	50
Figure 24.	Reduced travel time comparison of eigenrays with and without the circumpolar current .....	56
Figure A1.	Cartesian and cylindrical coordinate ray parameters .....	A3
Figure B1.	Example of ray trajectory during the first 1000 km (a) and near 20,000 km (b).....	B3

## 1. Introduction

An acoustic feasibility experiment for long-term monitoring of global warming trends is planned for January 1991. The concept for this remote sensing project, related to very long range acoustic tomography, is described by Munk and Forbes (1989) and is summarized by Gibbons (1990). The single transmitter will be at Heard Island (53.5°S, 73.5°E) in the southwestern Indian Ocean. The listening receivers will be located in several oceans and at several distances (at megameter ranges) from the transmitter. Windows for three of the longest paths are westward from Heard Island to the Atlantic Coast of North America and eastward from Heard Island to the US West Coast. The (unrefracted) geodesics that bound these three windows are shown in Figs. 1 and 2. The westward, "Atlantic," window has the widest azimuthal aperture, 20°; the two eastward windows ("Tasman" and "Polynesian") have apertures of 8° each.

The aperture of the westward window is bounded by Brazil and West Africa. Sound transmitted from Heard Island has unobstructed access to receivers along a wide swath of the northwest Atlantic Ocean between Nova Scotia in the north and Virginia in the south. Acoustic signals on a more complicated and longer path, from Perth to Bermuda, were measured during a history-making 1960 experiment. Interpretation of these measurements was given by Schockley et al. (1982) and Munk et al. (1988).

The main eastward window is azimuthally limited to the "Tasman Gap," an opening between Tasmania and North Island of New Zealand. It may be further limited by bathymetric barriers created by the Western Polynesian Islands or the Hawaiian Islands. A relatively narrow stretch of the continental slope along the North American Pacific coast off Washington and Oregon seems to be suited for locating receivers.

The other eastward window is bounded by Wilkes Land (west of Adélie Coast) in Antarctica and South Island of New Zealand. Acoustic paths sweep around New Zealand, pass through the Polynesian Archipelago, and reach the continental slope off California.

While the geographical "choke" points that bound these three sets of paths are reasonably well identified, the stretches of continental slopes in the northwest Atlantic and northeast Pacific, where we expect favorable listening conditions, can be adequately identified only by modeling the refracted acoustic paths.

These are some of the longest underwater propagation paths on the globe. When modeled with realistic, nonsmooth, oceanic features of the sound speed and ocean current fields, computed ray paths over such long distances may exhibit chaotic behavior similar to that described by Palmer et al. (1988). Chaos, in the analytical and computational sense, is suppressed by smoothness in the representation of the ocean, but this suppression degrades the realism of the model. Chaos is accentuated by dimensionality of the model, in that 3-D trajectories are much more prone to exhibit chaos than 2-D trajectories. But 3-D modeling enhances the realism and resolving power of the model. Hence the model design criteria are conflicting. We have paid attention to this important topic in the Discussion (Section 5), and have interspersed throughout the text considerations that will facilitate development of "2-D+" boundary layer ray tracers for use with nonsmooth ocean data. However, our computed results are obtained with a 3-D Hamiltonian ray tracer in a moderately smooth ocean, and they do not exhibit any sign of exponential sensitivity to initial conditions even at the extreme range of 18 Mm.

In the work reported here, our objective was to explore fundamental propagation conditions along the "Tasman" path and develop modeling software to support and interpret the

Heard Island feasibility and long-term acoustic monitoring experiments.

A SOFAR acoustic propagation path from Heard Island through the Tasman Gap to the US West Coast is viable (in the ray approximation) if the SOFAR axis is not obstructed by bathymetry. We do not address bathymetry effects in this report, and we assumed the viability of a Tasman path from the results of Munk and

Forbes (1989)—their Fig. 6. Our own analysis of the SOFAR geometry along the hypothetical Tasman path has shown their Fig. 6 to be in error, and this puts the viability of a Tasman SOFAR path into question. Therefore, the computed results that we present for propagation along the Tasman path are more appropriate for illustrating modeling techniques than for drawing geophysical inferences.

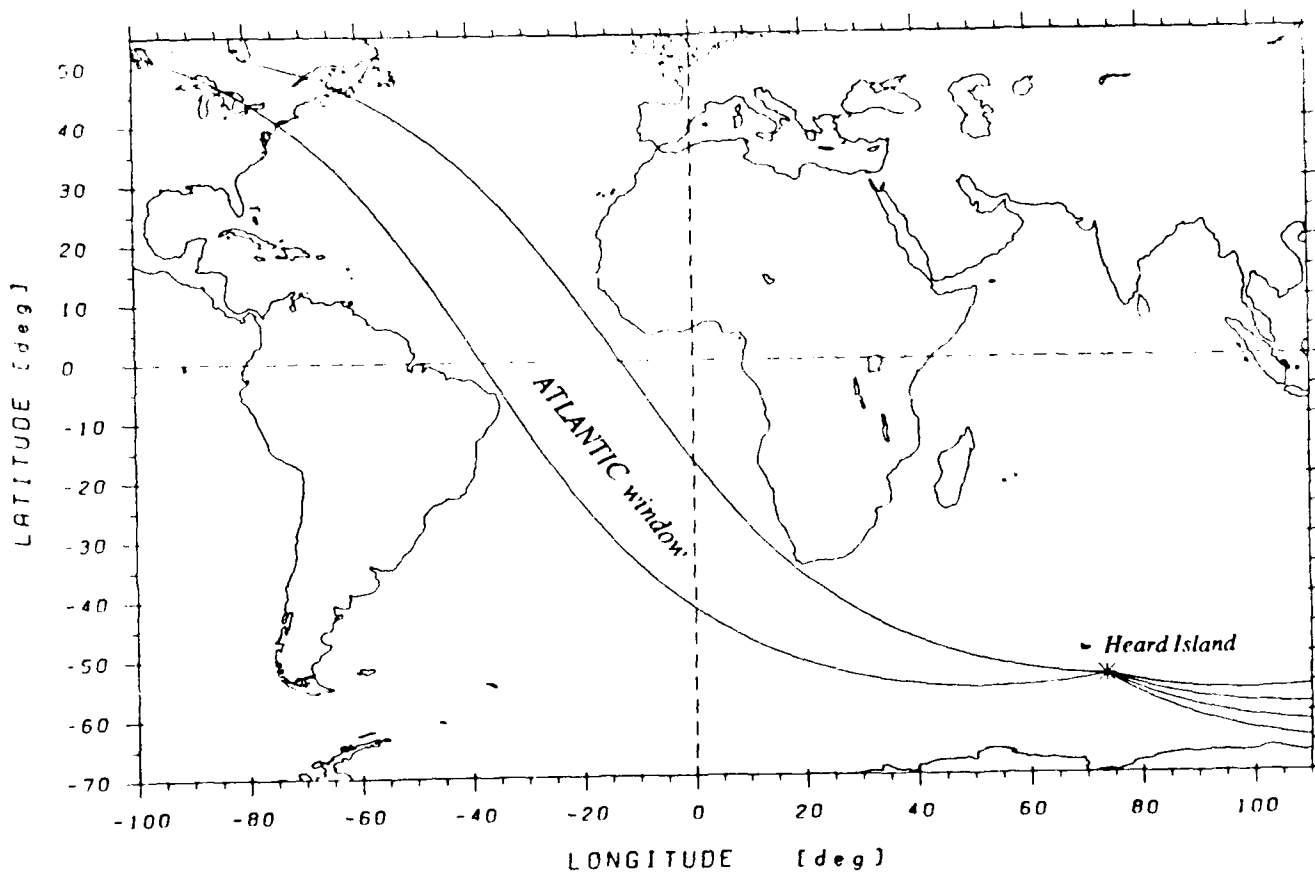


Figure 1. Geodesics bounding the westward Atlantic window from Heard Island.

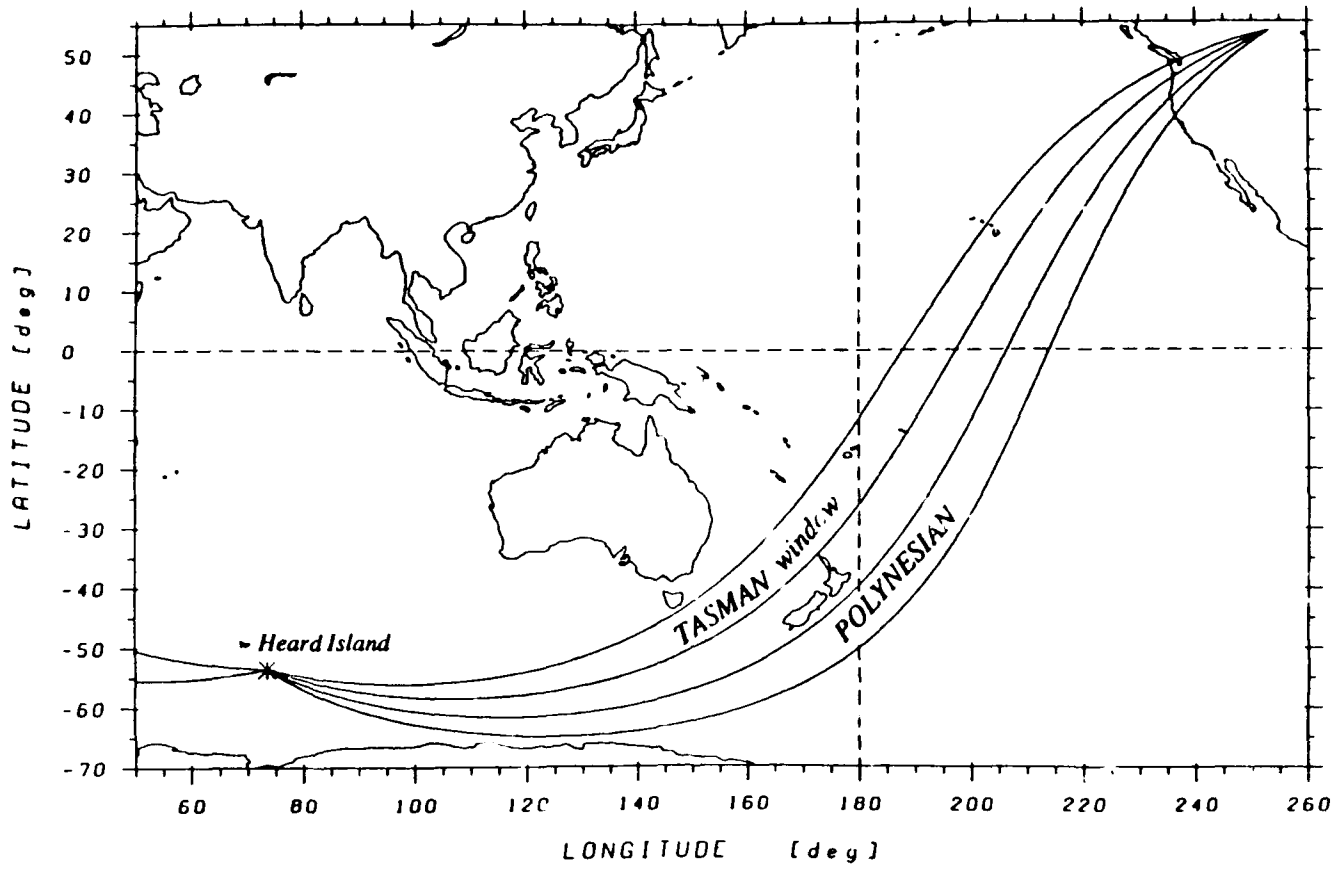


Figure 2. Geodesics bounding the Tasman and Polynesian eastward windows from Heard Island.

### *Section Preview*

Section 2 is the main body of this report. It addresses geodesic considerations and the Hamiltonian formalism. Section 3 describes the models used to represent the sound speed structure of the Indian/Pacific Ocean and the flow field of the Antarctic Circumpolar Current. Section 4 presents general modeling results and specific eigenpaths to an arbitrary point near Coos Bay, Oregon. Section 5 is a discussion of our conclusions and touches on considerations for the design of new modeling software.

## **2. Earth Coordinates and the 3-D Hamiltonian Formalism**

Experience with three-dimensional underwater acoustic ray tracing over ranges on the scale of one radius of the earth, or larger, is very recent and not generally available from the literature. When reported, the results are typically based on substantial simplifying assumptions.

### *What "Fully" 3-D Means to Ray Tracing*

The results shown here were obtained from fully 3-D models, and it is important to clarify what is meant by that. Ray paths that are confined to a (general) cylindrical surface (with a vertical generatrix) are 3-D, but they are *not* "fully 3-D" because they are confined to a surface. This surface is "ruled"; i.e., it is particularly simple and regular. The directrix (the curve through which the generatrix always passes) of such a cylinder is a great circle, a geodesic, or a refracted geodesic. The particular type of directrix depends on the sophistication of the given model, but all types have this in common: at all "down-range" points, the ray paths have the same azimuth regardless of their launch elevation angle. The converse is also true. When the rays launched with the same azimuth, but different launch elevation angles,

exhibit different azimuths at an arbitrary down-range point, then the corresponding ray paths could not have been confined to a ruled cylindrical surface; these ray paths are fully 3-D.

How important is the "fully 3-D" ray tracing? Lynch (1990) reports that the out-of-plane refraction effects are small, except when the ray paths get deflected from the cylindrical surface by reflection (from bathymetry) or by strong but spatially uneven refraction. We concur.

Specifically, the propagation geometry of paths that oscillate only a few hundred meters in the vertical (about the sound channel axis) can be thought of as effectively confined to a single cylindrical surface. A horizontally refracted geodesic is a good modeling directrix for this cylinder. Nonetheless, we will show that even for such paths our stringent eigenray tolerances cannot be met without capturing the azimuthal deviations caused by out-of-plane refraction.

The "fully 3-D" modeling that we actually used may be much more important for rays that oscillate vertically several kilometers, but we have not modeled such rays.

### *Global and Local Coordinates*

In underwater acoustics, there is a geometrical advantage in that the ocean is a thin, sharply bounded waveguide with a thickness less than 1/1000 of the earth's radius. This nearly decouples any local reference system from a global reference system. In this context "local" is logically related to "vertical," and "global" to the "horizontal" extent of the propagation path.

To focus attention to the issues, visualize a "flat earth" modeling (i.e., without embedding curvature terms into the ray equations) of underwater propagation on a spherical earth to, say, 6000 km range. We stress the existence of two types of errors. The first would be the inability of the modeled ray paths to curve horizontally

along a great circle route—an inability caused by the intrinsic lack of azimuthal control. As a result, the modeled sound paths would encounter waters of substantially different properties, and this would cause travel-time errors in addition to the errors due to the misrepresented geometry.

The second error type of the "flat earth" model is due to the earth's curvature and occurs in the vertical section. It is self-evident there, but one should keep in mind that the computed underwater sound paths, just like the actual ones, cannot escape the oceanic waveguide no matter how bad the representation of the propagation geometry. The modeled sound will reach the targeted distance with some, but not catastrophic, error in arrival time.

The "horizontal" error can be attributed to an inadequate *topology* of the Cartesian system in the global context of the problem. The "vertical section" error reflects accumulation of errors due to an inadequate *metric* of the Cartesian system in the local context. We note that mathematicians would call both deficiencies of the Cartesian system "metric" in the spherical context, but we use the term "topological" to emphasize a difference in the overall shape of the propagation paths. In the horizontal and on a large scale this difference would be quite discernible, but in the vertical the correct and the erroneous paths would look reasonably alike on a large scale, as they zigzag between the sea surface and the ocean bottom.

#### *How to "Flatten" the Earth's Curvature*

Both types of errors are associated with the earth's curvature. Actually, only the second was recognized early; it was dealt with using approximations that were appropriate given the questions asked and the computational limitations at the time.

For ranges up to one earth radius, the second (vertical) effect of earth's curvature can be reasonably accounted for by introducing a

number of "earth flattening" devices. The best known among them was introduced by Booker and Walkinshaw in 1946. It is a *modified index* of refraction, and the computing is still done in a Cartesian system. The validity of the ensuing approximation has been analyzed by Brekhovskikh (1960), and by Budden (1961; 1988) for radio waves in the ionosphere.

In underwater acoustics, the sound speed profile can be adjusted to compensate for the earth's curvature. This has been done by Weinberg (1981) in the Generic Sonar Model (GSM), closely paralleling the modified index idea.

The practice of modifying the medium's description to avoid dealing with more complex coordinates is probably waning. Brekhovskikh no longer refers to it in 1980. The GSM models a layered (range-independent) medium, and this limits the distances of practical interest.

#### *Beyond the Flat Earth: The Perfect Sphere*

Most long distance ray tracing near and below the earth's surface is now done in spherical coordinates. This removes both topological and metric errors as long as the spherical representation is considered to be sufficient for the problem at hand. Among the models that use spherical coordinates in underwater acoustics are the already mentioned HARPO by Jones et al. (1986) and its extension (HARPO-MOD1) by Lynch (1990). An overview of numerical ocean acoustic propagation in three dimensions is expected soon in book form, from Lee (1990).

The ray trace equations for spherical coordinates are published in a number of texts and papers, but rarely as completely and computationally oriented as in Jones et al. (1986). An accessible account of ray tracing in spherical coordinates, as used in seismic work a decade ago, is given by Aki and Richards (1980).

#### *Beyond the Sphere: The Ellipsoid*

The use of a 3-D spheroidal coordinate system, and approximations to it, must be

motivated by need—the need being to eliminate the error due to the horizontal lay of acoustic Fermat paths over very long distances if they are modeled as great circles. The latter is, of course, directly linked to ray path computations in a spherical coordinate system. At long propagation ranges, the lay of Fermat paths is systematically different on an ellipsoid (spheroid) than on a sphere. Implications of this fact were thoroughly analyzed by Munk et al. (1988).

The longest paths for underwater sound on this planet must involve the southern, near-Antarctic, Indian Ocean no matter how high the latitude of a receiver or transmitter in the North Atlantic or North Pacific. The intrinsic ellipsoidal topology causes the true Fermat path at such ranges to always project "south" of the corresponding great circle path. This argument is based on differential geometry, but remains valid in the presence of arbitrary lateral gradients of the sound speed field along the path.

An oceanographic consequence of this systematic deviation is that sound will traverse through "colder" (slower) waters than it apparently would have if the propagation had been modeled in spherical coordinates. Hence the interest of Munk et al. (1988), as well as Munk and Forbes (1989), in identifying the need for modeling propagation as close as topologically practical to the geometry of the planet.

The following discussion addresses details of the geometrical concepts related to the coordinate system. The salient points are

- The earth's ellipsoid offers a better topology for modeling long range propagation than does a sphere.
- The ellipsoid has a weak eccentricity, and its metric is not very different from that of a sphere.
- The ellipsoidal coordinates are more complex than the spherical ones. The differential operators have more terms and have the eccentricity implicitly embedded in a complicated way. If they are evaluated at every

integration step, they may become a computational monster, but if omitted the coordinate system becomes an approximation.

- The ocean *data* no longer possess the customary structure if they are to be strictly represented in the ellipsoidal coordinates. For example, data given at a constant depth, but different position, no longer have the same ellipsoidal "shell" coordinate.
- The maximum ratio of vertical ray path displacement in the 5–6 km ocean depth to the earth radius is small (less than  $1 \times 10^{-3}$ ), and the relative change in the spheroid's eccentricity over this displacement is equally small. This permits a local representation of data (depth can be used instead of the ellipsoidal shell thickness), and the inherently local (differential) computation of ray position can be accurately based on the depth coordinate, as will be shown in the discussion on the radii of curvature.

### *The Oblate Spheroid*

The earth's spheroid, or ellipsoid, is mathematically classified an *oblate spheroid*. This shape is an ellipsoid of revolution, revolving about its minor axis. It possesses less symmetry than a sphere and thus has more complicated relations between its coordinates. Figure 3(a) (adapted from Baier, 1972) gives a good 3-D picture of the coordinate surfaces on the spheroid. The surfaces labeled  $u_3 = \text{const}$  are the "radial" shells, and the hyperboloidal mantle surfaces  $u_2 = \text{const}$  are "latitudes." The coordinate surfaces  $u_1 = \text{const}$  are planes through the axis of rotation and are defined as "meridians."

A cross section through the rotational axis of such an ellipsoid is shown in Fig. 3(b). The meridional surfaces are no longer shown. Traces of the  $u_2 = \text{const}$  surfaces (constant latitudes) are hyperbolas, and they must be orthogonal to the  $u_3 = \text{const}$  shells (though they are not shown as such in this textbook sketch).

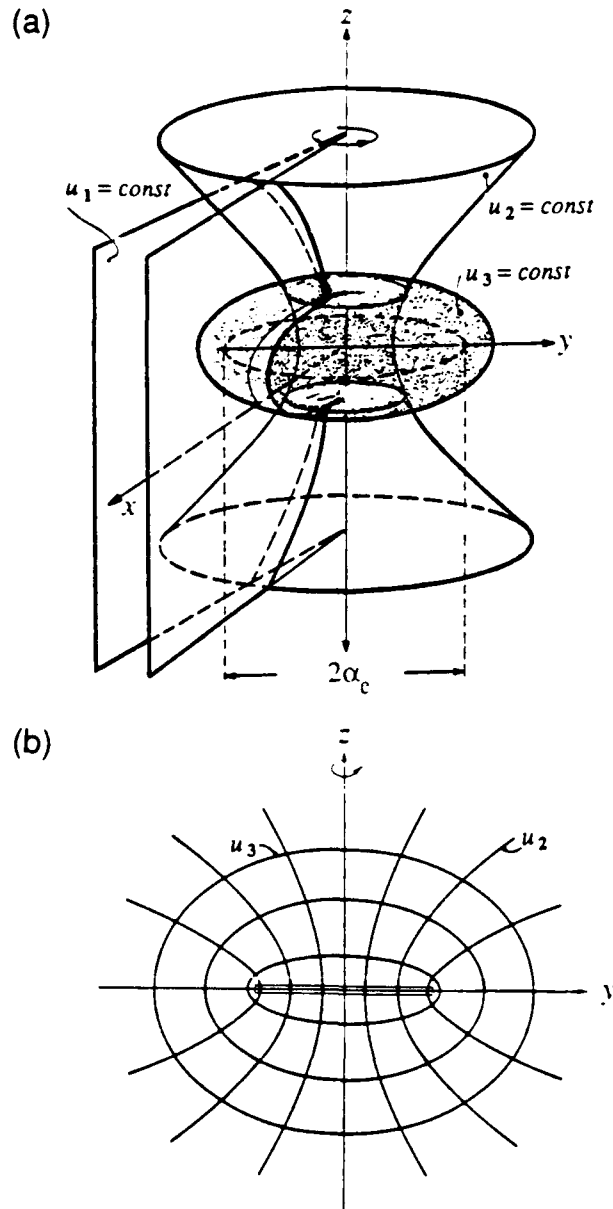


Figure 3. (a) Coordinate surfaces on the spheroid [from Fig. 1 in "Acoustic radiation impedance of caps and rings on oblate spheroidal baffles" by R.V. Baier, *J. Acoustic So. Am.*, 51(5): 1705-1716, 1972]; (b) a cross section through the rotational axis [from Fig. 2.12 in *Mathematical Methods for Physicists (2nd ed.)* by George Arfken, copyright 1970 by Academic Press, New York].

Details about these coordinates can be found in Arfken (1970) (from which Fig. 3(b) was drawn), or from Morse and Feshbach (1953) in even greater detail. Both works use a left-handed system in ordering the triplets ( $u_3, u_2, u_1$ ), and we retain it (cyclically permuted when necessary).

When attention is confined to the surface of the spheroid,  $u_3$ , then the geodesic literature offers a wealth of detailed and specialized information (e.g., Bomford (1980), Zakatov (1962), and Jordan et al. (1965)). The relations of direct interest for long range acoustic propagation are not too readily extracted from that literature, so they will be quoted or derived below for ease of reference.

*Relations Between Spheroidal Coordinates*

The coordinates of an oblate spheroid are usually found in two forms. One (Fig. 3) employs the left-handed orthogonal triad  $\{u_3, u_2, u_1\}$ , for which one can express the right-handed Cartesian triad  $\{x, y, z\}$  in terms of hyperbolic functions of  $u_3$  and trigonometric functions of  $u_2$  and  $u_1$ . This form is given by Morse and Feshbach and by Arfken.

The other, completely equivalent form is more algebraic (Madelung, 1957). It employs the left-handed orthogonal triad  $\{\lambda_3, \lambda_2, \lambda_1\}$ . It also results in notationally simpler differential expressions. This is helpful while inspecting derivations; e.g., left-handedness of the curvilinear coordinate triads can be tracked by applying a minus sign to the  $\nabla \times$  operator.

The following equivalences hold (cf. Fig. 3):

$$\begin{aligned} \lambda_3 &= \sinh u_3 \\ \lambda_2 &= \sin u_2 \\ \lambda_1 &= u_1. \end{aligned}$$

Ranges of the arguments as well as the interpretations of surfaces generated by them are

- The surfaces

$$u_3 = \text{const}, 0 \leq u_3 < \infty$$

are oblate spheroidal shells (so that  $u_3$  partly describes a "radial" distance to the shell's surface).

- The surfaces

$$u_2 = \text{const}, -\pi/2 \leq u_2 \leq \pi/2$$

are one-shelled hyperboloids. A limiting (and degenerate) case is the equatorial plane,  $u_2 = 0$ . The coordinate  $u_2$  becomes, by definition, the *geodetic latitude*,  $\chi$ .

- The surfaces

$$u_1 = \text{const}, 0 \leq u_1 \leq 2\pi$$

are half planes through the  $z$  axis (the axis of rotation), and  $u_1$  is identical to the *geodetic longitude*,  $\phi$ .

Relations of these curvilinear coordinates to the Cartesian coordinates are

$$\begin{aligned} x &= \alpha_e \cosh u_3 \cos u_2 \cos u_1 \\ &= \alpha_e (1 + \lambda_3^2)^{1/2} (1 - \lambda_2^2)^{1/2} \cos \lambda_1; \quad (1) \end{aligned}$$

$$\begin{aligned} y &= \alpha_e \cosh u_3 \cos u_2 \sin u_1 \\ &= \alpha_e (1 + \lambda_3^2)^{1/2} (1 - \lambda_2^2)^{1/2} \sin \lambda_1; \quad (2) \end{aligned}$$

$$\begin{aligned} z &= \alpha_e \sinh u_3 \sin u_2 \\ &= \alpha_e \lambda_3 \lambda_2. \quad (3) \end{aligned}$$

The proportionality factor  $\alpha_e$  is obtained by elimination of coordinates, using the following geometrical facts: the smaller axis,  $b$ , of the spheroid satisfies  $z^2 = b^2$  for  $\lambda_2 = 1$ , and the larger axis,  $a$ , satisfies  $x^2 + y^2 = a^2$  for  $\lambda_2 = 0$ . Therefore,  $\alpha_e^2 = a^2 - b^2$ , and  $\alpha_e$  has a geometrical interpretation as the radius of the "focal circle" of the oblate spheroid in the equatorial plane (Fig. 3(a)).

The geocentric radius (distance from the origin to a point on any of the spheroidal shells) is important for the metric properties of

approximate computations involving the earth's ellipsoid; it is given by

$$\begin{aligned} \rho_g^2 &= x^2 + y^2 + z^2 \\ &= \alpha_e^2 (\lambda_3^2 - \lambda_2^2 + 1). \end{aligned} \quad (4)$$

*Numerical Geometry of the Ellipsoid*

A frequently used configuration of the earth's ellipsoid is parameterized by definitions of the WGS 84 (Department of Defense World Geodetic System 1984) spheroid, and we use it here in our text. However, most of the computed results used parameters from the predecessor WGS 72. The 72 spheroid is negligibly different from the 84 (its major semiaxis is shorter by 2 m, and its "flatness" is smaller by  $3 \times 10^{-8}$ ). Two parameters are sufficient to define the geometry: the major semiaxis length  $a = 6378.137$  km and the dimensionless flatness

$$f = 1/298.2572 .$$

From  $a$  and  $f$  one obtains the minor semiaxis  $b = a(1-f)$ , and the "first" or "major" eccentricity squared  $e^2 = f(2-f) = 1/149.3790$ . Note that all ellipsoids in use so far (e.g., Bessel (1841), Clarke (1866), International, or Hayford (1924)) have their ellipticity described within limits of the approximations  $f \approx 1/300$  and  $e^2 \approx 1/150$ .

The following identities

$$(1-f)^2 \equiv 1-e^2 \equiv (b/a)^2 , \quad (5)$$

in conjunction with Eqs. (1) through (4), yield a definition of the earth's oblate spheroid terms:

$$\alpha_e^2 = a^2 e^2 \quad (6a)$$

$$\lambda_{3_0}^2 = \frac{1-e^2}{e^2} \quad (6b)$$

$$\mu_0 = \sinh^{-1} \lambda_{3_0} . \quad (6c)$$

where the subscript 0 indicates the parameter value at the earth's surface. Using the numerical parameters of WGS 84, one obtains

$$\alpha_e = 521.85400842262 \text{ km} \quad (7a)$$

$$\lambda_{3_0} = 12.18109320164 \quad (7b)$$

$$\mu_0 = 3.1947128 . \quad (7c)$$

The extended precision of values in Eq. (7) is carried along solely for checking the integrity of the approximate computations; their accuracy depends on the accuracy of the ellipsoidal axis  $a$  (seven significant digits) and the flattening  $f$  (about seven significant digits). The parameters for our earth's oblate spheroid, Eq. (7), could not be found in the topical literature, probably because geodesy (including the physical one) does not find much use for the earth's geometrical ellipsoid at any distance below the sea surface. However, the oblate spheroidal coordinates are useful in geophysical contexts, spurred by the use of earth-orbiting satellites (Vinti, 1959).

*Approximations*

In our application, the fundamental shape parameters of Eq. (7) are essential for high resolution checks on the accuracy of approximate computations when ray paths dip a few kilometers below the sea surface.

A few qualitative arguments will introduce the approximations relevant to the global oceanic boundary layer. It is evident from Fig. 3(b), and Eqs. (1) through (3), that constant latitude surfaces on the spheroid do not intersect the rotational axis, unlike the constant latitude surfaces on the sphere where they are cones with a single vertex at the earth's center. More importantly, the local normal to any  $\lambda_3 = \text{const}$  shell, tangential to a  $\lambda_2 = \text{const}$  surface, does intersect the rotational axis but not at the earth's center.

*Which Latitude?*

In geodesic terminology, the discussion above gives rise to two latitudes, the geocentric latitude

$$\psi = \tan^{-1} [z / (x^2 + y^2)^{1/2}],$$

and the geodetic latitude,  $\chi$ , introduced previously. They are related by

$$\tan\psi = (1 - e^2) \tan\chi,$$

which shows that  $\chi > \psi$  everywhere except at the poles and the equator where they have equal values. The difference between them is largest at latitude  $45^\circ$  where the angle is  $11'33''$ . In acoustic propagation modeling this difference can be interpreted as a departure from the "vertical" that affects the given data fields (though the concepts of vertical and normal have very precise references that are of no concern here). In that sense it is a negligible difference. We do not distinguish between the two latitudes, though we do follow the more common practice and preferentially use the geodetic latitude,  $\chi$ .

#### Which Radius?

A second point evident in Fig. 3(b) is that while the earth's surface is associated with the constant value of the spheroidal coordinate  $\lambda_{3_0}$ , which would conventionally be the "radial" coordinate in a spherical analogue, the ellipsoidal earth's surface is obviously not associated with the same value of the *geocentric* radius, Eq. (4), at arbitrarily chosen surface points. In the pure spherical system, all surface points have the same geocentric point-radius. The neighborhood of each point has a unique radius of curvature (identically equal to the point-radius, and with a center coinciding with the point-radius origin) that is independent of direction (azimuth) along the surface.

The situation is more complicated in the spheroidal system. Consider a general ray point at a given depth below the ocean surface along the acoustic propagation path. To get a handle on consistent differential changes, one derives the *total differential* of any 3-D path:

$$ds^2 = \alpha_e^2 \frac{\lambda_2^2 + \lambda_3^2}{1 + \lambda_3^2} d\lambda_3^2$$

$$+ \alpha_e^2 \frac{\lambda_2^2 + \lambda_3^2}{1 - \lambda_2^2} d\lambda_2^2 + \alpha_e^2 (1 + \lambda_3^2) (1 - \lambda_2^2) d\lambda_1^2. \quad (8)$$

The first term of Eq. (8) represents a differential "depth equation," as can be seen from the following argument.

Consider a fixed latitude and longitude. Then, Eq. (8) shows the relation between a given change in  $\lambda_3$  and the corresponding depth change  $dz$  (because this  $ds$  is a change along the normal to the ellipsoid).

$$dz^2 = \alpha_e^2 \frac{\lambda_2^2 + \lambda_3^2}{1 + \lambda_3^2} d\lambda_3^2. \quad (8a)$$

The interesting fact is the presence of the latitude factor  $\lambda_2$  in Eq. (8a). This shows that a surface of constant  $\lambda_3$  cannot be at constant depth in a global sense. Two limiting cases are easy to check out: at the pole  $\lambda_2 = 1$  and

$$dz^2 = \alpha_e^2 d\lambda_3^2; \quad (8b)$$

at the equator,  $\lambda_2 = 0$ , so

$$dz^2 = \alpha_e^2 \frac{\lambda_3^2}{1 + \lambda_3^2} d\lambda_3^2. \quad (8c)$$

The fundamental parameters derived in Eq. (7) become useful here. Our approximation in the Hamiltonian differential equations will assert that (8a) and (8b) are negligibly different at any relevant latitude for depth changes over the topmost few kilometers near the sea surface. This is because  $\lambda_{3_0}^2$  is very large compared with unity. Thus the case is made for abandoning a strict accounting of  $\lambda_3$  in favor of the layer-by-layer differential analysis that monitors *depth* changes of the ray path without referencing the point-origin of the coordinates. This is essential for an efficient representation of environmental data (sound speed, flow velocities, bathymetric depths, etc.).

Conversely, the spheroidal surface's curvature radii that a ray reaches at any point in its trajectory deserve careful attention. At any point on the surface of a spheroid, or on the surface of an interior shell, there is an infinity of radii of curvature, and they are functions of latitude and the azimuth at each point. Two of these radii define all others. They are the principal radii of curvature, the *meridional* radius  $r_m$  (curvature in the meridional plane), and the *prime vertical* radius  $r_v$  (curvature in the plane of the "prime vertical"; this plane is perpendicular to the meridional plane through the surface point).

The principal radii of curvature are compactly expressed by introducing an auxiliary function,  $w$ , of  $e$  and latitude  $\chi$ :

$$w^2 = 1 - e^2 \sin^2 \chi, \quad (9)$$

so that

$$r_m = \frac{a(1-e^2)}{w^3}, \quad (10)$$

and

$$r_v = \frac{a}{w}. \quad (11)$$

Equations (9) through (11) are valid only on the earth's spheroid surface if one considers  $a$  and  $e$  fixed. This is the normal practice, but conceptually one could let  $a$  and  $e$  vary as functions of depth. As one looks at spheroidal shell surfaces that are below the sea surface, the equatorial radius  $a$  decreases and the first eccentricity  $e$  increases with the same relative rate. This can be seen by taking the logarithmic derivative of (6a), because the left-hand side (the scale parameter  $\alpha_e$ ) is an invariant for our planet. Equation (6) can be "driven in reverse" starting with the surface parameters in Eq. (7), and using Eq. (8a) to determine  $d\lambda_3$  for any prescribed  $z$  or  $dz$ .

Alternatively, one leaves  $a$  and  $e$  fixed at their surface value and considers an approxima-

tion that is depth dependent. Since the factor  $w$  in Eqs. (9)–(11) is close to unity, the true curvature radii "at depth" are closely approximated when the surface curvature radii are decreased by the local depth,  $z$ , of a ray point.

$$\begin{aligned} r_m(z) &\approx r_m - z \\ r_v(z) &\approx r_v - z. \end{aligned} \quad (12)$$

The curvature approximation error is sufficiently small for modeling propagation in the ocean (at a depth of 5 km, it is  $2 \times 10^{-9}$  at the equator and  $3 \times 10^{-6}$  at latitude  $45^\circ$ ), and it is probably small enough even for modeling propagation at subacoustic frequencies (at a depth of 20 km, it is  $3 \times 10^{-8}$  at the equator and  $1 \times 10^{-5}$  at latitude  $45^\circ$ ).

It follows from (11) and (10), using (9), that everywhere on the spheroid

$$r_v \geq r_m. \quad (13)$$

Furthermore, the radius of curvature,  $r_{\alpha_h}$ , in the direction of any azimuth  $\alpha_h$  is determined by a relation due to Euler:

$$1/r_{\alpha_h} = \frac{\cos^2 \alpha_h}{r_m} + \frac{\sin^2 \alpha_h}{r_v}. \quad (14)$$

Taking the mean value integral of  $r_{\alpha_h}$  over all azimuths, one gets the earth's mean radius of curvature  $\bar{r}$  at a given geodesic latitude:

$$\bar{r} = \sqrt{r_m r_v}.$$

Using (13) with (14) it is clear that

$$r_m \leq r_{\alpha_h} \leq r_v$$

and that

$$r_m \leq \bar{r} \leq r_v.$$

Figure 4 shows the deviations of  $r_v$  and of  $r_m$  from  $\bar{r}$  as a function of latitude. The deviations are largest at the equator where the difference between the two principal radii of curvature exceeds 42 km. One sees that the spheroid behaves like a sphere at the poles (having a

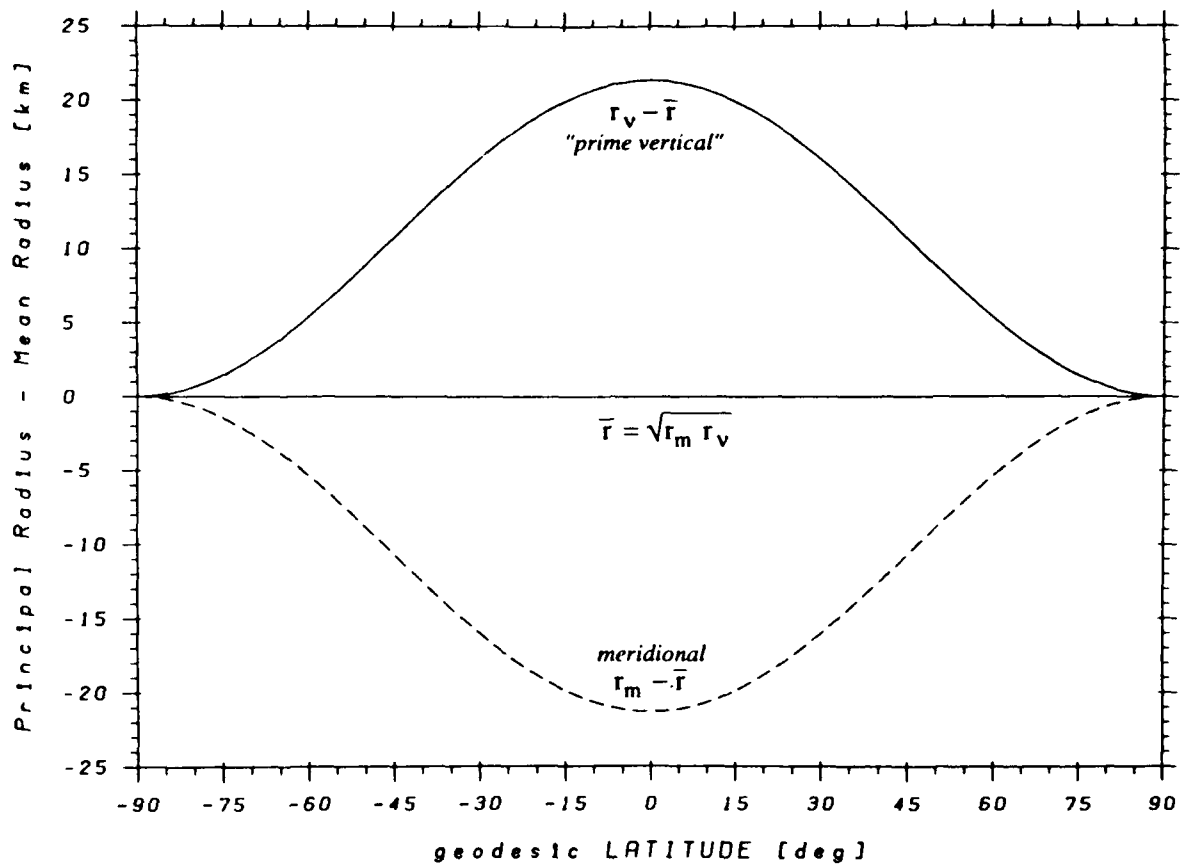


Figure 4. Deviations of  $r_m$  and of  $r_v$  from  $\bar{r}$  as a function of latitude.

single measure of curvature, albeit of larger radius—nearly 6400 km—than the earth's average radius of 6371 km). But the spheroid does not behave like a sphere at the equator. In the tropics the azimuthal steering on the sphere and on the spheroid will be significantly different. Long acoustic propagation paths cannot be "very" long unless they cross the equator, and therefore this difference matters.

#### *Azimuthal Steering on the Spheroid*

Equation (14), and a text passage in the NOAA document for HARPO (Jones et al., 1986, pp. 115–116), provide an instructive motivation for clarifying the "steering" issue: "For some long-range ray calculations in the ocean, a spherical model of the earth may not be accurate enough. Some applications may require ocean models to be expressed in geodetic (e.g., spheroidal) coordinates, which would be transformed to spherical coordinates for ray tracing. However, for paths of a few thousand kilometers and less, we would recommend using a spherical computational coordinate system with  $W(1)$  set to the local radius of curvature of the geoid in the propagation direction."

The term "ocean models" in this passage refers to the analytical models representing the refractive index or current velocity data, and  $W(1)$  is the only admissible value of the radius for the computational sphere in HARPO.

We have fundamental problems with parts of this recommendation. It is clear that the ray paths cling to a "curved earth" because the "data" (including the top and bottom boundaries of the oceanic waveguide) are given in a specific "curved space," not because the differential equations are cast in a particular curved coordinate system. It is a question of adjusting mathematics to the data vs adjusting data to the mathematics. The cited passage recommends a variant of adjusting mathematics to the data for paths of a few thousand

kilometers or less, and adjusting data to the mathematics for longer paths. There are strong reasons for providing mathematics that adjusts to the data in all conceivable cases, regardless of the scale of the problem.

Since that part of the recommendation that leaves data "as is" and uses a local radius of curvature (i.e., adjust the mathematics) is also easier to implement in HARPO, we explored it. Equation (14) furnishes the "local radius of curvature...in the propagation direction," but this direction changes even on a perfect sphere (i.e., the path is orthodromic and not loxodromic), so one value of  $W(1)$  is hardly enough. With just one representative radius of curvature along the path, the results were really not distinguishable from a pilot run on a perfectly spherical earth of nominal radius. This is understandable in the context: both runs were done in spherical coordinates, except the two radii were somewhat different.

Next, by modifying HARPO's code, we used the local azimuth along the path to recompute the azimuthally dependent local curvature radius at every step. The results were, again, hardly distinguishable from the spherical pilot run, but a close inspection of propagation times revealed small differences between the runs. The topological vs metric aspects of long range acoustic ray computations had become clearer:

- As long as there is only one radius built into the differential equations associated with the Hamiltonian, the azimuthal steering will be topologically the same: on a golf ball, on the earth, or on Jupiter, it will be a great circle. Two distinct radii are needed, (10) and (11), to achieve a steering that results in a variationally (geodesic) minimal or stationary trajectory.
- The use of a local curvature radius "in the direction of propagation" is metrically correct. If one possesses an independently prescribed geodesic path, such as the "refracted geodesics" of Munk et al. (1988),

then the computation in the vertical does better when a variable radius of curvature is used instead of a fixed radius (e.g., equal volume or equal area, etc.). However, as explained earlier, the major representation errors in long range acoustic propagation have a topological rather than a metric origin.

From here on, we can speed up the pace of presentation by referring to the literature, mainly Munk et al. (1988) and Jones et al. (1986), without reproducing their analytical treatment.

#### *Horizontally Refracted Geodesics on the Spheroid*

A complete treatment of unrefracted (surface) geodesics and refracted geodesics (at the depth of the sound channel) is given by Munk et al. (1988). We have already discussed their assumptions. In each set of their equations (Eq. (1) for the unrefracted, Eq. (2) for the refracted case), there are three equations. Two relatively simple ones describe changes in latitude and longitude, and the more complex one describes change of the azimuth. In the refracted case, when the path length is used instead of the propagation time as the independent argument, the sound speed and its derivatives occur only in the azimuthal equation. This reinforces the notion that this equation is the (horizontal) "steering" equation for the propagation path.

The following topology with respect to curvature radii is relevant. The meridional radius occurs in the latitude equation (plausible and easy to visualize), the prime vertical curvature radius occurs in the longitude equation, and both have a place in the azimuthal equation. If the sound speed were constant there would be no difference between the refracted and unrefracted equations, and if both principal curvature radii become the same (as they nearly would in the Arctic Ocean) then everything reverts to the spherical case.

#### *Antipodal Acoustic Paths on the Spheroid*

Munk et al. (1988) discuss the longest experimental sound propagation path, from Perth to Bermuda, that has been documented. The range was 19,820 km, only about 185 km short of antipodal. They are also interested in true antipodal conditions because such geometries may be realizable in the future, but this is not a primary object of their paper. They say that the "great circle geometry fails catastrophically for near-antipodal ranges," and that "for exactly antipodal transmissions (geodesic  $180^\circ$ ) the geodesic goes through the pole, as does one of the infinite number of great circle routes" (their Fig. 5). These are correct and important observations, particularly relevant in view of their concluding remark that this landmark experiment may be worth repeating given our present understanding of the issues involved.

We are specifically interested in the forthcoming Heard Island feasibility experiment. Heard Island is closer to Africa than it is to Australia, and the acoustic propagation geometries from Heard Island are not antipodal. Heard Island's antipode is on land in western Canada, as can be seen in Figs. 1 and 2. However, it is clear that with a ship under way, say, from Perth or Fremantle to Heard Island, one reaches potential oceanic transmission points that have antipodal geometry relative to some feasible receiver locations in the North Atlantic.

Two questions regarding potential underwater acoustic propagation on antipodal paths arise naturally:

- Are antipodes acoustically "reachable"?
- If reachable, is there a likelihood of energy focusing at the antipode? If not, what sort of energy focusing can be expected in some neighborhood of the antipode?

Munk et al. (1988) show that horizontal refraction significantly modifies the actual sound paths relative to those defined by spherical or spheroidal geodesics. Such modification

is one of degree rather than being related to the underlying fundamentals.

Thus a conceptual dilemma exists:

- In the spherical approximation the antipode is reachable, albeit in a singular way, by many great circles passing through a feasible oceanic window. This window has about the same azimuthal width as the corresponding window in the spheroidal approximation. Focusing can be strong (they estimate +20 dB for the Perth-Bermuda geometry, 185 km short of the antipode), and becomes theoretically unlimited at the antipode.
- Alternatively, in the spheroidal approximation, the antipode is not reachable because the unique geodesic to the antipode must go through a pole, and is definitely outside the feasible oceanic window.

We investigate these questions in a short aside that fits the geodesic theme of this section. Figures 5 and 6 describe the findings for a viable propagation geometry. To emulate a propagation window of similar azimuthal width (about 20°) to the "Atlantic" window from Heard Island (Fig. 1), we place a hypothetical source (Fig. 5) at the longitude of Perth but at a higher latitude (40°S). The horizontal center of the radiated fan passes through Heard Island, and a hypothetical antipodal receiver is in the North Atlantic about 475 n.mi. NNW of Bermuda.

Figure 6 shows the computed pattern in the geographic neighborhood of the antipode. The horizontal ray fan focuses on an area about 20 km away from the antipode, which is not acoustically reachable through the ocean. The focusing is not to a point but is spread along a caustic, part of which we label "audible" in the belief that the pattern, if not its exact location, will persist even in the presence of lateral refraction.

This dilemma was clarified by Helmer (1880), who investigated the uniqueness of geodesics on the spheroid. The prototype of a

surface with nonunique geodesics is a cylinder of revolution. Take any pair of distinct points not on the same meridian, the eigen-geodesics between these two points are helices of 1, 2, ..., n, and up to an infinite number of windings. They are geodesics because each has a shorter (stationary) path length relative to any of its neighboring paths. The helix with a single winding has the absolute shortest path length; it is the Fermat geodesic. The spheroid is topologically between the sphere and the cylinder, but our spheroid is very close to a sphere. Helmer has done remarkably detailed computations of the geodesic geometry in the neighborhood of the antipode and has identified the multipath region that constitutes our present context.

The caustics that we label "audible" and "inaudible" in Fig. 6 constitute one leg of an astroid, a star-like envelope of geodesics centered on the antipode. The term "inaudible" should be understood in context: each of the four legs of the astroid is a horizontal caustic (i.e., an envelope curve to a family of geodesics), and only part of one of them will be "audible." The family of geodesics emanating from the Indian Ocean transmit point is unique only outside this astroid.

The major axes of the astroid are aligned N-S and E-W. The size of the astroid depends on the eccentricity of the spheroid and on the latitude of the transmit point. In particular, the size of the N-S axis is the greater of the two, and is proportional to the cosine of the transmit latitude. The E-W axis size is proportional to the cosine squared of the transmit latitude. Consequently, high latitude transmit points are associated with a small region of geodesic multipathing at the antipode. The size of the astroid would shrink to zero if a geographic pole were a feasible transmit point.

Moreover, the relative focusing (+20 dB at Bermuda) estimated by Munk et al. using a spherical argument is basically correct even in the spheroidal case, as evidenced by Fig. 5.

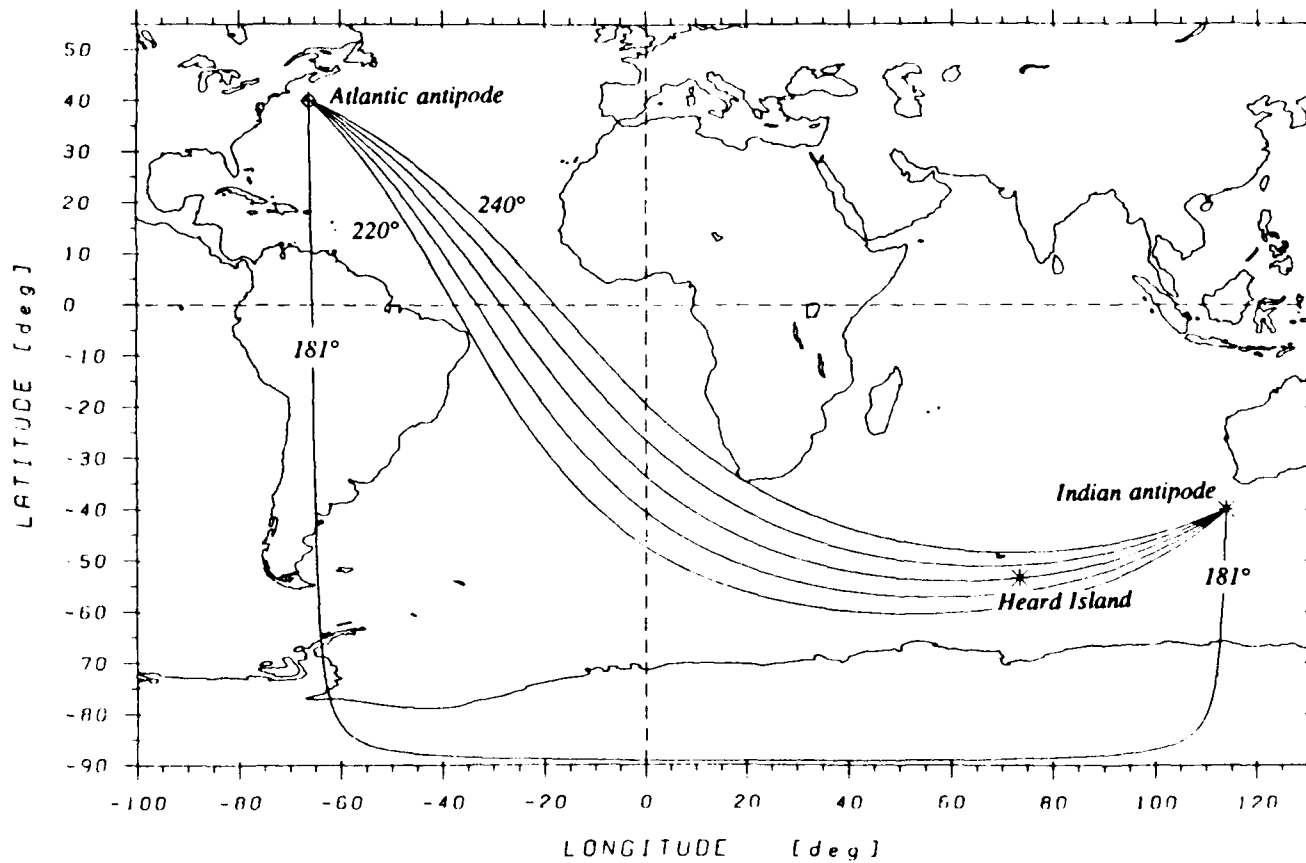


Figure 5. Geodesics from a location south of Perth. The fan of geodesics with azimuths between  $220^\circ$  and  $240^\circ$  approaches the Atlantic antipode. The geodesic with an azimuth of  $180^\circ$  connects the antipodes exactly ( $181^\circ$  is computable).

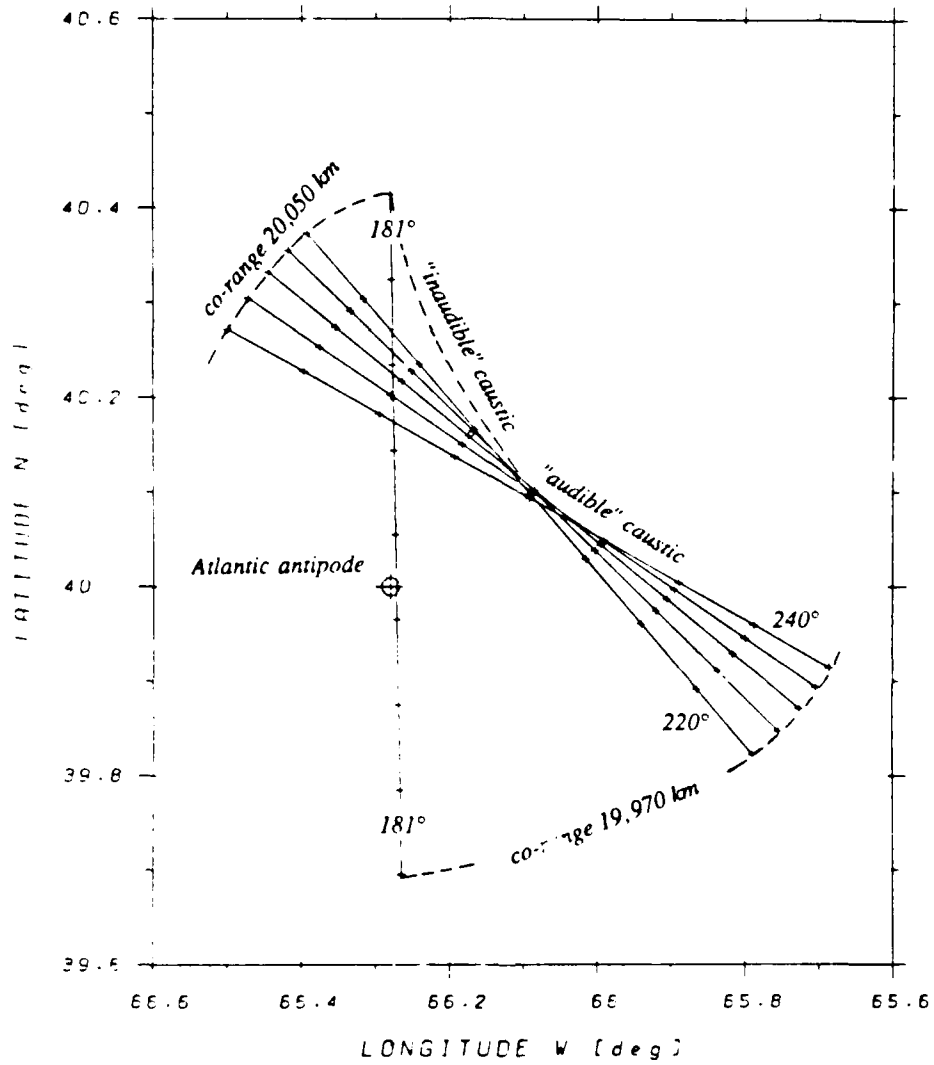


Figure 6. The actual pattern of geodesics (from Fig. 5) in the vicinity of the Atlantic antipode.

Figures 5 and 6 are generated from the same high precision geodesic computations, but the ray fan in Fig. 5 is very similar to a ray fan on a spherical earth. Its gross structure does not even hint at the details that are revealed by Fig. 6.

### *Hamiltonian*

We chose HARPO as a preliminary tool for 3-D modeling of very long range acoustic propagation. It was clear, though, that new software would eventually be needed for easier absorption of data updates on a global scale. Then the ray equations could be carried over as Hamiltonian equations copied from HARPO, or they could be written using the eikonal equation as a base. This accounts for our interest in understanding the Hamiltonian formalism in a wider setting.

A few comments about the Hamiltonian approach, in parallel with those given by Jones et al. (1986), may help explain why numerical codes that are not based on the Hamiltonian may serve specific objectives rather well.

- Not only are the ray paths computed from the Hamiltonian equations the same as those computed from differential equations that are derived from the eikonal, but the Hamiltonian itself is derivable from the eikonal (Whitham, 1961) This is true for a broad formulation of the dispersion relation (e.g., including a moving medium).
- It is also true that the Hamiltonian is the more original and fundamental construct if one thinks of the eikonal as a related but different concept. This relation was the subject of a little-known polemic exchange in 1937 regarding geometrical optics, but applicable to geometrical acoustics, between J. L. Synge and M. Herzberger. It ended on the notion that Bruns (the formulator of the eikonal) rediscovered in 1895 the ray propagation Hamiltonian that was conceived in 1832, but

brought to light only in 1931 (Conway and Syngé).

- The Hamiltonian approach to geometrical acoustics entered the literature in the 1950's (Keller, 1954). This was nearly synoptic with actual applications of the Hamiltonian ray equations in radio-wave propagation by J. Haselgrove (1954). Her methodology stimulated much of the subsequent work, bridging applications in several media of propagation.
- The literature cited, and the individual contributions of Jones et al., provide a good example of some activities in the 1960's and 1970's leading to HARPO. An overview by Ostashev (1985) puts the Hamiltonian and eikonal based ray formalisms into the context of the more general acoustic propagation theory for an inhomogeneous moving medium.
- One may conclude on balance that the Hamiltonian approach offers an elegant, but not always simple, path to ray tracing. This is well articulated by Lighthill (1979) who relegates the Hamiltonian equations to what he calls a "brief parenthesis on parallel with other fields of study" in his extensive sections on the general theory of ray tracing and ray tracing in a wind.
- The primary appeal of the Hamiltonian is that it is independent of the coordinates used. The converse is also true; the Hamiltonian differential equations in a given coordinate system do not change when the Hamiltonian changes because, say, a different set of propagation conditions is to be modeled. We rely heavily on this in modifying HARPO's code for use in the ocean on the ellipsoidal earth. However, the ray equations derived from the eikonal also have a vector form (Pierce, 1981) that is intrinsically independent of the computational coordinate system.

There are six ordinary, first order, non-linear Hamiltonian equations that define the ray

trajectory in a three-dimensional space. Three of them define the position coordinates of the ray point. Since we start out with a spherical coordinate system, all terminology refers to such a system. The computed ray-point position is the (geocentric) radius  $r$ , the colatitude  $\theta$ , and the longitude  $\phi$ . The other three equations define the local components of the wavenumber vector  $\vec{\kappa}$  that is tangent to the ray path. These six equations are integrated subject to six initial conditions; the three coordinates of the transmitter, and the three components of the initial direction (initial value of the wavenumber vector).

In adapting the given set of Hamiltonian equations to propagation in the thin ellipsoidal planetary waveguide, one recognizes immediately the asymptotic and the actual structure:

- The "horizontal" components of the wavenumber vector ( $\kappa_\theta, \kappa_\phi$ ) must implement the azimuthal steering that corresponds to a "refracted geodesic" of Munk et al. (1988). This is fed back to the latitude and longitude equation, ensuring a correct overall global trajectory. Four of the six equations are involved in this process, and this foursome is strongly coupled.
- The other two equations are the radial position and the radial component of the wavenumber. One more equation, a horizontal component for the wavenumber, is needed to define the ray path in the "vertical" cylindrical surface. But two more are available, the aforementioned equations for ( $\kappa_\theta, \kappa_\phi$ ). They too comprise a foursome. Again, this foursome is strongly coupled.
- Thus the six Hamiltonian equations subtend, in a topological sense, two overlapping four-somes of equations with strong coupling within each foursome and weak coupling across them.
- The weak coupling across these two equation sets is implemented in the numerical code, and it ensures that the ray paths are fully 3-D,

i.e., not confined to an idealized cylinder to which they would be bound in the asymptotic case.

The ocean data (sound speed field and current velocity field) remain defined in spherical coordinates (latitude, longitude, and depth). Depth is defined as the difference between two geocentric radii, the radius to the sea surface and the radius to the point considered. For HARPO, the ocean data are appropriately termed "ocean models" because they must be given analytically rather than pointwise.

The earth's ellipticity is introduced into the Hamiltonian equations by distinguishing the two principal radii of curvature,  $r_m$  from (10) and  $r_v$  from (11), in the individual terms of the equations described below. The depth of a ray point is based on the geocentric radius  $r = \rho_g$  from (4). Equation (12) may then be substituted for (10) and (11).

A term-by-term validation of the modified equations is accomplished by requiring that they reduce to the surface geodesic equations when all lateral gradients of the refractive index are set to zero, and when an artificial vertical sound channel is established with its axis at the surface. A numerical validation was performed by running this reference case through the modified code.

The spherical Hamiltonian equations that we adapted to the earth's ellipsoid are those residing in HARPO's subroutine HAMLTN. The original equations are (6.10) through (6.15) in the HARPO document by Jones et al.

Let  $H$  be the Hamiltonian,  $t$  the propagation time,  $c_0$  a reference constant sound speed,  $c$  the local sound speed,  $p = c_0 t$  the independent variable of integration,  $\omega$  a fixed wave frequency, and  $F = c_0 \partial H / \partial \omega$  a fixed scale factor. The geocentric radius to the ray point is  $r$ , the colatitude is  $\theta$ , and the longitude is  $\phi$ . Notice that  $p$  is a "scaled time" with numerical value roughly equal to the path length. The exact relation between  $p$ ,  $t$ , and the actual path length  $s$  is

$$\frac{d}{ds} = \frac{c_0}{c} \frac{d}{dp} = \frac{1}{c} \frac{d}{dt}$$

The six new Hamiltonian equations are

$$\frac{dr}{dp} = -\frac{1}{F} \frac{\partial H}{\partial \kappa_r}, \quad (15)$$

$$\frac{d\theta}{dp} = -\frac{1}{r_m F} \frac{\partial H}{\partial \kappa_\theta}, \quad (16)$$

$$\frac{d\phi}{dp} = -\frac{1}{r_s \sin\theta F} \frac{\partial H}{\partial \kappa_\phi}, \quad (17)$$

$$\begin{aligned} \frac{d\kappa_r}{dp} &= \frac{1}{F} \frac{\partial H}{\partial r} + \kappa_\theta \frac{d\theta}{dp} \\ &+ \kappa_\phi \sin\theta \frac{d\phi}{dp}, \end{aligned} \quad (18)$$

$$\begin{aligned} \frac{d\kappa_\theta}{dp} &= \frac{1}{r_m} \left[ \frac{1}{F} \frac{\partial H}{\partial \theta} - \kappa_\theta \frac{dr}{dp} \right. \\ &\left. + \kappa_\phi r_m \cos\theta \frac{d\phi}{dp} \right], \end{aligned} \quad (19)$$

and

$$\begin{aligned} \frac{d\kappa_\phi}{dp} &= \frac{1}{r_s \sin\theta} \left[ \frac{1}{F} \frac{\partial H}{\partial \phi} - \kappa_\phi \sin\theta \frac{dr}{dp} \right. \\ &\left. - \kappa_\theta r_m \cos\theta \frac{d\theta}{dp} \right]. \end{aligned} \quad (20)$$

The Hamiltonian  $H$  is used directly as specified by Jones et al. in dispersion relations designed to cover specific propagation conditions. Two important ones are

- (i) Propagation through an inhomogeneous stationary medium. This propagation is isotropic; the ray paths are perpendicular to the wavefronts.
- (ii) Propagation through an inhomogeneous moving medium. This propagation is anisotropic; the ray paths are no longer perpendicular to the wavefronts.

Ray tracing results for the Heard Island to Oregon Coast paths, utilizing (15) through (20) and both isotropic and anisotropic media, are presented in Section 4.

One problem related to data representation remains when using (15) through (20). These are, as stated, geocentric equations on the ellipsoid, but they are not oblate spheroidal equations. For them, even a level sea surface, or a flat bottom, has a radial position that varies with the horizontal coordinates.

Throughout this subsection on the Hamiltonian, we drew attention to alternative viewpoints that are relevant to ray tracing. A major alternative that loomed in the background is the abandonment of a sharp distinction between 2-D and 3-D in the thin global boundary layer. This involves a "2-D+" boundary layer coordinate system, and is beyond the scope of this text. However, the ray tracing equations will be looked at in this emerging context. Therefore, before reporting some of the numerical results obtained using a 3-D Hamiltonian ray tracer, we draw attention to Appendix A. In it we illustrate a 2-D set of ray equations in two coordinate systems, show their relation to the Hamiltonian equations, and point to the merit of having specialized equations that affect possible cancellations analytically rather than numerically. The illustrated equations are those that Bold and Birdsall (1986) discuss as the "third algorithm (angular form)," and that are used in a number of interesting applications (e.g., Baxter and Orr (1982) and Eliseevnin (1965)).

### 3. Indian/Pacific Sound Speed Model and the Antarctic Circumpolar Current Model

The computer code in HARPO requires that the 3-D field of the sound speed and of the current velocity be continuous, and that they have *continuous* partial derivatives in the three spatial directions (Jones et al., 1986). For

vector fields, each component must satisfy this requirement. The menu-driven HARPO further requires that such fields obey a particular formalism. This formalism is generally termed OCEAN MODELS, and it includes additional species of models, for the ocean bottom, absorption, etc. In any HARPO run there may be no more than one model of each species, but some fields allow a subspecies of the general model. The general model for a field is termed a "background" model, and the subspecies is termed the "perturbation" model for that field. This arrangement permits the user to break up the complexity of modeling a field, and to investigate sensitivity questions by switching the perturbation model on and off.

The sound speed field for modeling propagation paths in the Tasman window (Fig. 2) had to be defined over ranges that were so long (18 Mm) that the existence of a single perturbation submodel was not sufficient to describe all significant departures from the background. Instead, the "background" field itself had to include practically all the complexity that was required. Figure 7 shows an image of the final analytical sound speed field as a function of depth (0 to 5 km) and latitude (70°S to 55°N), with the sound speed color coded between 1450 m/s and 1550 m/s. The rationale for this model, and its limitations, will be discussed after presenting its analytical configuration.

#### *Sound Speed Model*

The Indian/Pacific Ocean 3-D sound speed model is valid in the neighborhood of propagation paths from Heard Island through the Tasman window. It is constructed as follows:

- In the vertical coordinate the "background ocean model" satisfies the equations of a continuum of canonical sound speed profiles (Munk, 1974) and is referred to simply as Munk's SSP (sound speed profile). This profile was primarily meant to be applicable in the vicinity of the sound channel axis, but

in our experience it can match archived data over a significantly wider depth range at nearly every latitude of interest.

The functional form for the sound speed  $c(z)$  as function of depth  $z$  (positive down) is defined in the Munk SSP as

$$c(z) = c_0 [1 + \epsilon (\gamma + e^{-\gamma} - 1)], \quad (21)$$

where

$$\gamma(z) = \frac{2}{H_c} (z - z_0).$$

This profile is completely determined by four parameters:  $z_0$ , depth of the sound channel axis;  $c_0$ , sound speed at axis depth;  $\epsilon$ , a dimensionless perturbation or shape parameter; and  $H_c$ , a characteristic scale depth.

A set of the fitted profiles, offset by 20 m/s each and indexed by latitude, is shown in Fig. 8. Table I contains some of the numerical data that were used to estimate the four parameters, and, in the last two columns, the fitted sound speed at the surface and at a depth of 4400 dbars. The archived data used to support this model were not selected by "objective means" (least square fits, or equivalents) but were chosen after a sensitivity analysis of Eq. (21) that is outlined next.

Data from five sources were used in this analysis. The conditions at the sound channel axis were obtained from the appropriate graphs (Figs. 3(a) and (b) of Munk and Forbes, 1989). For the rest of the water column along the acoustic path, the sound speed was computed from oceanographic data extracted from three atlases (Gordon et al., 1982; Wyrki, 1988; Craig et al., 1981). Also, tables and graphs of Podeszwa (1976) were used to estimate the sound speed data in the North Pacific.

A few interesting facts, not described in Munk's original paper, can be deduced from Munk's canonical profile. They show the versatility of Eq. (21) and the relevance of the underlying physics:

- The parameter pair  $(\epsilon, H_c)$  is independent of the parameter pair  $(z_0, c_0)$  because  $\partial c/\partial \epsilon \rightarrow 0$  and  $\partial c/\partial H_c \rightarrow 0$  as  $z \rightarrow z_0$ . Therefore, the parameters defining conditions at the sound channel axis can be chosen independently from those that define the upper and lower branch of the SSP. These relations are illustrated in Fig. 9. Note that  $(z_0, c_0)$  determines a single *point*, while  $(\epsilon, H_c)$  controls the *interval* behavior of  $c(z)$  away from the sound axis.
- When  $(z_0, c_0)$  is chosen at different latitudes along the Tasman window propagation path and  $(\epsilon, H_c)$  is estimated from the near surface and the deep water sound speeds, then  $H_c$  and  $\epsilon$  show correlation in the form of an empirical *affine* transformation:

$$H_c \text{ [km]} = \sigma_1 \epsilon + \sigma_0, \quad (22)$$

where  $\sigma_1 \cong 115$  and  $\sigma_0 \cong 0.3$ . The estimates  $(\epsilon, H_c)$  from Table I are displayed in Fig. 10, and it is seen that  $H_c$  "tracks"  $\epsilon$  over a wide interval of latitudes. The scatter diagram  $(\epsilon, H_c)$  on which Eq. (22) is based is shown in the upper right corner of Fig. 10. But the apparent relationship implied by (22) must be interpreted guardedly. If nature behaved this regularly it would be disappointing, as well as unlikely.

What is seen in Fig. 10 can be qualitatively explained by noting another asymptotic behavior of (21): when  $\epsilon \rightarrow 0$ , then  $c \rightarrow c_0$  for any  $H_c$  and for all  $z$ —hence the term "perturbation parameter" for  $\epsilon$ . This parameter attains its largest values where the sound channel axis is deep (between 30°S and 40°S), to account for the sound speed contrast between surface and deep water relative to the water at the channel axis. The scale depth  $H_c$  must also be large there to prevent the sound speed contrast from becoming too large. Conversely,  $\epsilon$  will be small, and  $H_c$  will be small when the surface water is warm (high sound speed), but the channel axis moves closer to the surface, as in the low latitudes of the North Pacific.

This explanation shows why a *negative* correlation between  $\epsilon$  and  $H_c$ , as  $\epsilon$  or  $H_c$  evolves along a hypothetical propagation path, could never fit the SSP of any deep ocean: a small  $\epsilon$  and large  $H_c$  would estimate an SSP that is too uniform top to bottom, while a large  $\epsilon$  and small  $H_c$  would imply sound speeds that are much too high at the surface, or at the bottom, or both. Thus, choices of  $\epsilon$  and  $H_c$  that smoothly track the path parameter, but randomly map about a *positive* correlation line, can help generate canonical profiles that effectively model the vertical distribution of the sound speed in the ocean. This holds in a wider neighborhood of the channel axis than we anticipated. Such representation is valuable while using HARPO, but we stress that the architecture of a long range ray tracer should be oriented toward assimilation of gridded sound speed data upon which one should not impose any smoothness requirements.

The next step in developing the required analytical differentiability of the ocean sound speed model for HARPO is to link the individually fitted Munk SSPs horizontally, at constant pressure-depth levels, thereby creating the continuum. We decided on a fit by horizontal splines—not to the profiles, but to their canonical expansion parameters in Eq. (21). Figure 11 shows the sound speed at the channel axis, at the surface, and at the depth of 4400 dbars. Figure 12 shows the modeled depth of the channel axis. The independent variable in both figures is the latitude.

The splines are piecewise cubic splines, but not the ordinary, analytically linear, splines. They are quasi-Hermite (IMSL, 1979) nonlinear splines that exhibit some "spline-in-tension" properties. Originally known as "splines obtained by local procedures," they were developed by Akima (1970) for applications where oscillations of linear splines must be attenuated if not altogether suppressed. It can be seen from Figs. 11 and 12 that the latitude belt between 40°S and 55°S encompasses a

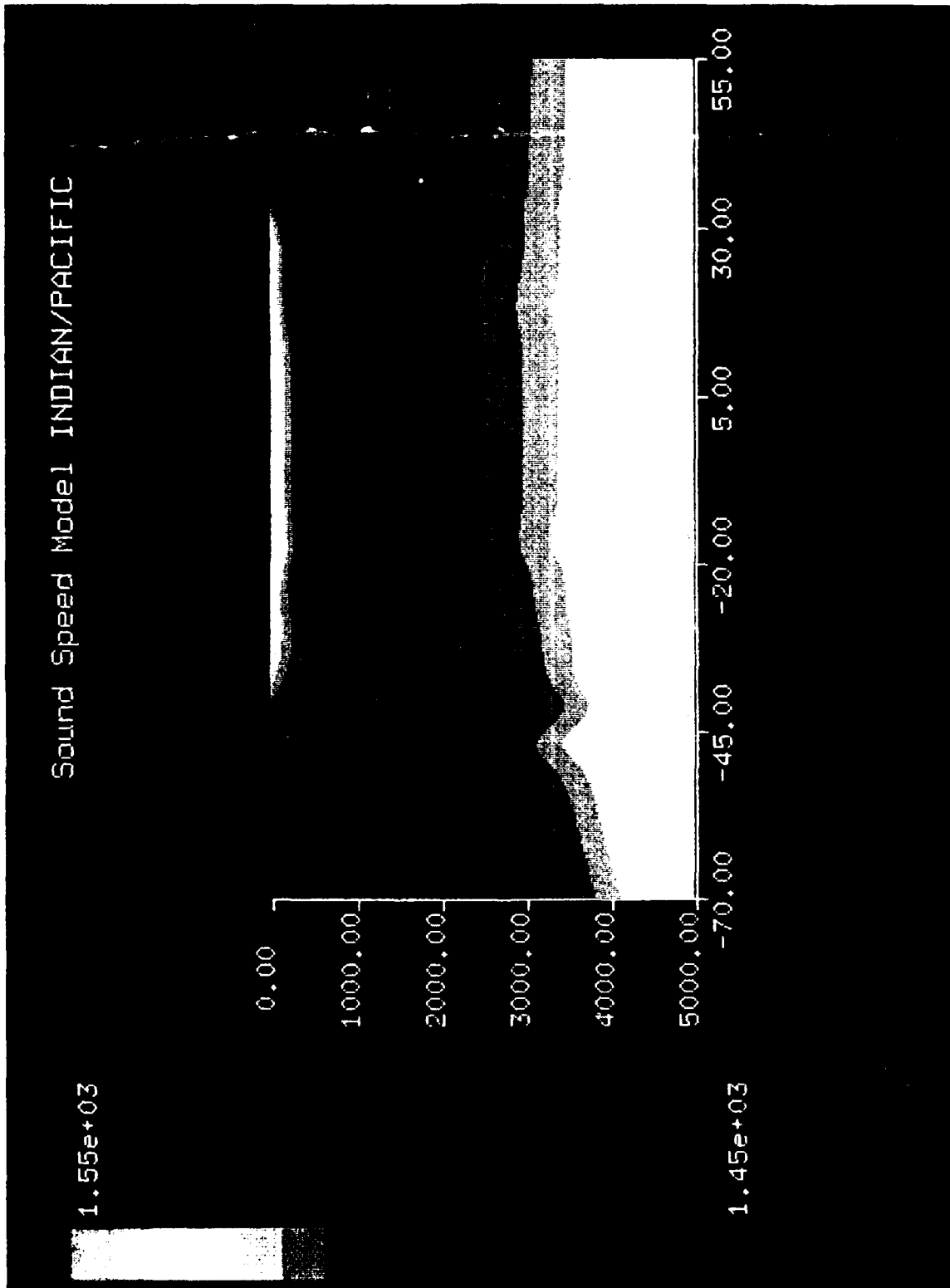


Figure 7. Image of the analytical sound speed model used for modeling propagation through the Tasman window as a function of latitude.

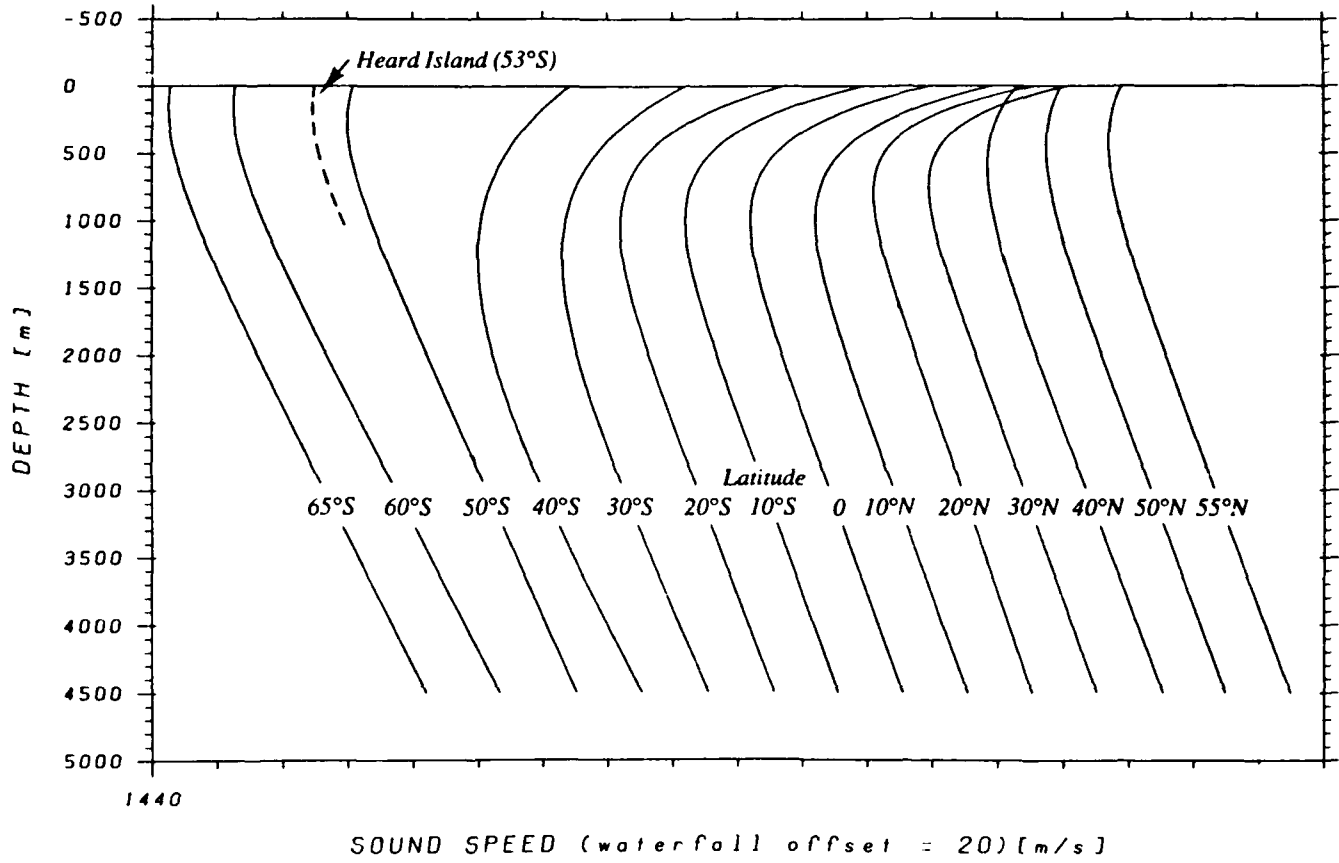


Figure 8. Sample sound speed profiles for the Tasman window indexed by latitude and offset by 20 m/s from one another.

Table 1. Parameterization of a Hermite splined model for the Indian/Pacific sound speed field.

## INDIAN/PACIFIC

LAT [deg]	SOUND CHANNEL*		FROM ARCHIVES*		PARAMETERS		USING PARAMETERS	
	$z_0$ [m]	$c_0$ [m/s]	c(surf) m/s]	c(4400) [m/s]	$\epsilon$ [-] $\times 100$	$H_c$ [km]	c(surf) [m/s]	c(4400) [m/s]
-70.0	150.0	1445.00	1445.00	1521.20	0.7811	1.1212	1445.44	1521.31
-65.0	150.0	1445.00	1446.00	1523.90	0.7675	1.0718	1445.48	1523.93
-60.0	150.0	1445.00	1446.50	1526.60	0.7595	1.0314	1445.51	1526.60
-50.0	250.0	1460.00	1462.30	1530.25	0.5477	0.8683	1461.62	1530.28
-40.0	1280.0	1480.00	1508.65	1530.65	1.5798	2.0657	1508.38	1530.55
-30.0	1280.0	1486.00	1523.70	1530.90	0.9271	1.5124	1523.77	1531.08
-20.0	1050.0	1484.00	1533.80	1531.10	0.4745	0.8954	1533.94	1531.23
-10.0	1000.0	1484.00	1538.45	1531.15	0.4011	0.7862	1538.67	1531.04
0.0	1000.0	1484.00	1539.00	1531.15	0.3993	0.7829	1539.17	1531.05
10.0	1000.0	1484.00	1537.75	1530.90	0.4002	0.7888	1537.97	1530.77
20.0	800.0	1482.00	1532.00	1530.60	0.2795	0.5815	1531.37	1530.58
30.0	750.0	1479.00	1521.00	1530.35	0.2883	0.5764	1521.19	1530.22
40.0	600.0	1477.00	1486.50	1530.10	0.5156	0.9722	1486.15	1530.49
50.0	450.0	1475.00	1477.50	1529.80	0.5068	0.9730	1479.46	1529.76
55.0	420.0	1474.00	1475.50	1529.70	0.5110	0.9727	1477.83	1529.66

\*Sources for archive data:

Munk and Forbes, 1989

Gordon et al., 1982

Wyrski, 1988

Craig et al., 1981

Podszwa, 1976

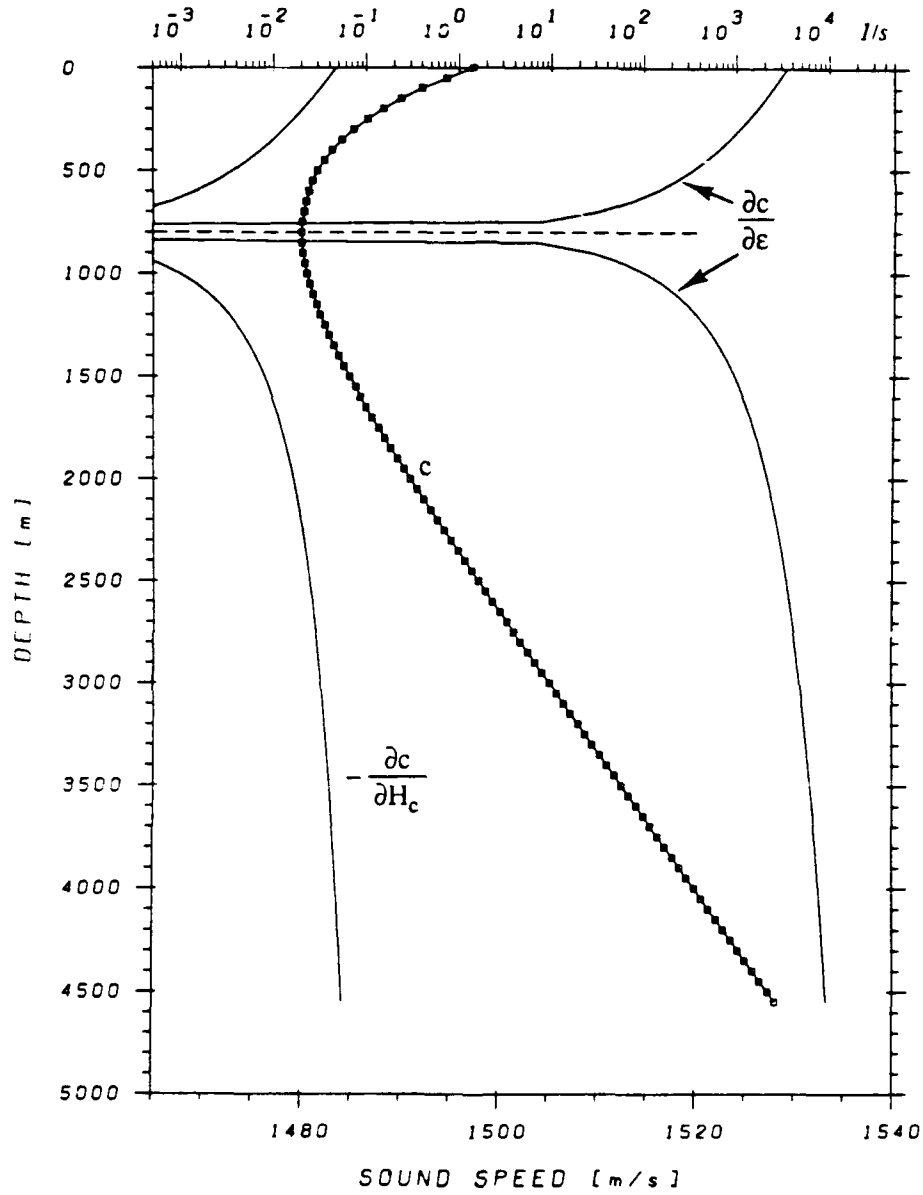


Figure 9. A canonical sound speed profile and its partial derivative  $s$  with respect to  $H_c$  and  $\epsilon$ .

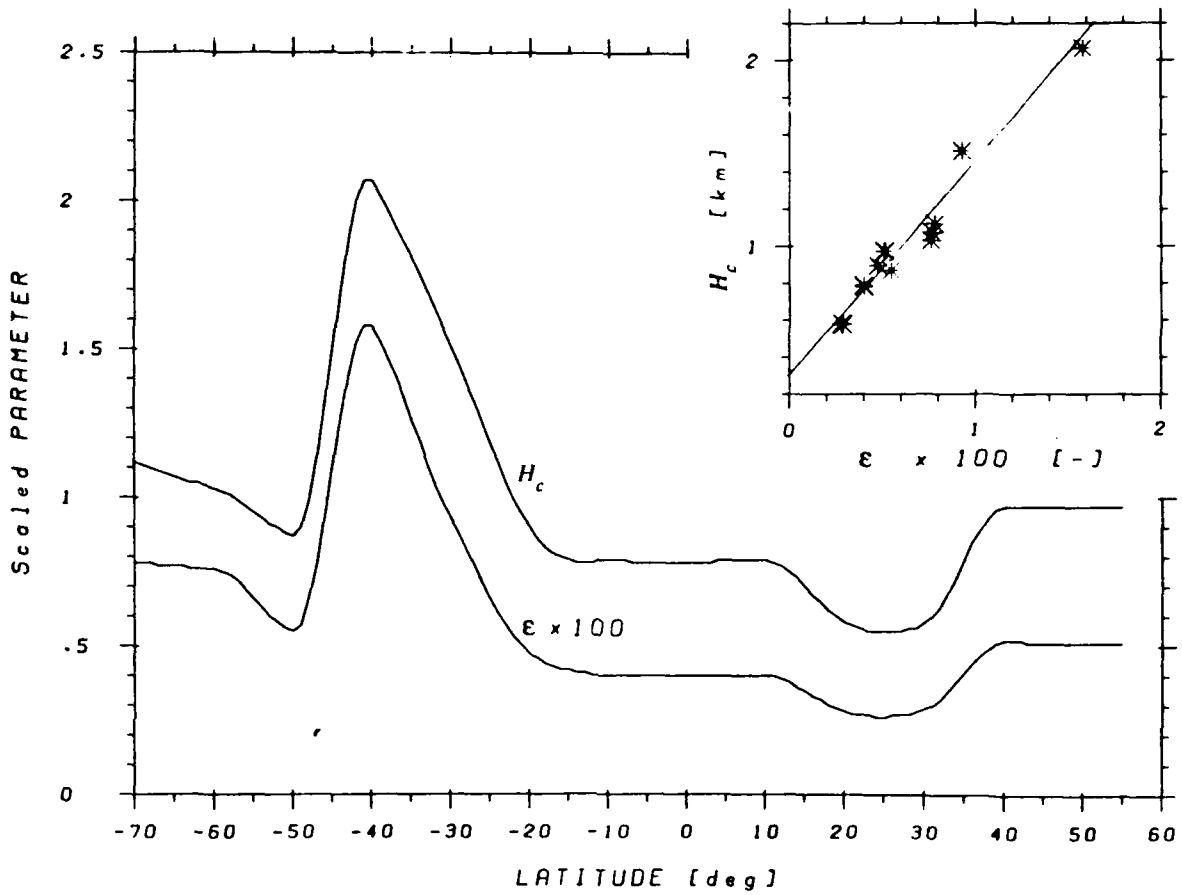


Figure 10. Canonical parameters  $H_c$  and  $\epsilon$  as a function of latitude. The insert shows the correlation between  $H_c$  and  $\epsilon$ .

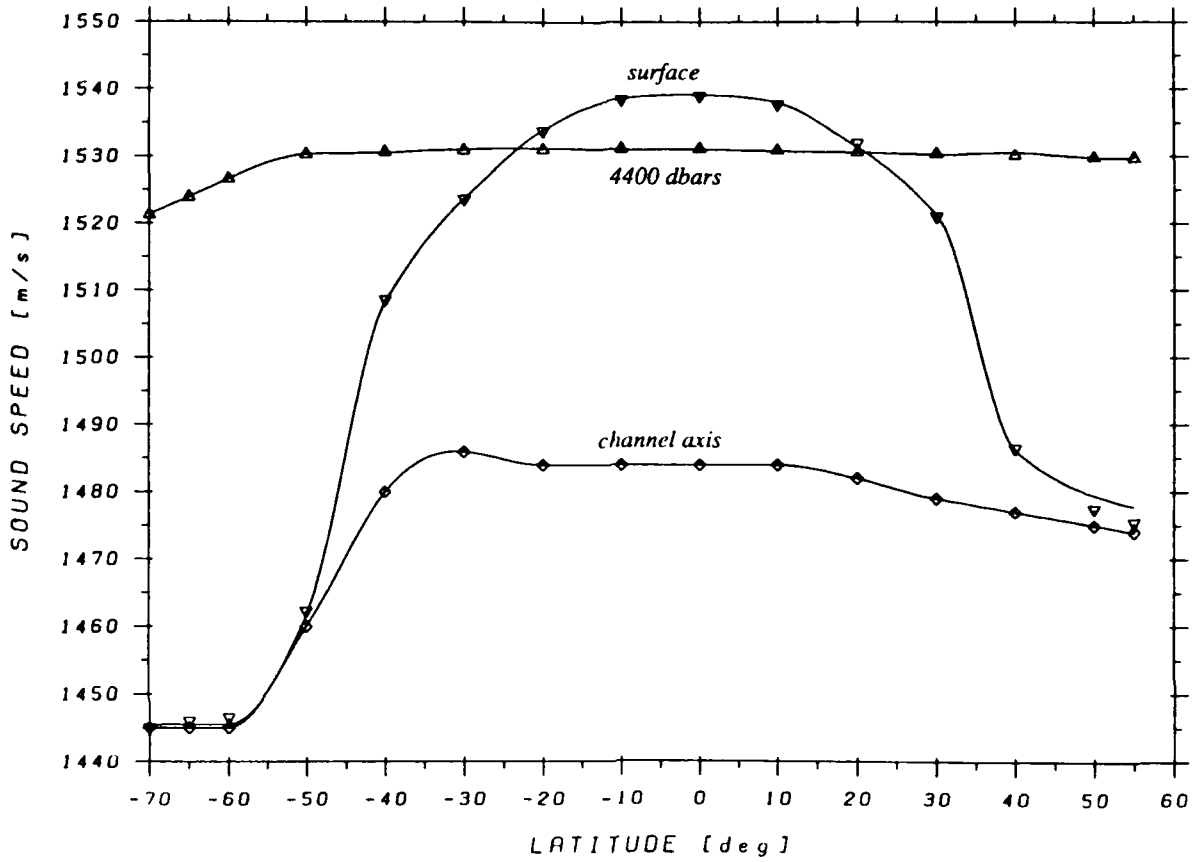


Figure 11. Tasman window sound speeds at the surface, channel axis, and 4400 dbar depth as function of latitude.

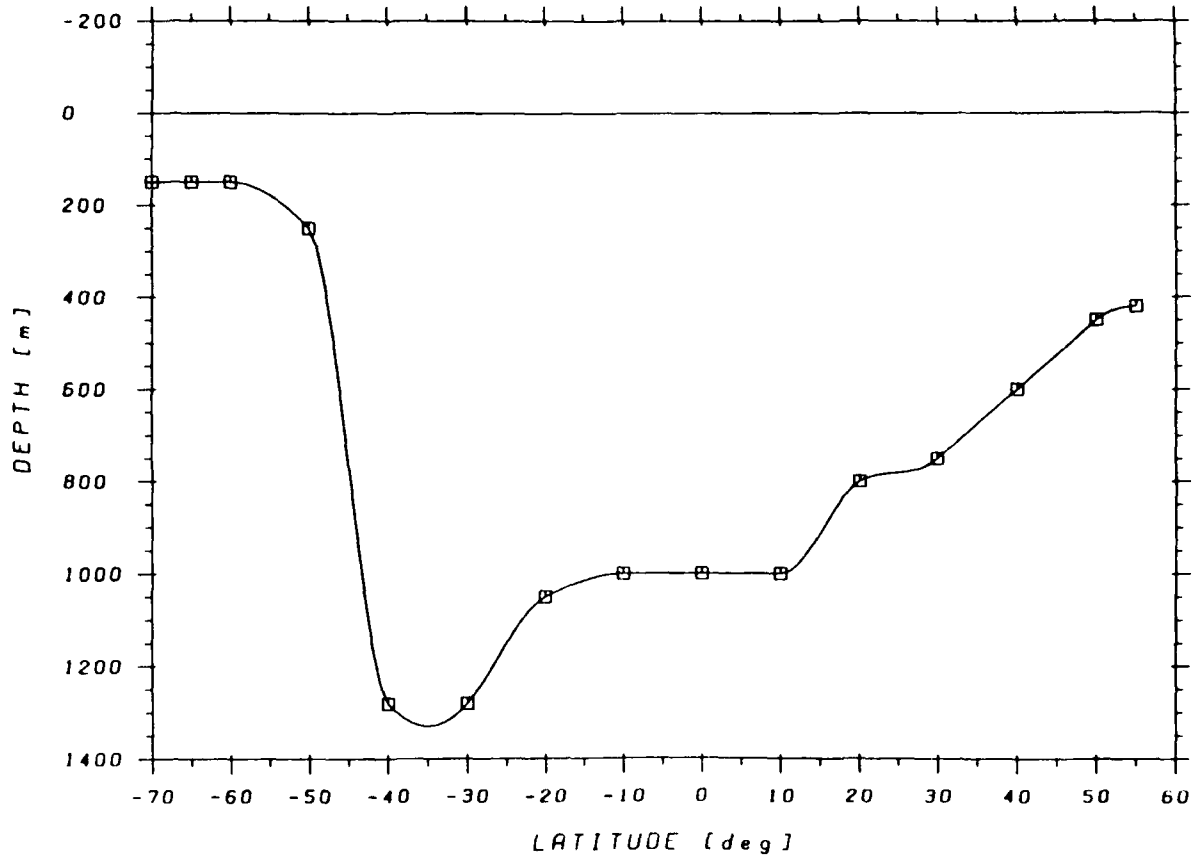


Figure 12. Tasman window sound channel axis depth versus latitude.

region of sharp horizontal changes. This, of course, is the region of the circumpolar front, albeit schematized here to a fairly narrow interval of longitude. The sharp (horizontal) frontal transitions cannot be reasonably represented by linear splines at any depth.

Akima's splines are better suited than most under such conditions, but even they show a residual oscillation artifact at depths greater than 3000 dbars (Fig. 7). Their direct analytical extension to 2-D gridded data, Akima (1974) was used in the aforementioned ray propagation model by Baxter and Orr with entirely satisfying results. The quasi-Hermite Akima splines, which were not quite "flat" enough in this application, are considered locally too flat by some spline experts (De Boor, 1978) because their second derivatives are not continuous.

Munk's SSPs are very smooth in the vertical (in terms of the number of continuous derivatives). The Akima splines are merely optically smooth in the horizontal (the first derivative is continuous), and this is all that the HARPO code requires for its predictor-corrector integration.

The composite sound speed field for the Indian/Pacific Ocean, and its partials, is easily evaluated. It obeys Eq. (21) in the vertical at any station, and the four parameters of that equation are piecewise cubic (continuous and differentiable) functions of latitude. Their spline expansion coefficients are stored into a lookup table that is embedded in the subroutine that represents the "background" ocean model conforming to HARPO's formalism.

### *Circumpolar Current Model*

When HARPO's menu is executed using the option "with current," an analytical module that provides current velocity and its partials must be supplied. We chose to model the Antarctic Circumpolar Current (ACC) as a strictly zonal current defined with a Gaussian profile in depth  $z$  and in latitude  $\theta$ , having

velocity  $u$  positive eastward:

$$u(z, \theta) = u_0 \exp \left[ - \left[ \frac{z - z_0}{\sigma_z} \right]^2 - \left[ \frac{\theta - \theta_0}{\sigma_\theta} \right]^2 \right], \quad (23)$$

where  $u \rightarrow u_0$  as  $z \rightarrow z_0$  and  $\theta \rightarrow \theta_0$ . The vertical and meridional scale parameters are  $\sigma_z$  and  $\sigma_\theta$ , respectively. They represent the  $1/e$  scale for the velocity drop-off from its maximum,  $u_0$ . The current is parametrized to satisfy an integral constraint:

$$\iint u(z, \theta) dz d\theta = S, \quad (24)$$

where  $S = 180 \times 10^6 \text{ m}^3/\text{s}$ . This value is in the midrange of estimates for the ACC transport that is known to exhibit a rather strong variability in time.

We made an *a priori* assumption about two of the parameters,  $z_0 = 200 \text{ m}$  and  $\sigma_z = 1000 \text{ m}$ , and retained a free choice for  $\theta_0$  that defines the latitude of the current axis. The parameterization was completed by demanding that  $u_0$  and  $\sigma_\theta$  be such that (23) satisfy (24). Thus, the estimation reduces to the functional dependence

$$u_0 = u_0(\sigma_\theta).$$

With  $\sigma_\theta$  large,  $u_0$  will be small; i.e., the model ACC will be wide and slow, and vice versa. A guide to a reasonable selection is provided by measured profiles of the current, e.g., as given by Kamenkovich and Monin (1978) and shown in Fig. 13. The fitted profile, also shown there, with  $u_0 = 0.314 \text{ m/s}$  and  $\sigma_\theta = 2.73^\circ \triangleq 300 \text{ km}$ , satisfies the targeted transport of 180 Sverdrups. While the meridional folding length seems somewhat modestly defined at 300 km, making it any larger would reduce the maximum core velocity to a level that would poorly match the data and would be less interesting acoustically. The actual acoustic propagation runs were made with  $\theta_0 = 45^\circ \text{S}$ .

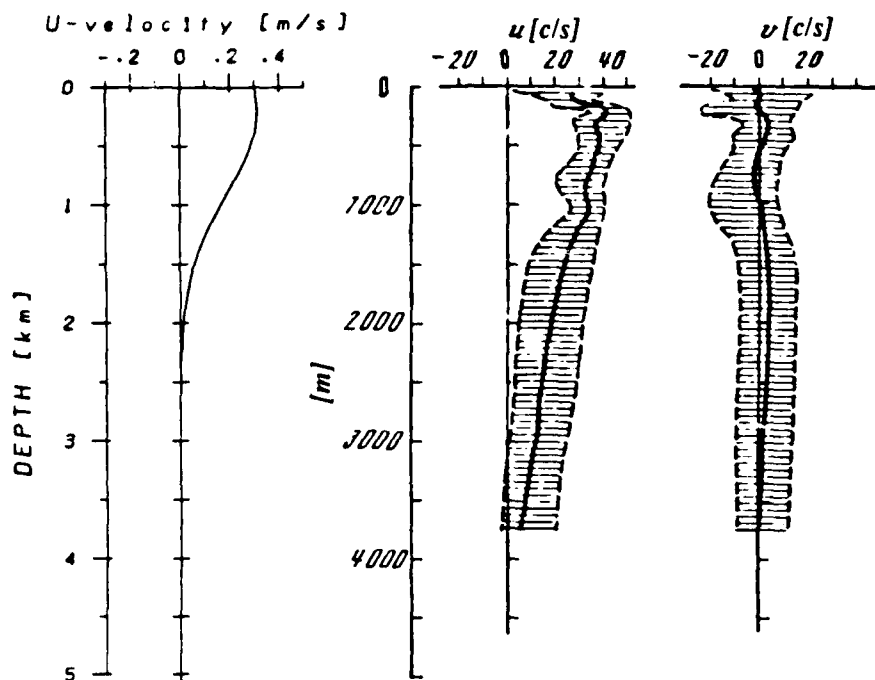


Figure 13. The Antarctic Circumpolar Current versus depth. The component speeds, after Kamenkovich and Monin (1978), are shaded to illustrate the variability.

#### 4. General Modeling Results and the Specific Eigenpaths to a Receiver Near Coos Bay, Oregon

Munk and Forbes (1989) have computed horizontally refracted paths from Heard Island through the Tasman window with launch azimuths between  $110.5^\circ$  and  $117.5^\circ$ . We compute the horizontally and vertically refracted paths of launch azimuth near  $110.5^\circ$  at small elevation angles (between  $-1.7^\circ$  and  $+1.7^\circ$ ) and obtain their arrival at latitude  $43^\circ\text{N}$  (exactly) and longitude  $232.5134^\circ\text{E}$  ( $127.4866^\circ\text{W}$ ). This is an arbitrary location off the coast of Oregon where the depth to the bottom exceeds 1500 m and the sound channel axis is estimated at 550 m depth. We place the hypothetical receiver at 547.8 m depth and seek to reach it with eigenpaths within a few meters error in latitude, longitude, and depth. The ray path length depends on the specific value of the elevation angle for a given launch azimuth; it amounts to roughly 18,092 km for these shallow launch elevation angles. The travel time is about 12,289.7 s, so the average sound speed sampled by the typical ray in this range of parameters is 1472.13 m/s.

The general modeling results demonstrate the effects of some of the remarkable oceanic features encountered along these long paths. All fundamental and qualitative features of the westward propagation originating in the Indian Ocean (not from Heard Island but from Perth) have been described by Munk et al. (1988) and by Munk and Forbes (1989) in a broader geographical context. We refer the reader to these two sources for the important notions, and concentrate instead on the resolving power of ray propagation computations, and on certain propagation features in the vertical plane.

Figure 14 shows four trajectories through the Tasman window. Two are projections of acoustic paths onto the sea surface. The other two are the transmitter-to-receiver geodesic on the WGS72 ellipsoid, and the great circle

between Heard Island and the hypothetical receiver in the northeast Pacific.

On the distance shown (much shorter than antipodal, cf. Fig. 2) the horizontal lays of the great circle and the geodesic to the receiver are not substantially different.

The acoustic eigenpath with launch azimuth  $110.5087^\circ$  and launch elevation angle  $-1.6148^\circ$  is refracted away from the geodesic "to the left," toward the "faster water." This is as expected, because it is a Fermat path. But the magnitude of the deviation (nearly 600 km at the widest point) is unexpected, and points to the importance of 3-D modeling for identifying deviations of refracted paths from a nominal vertical propagation surface that has either a great circle or a geodesic as a trace. This particular eigenpath will be further analyzed in the subsection on the search for eigenrays.

The "acoustic" path in Fig. 14 that seems to be obstructed by North Island of New Zealand is computed merely as a consistency check. It is launched with the same azimuth,  $119.1603^\circ$ , as the azimuth of the geodesic to the receiver. Because this path is not an eigenpath to the receiver, it is refracted away from the geodesic "to the right," in this case, toward the "slower water," as expected. Its elevation angle of  $-1^\circ$  is just a nominal value to expose the computation to nontrivial sound speed gradients.

Figure 15 shows the vertical oscillation of the acoustic eigenpath ( $110.5087^\circ$ ,  $-1.6148^\circ$ ) in the sound channel. Because it started in a shallow sound channel at Heard Island, its oscillation nearly reaches the surface at high southern latitude and establishes a pattern that persists along a distance of nearly 4000 km. The gentle curve with which the envelope to this trajectory comes closest to the sea surface about 2000 km down range from Heard Island attests to the Fermat behavior. To reach the distant receiver in the Northern Hemisphere, the eigenpath must first go south toward Antarctica, and there it

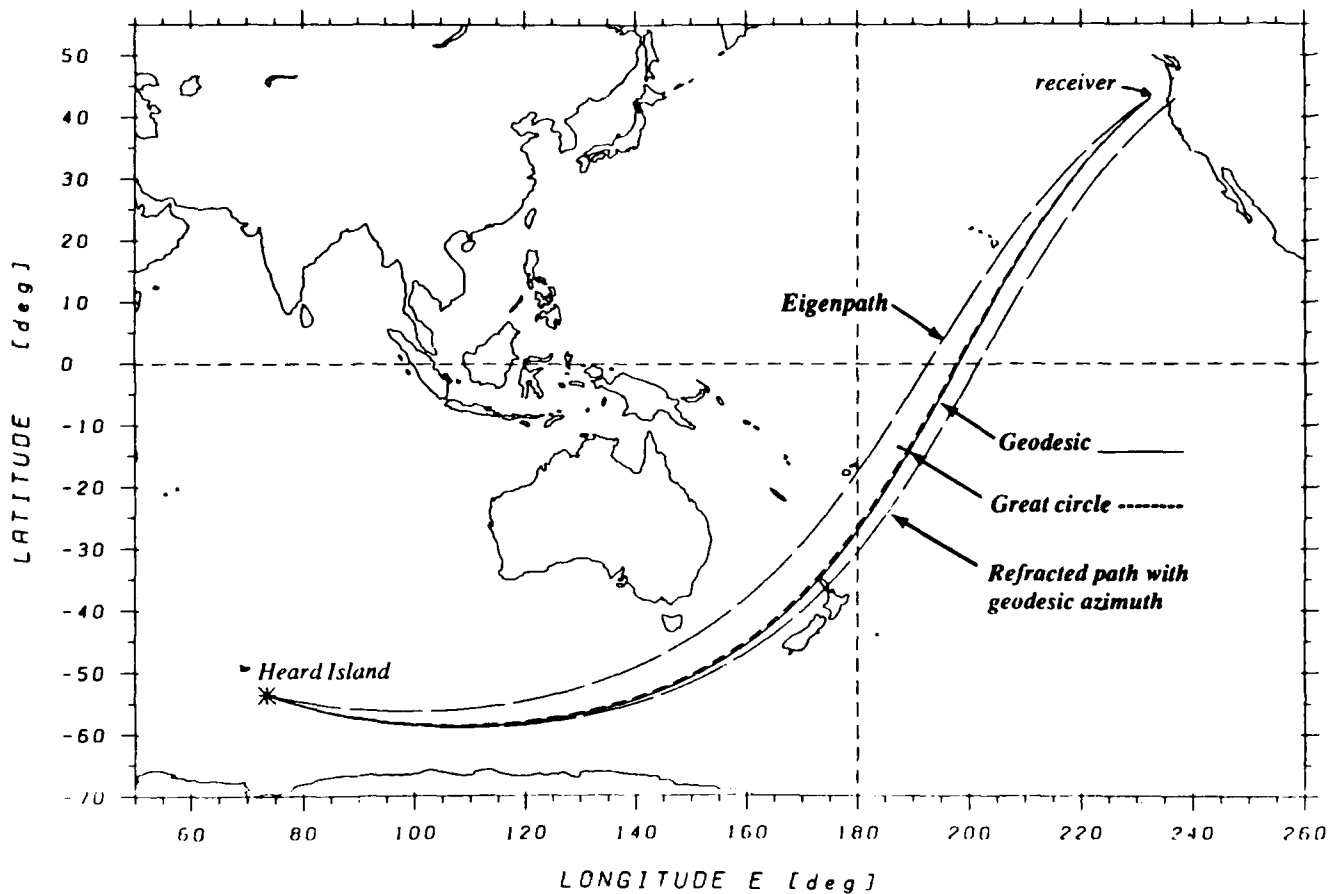


Figure 14. The surface projection of an eigenpath through the Tasman window and corresponding geodesic and great circle paths. Also shown is the refracted path having the same initial azimuth as the geodesic.

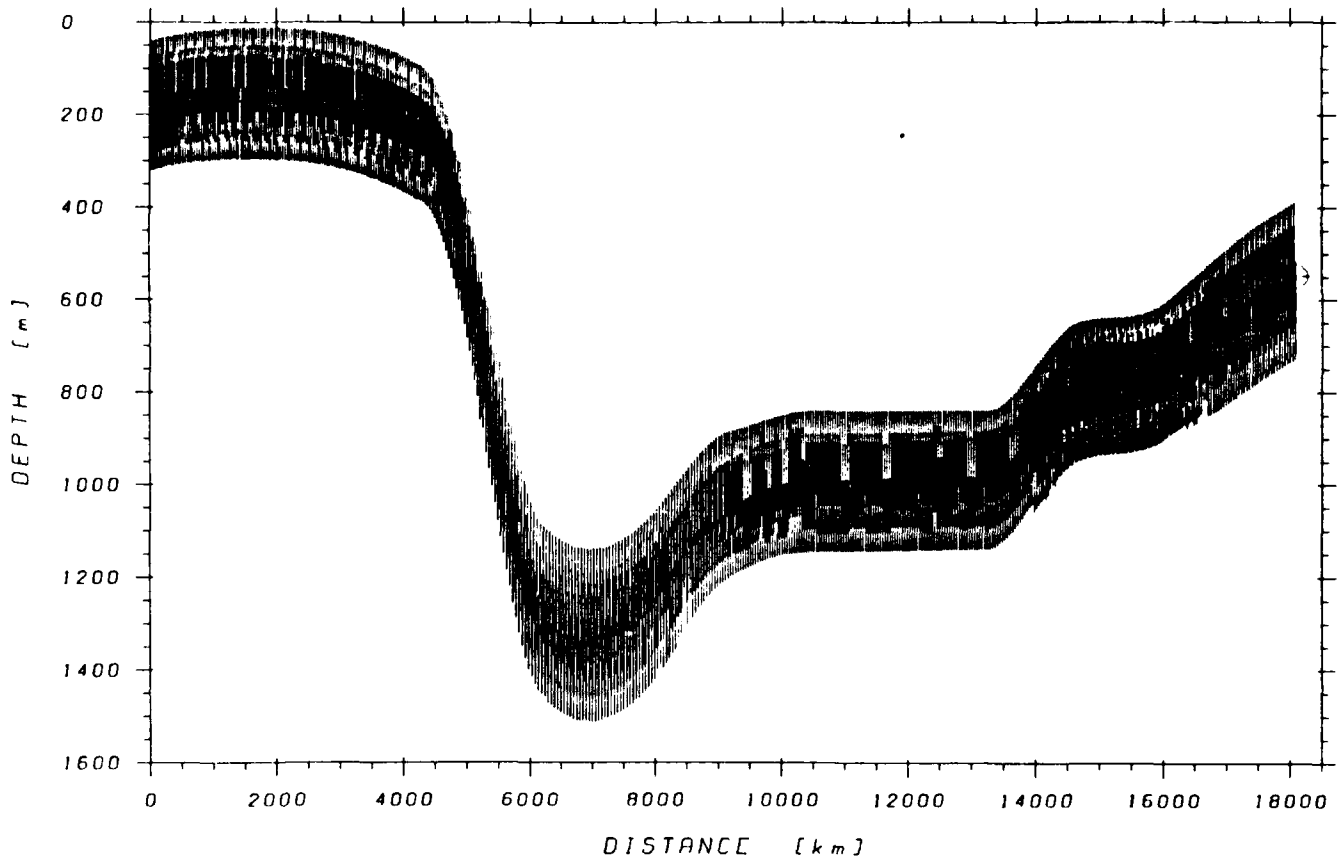


Figure 15. Vertical oscillations of the Tasman eigenpath, with an elevation angle of  $-1.6148^\circ$ , along the 18,000 km path.

travels in a channel where the axis gets shallower for quite a distance. In fact, this flat ray (elevation angle  $-1.6148^\circ$ ) is the steepest eigenray that does not experience multiple interactions with the surface. Beyond a limiting "direct" ray of about  $\pm 1.7^\circ$  elevation, all steeper rays will experience more than 100 interactions with the surface before the sound channel sinks to a greater depth in the Tasman window, cf. Fig. 12. This could result in a large scattering loss so that the corresponding paths may be hard to detect at the receiver.

Another propagation characteristic that we notice, but do not explore at this time, is the relation of oceanography, atmospheric forcing, and boundary interaction to the effective aperture of launch elevation angles for "direct" paths that will constitute the main acoustic communication link to the US West Coast. Factors that influence this relation can be anticipated from Fig. 8 by the shape of canonical SSPs that we used to model the high southern latitudes; admittedly this goes beyond Munk's (1974) expressed intention to limit the canonic profile to temperate latitudes. Regardless of how the sound profiles were modeled, the oceanography produces a sound channel that is weak, in addition to being shallow.

The Indian Ocean near Antarctica is subjected, on the average, to the highest wind stress on the globe during the Austral winter. This is evident from the SEASAT altimeter wind speeds for July–October 1978, as reported by Chelton et al. (1981), as well as from computed wind stress and wind stress curl for the same period, reported by Baker et al. (1980). The latter was part of a computational study of various atmospheric ocean-forcing fields using seven years of twice daily Australian sea surface pressure data. The wind stress in the belt between Prince Edward Island in the west and Macquarie Island in the east exceeded values of 0.4 Pa for prolonged periods. The forcing was particularly strong during the SEASAT year (1978), but it was comparably strong in three out of the seven years. Figure 16, computed

during that study, shows the average zonal wind stress and wind stress curl for July 1979, based on twice daily data for the whole Southern Hemisphere. One notices the exceptional intensity of atmospheric forcing over the southern Indian Ocean. Such forcing may intermittently destroy the sound channel, if it acts long enough. The communication link which is predicated on the existence of the channel may then be interrupted. Clearly, realistic modeling of the time dependent sound channel in the antarctic Indian and Pacific Ocean is of high priority among our future tasks.

Figure 17 shows the propagation pattern for the axial ray with launch elevation angle  $0^\circ$ . It oscillates a little in the channel, and this was unexpected. Appendix B shows that a ray launched with  $0^\circ$  elevation angle from the exact depth of the channel axis oscillates, because of earth's curvature and after an initial transient, about a mean depth that is shallower than the channel axis. Appendix A gives the analytical proof for this behavior.

### *Eigenpaths*

The customary computation of eigenrays propagating through 2-D layered media uses the "shooting method." This is one of the original techniques for numerically solving two-point boundary value (BV) problems. When used with an adaptive step integrator on a smooth problem, it has an accuracy superior to other BV solvers (finite difference, finite elements, etc.) for a comparable computational effort. The main Heard Island project will focus on monitoring a time varying communication channel in which the end-point boundary conditions remain fixed. We wondered whether a numerical method other than shooting might provide an attractive modeling alternative for computing effects of the *changes* in the channel properties, knowing that they will be localized in time and space. We did consider the shooting method to establish a set of eigenpaths at an initial time, followed by a perturbation routine for these paths at later times, but found that the accuracy

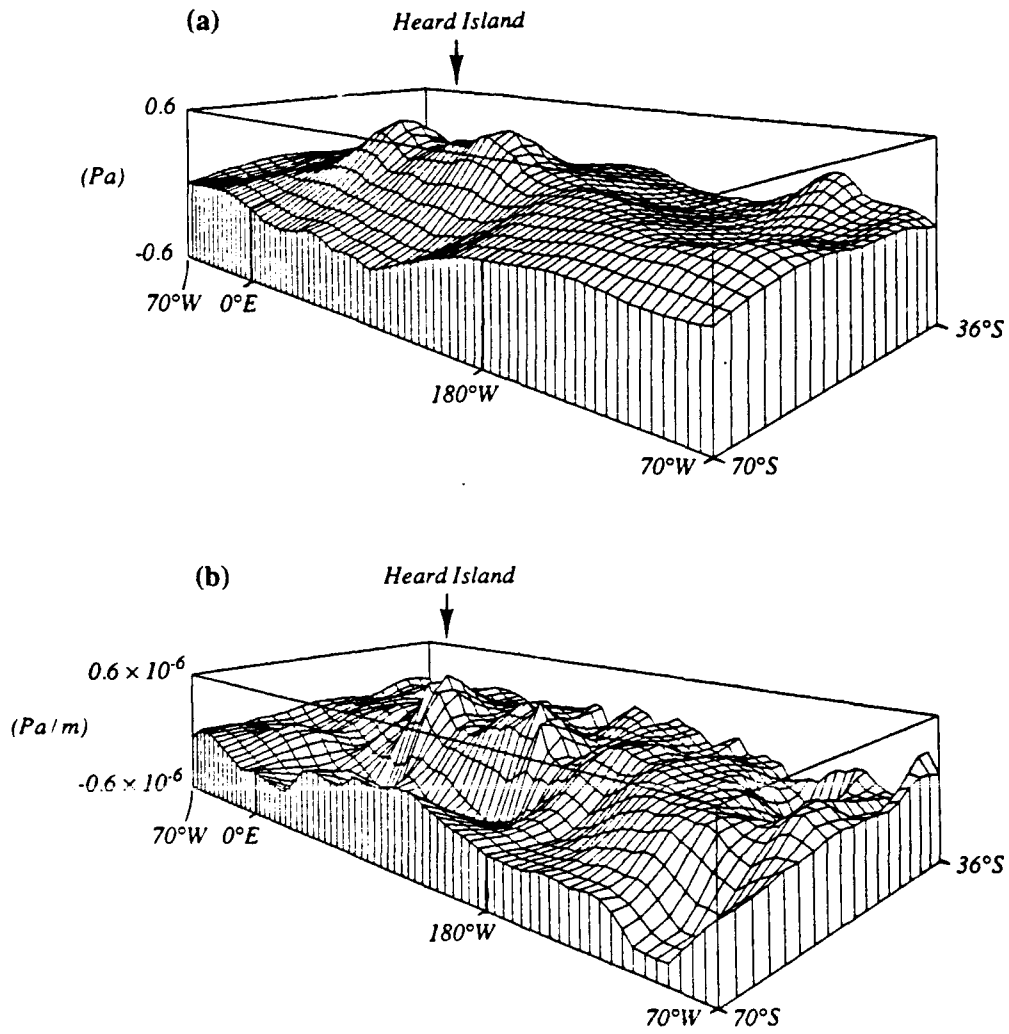


Figure 16. Average zonal wind stress and wind stress curl for the month of July 1979.

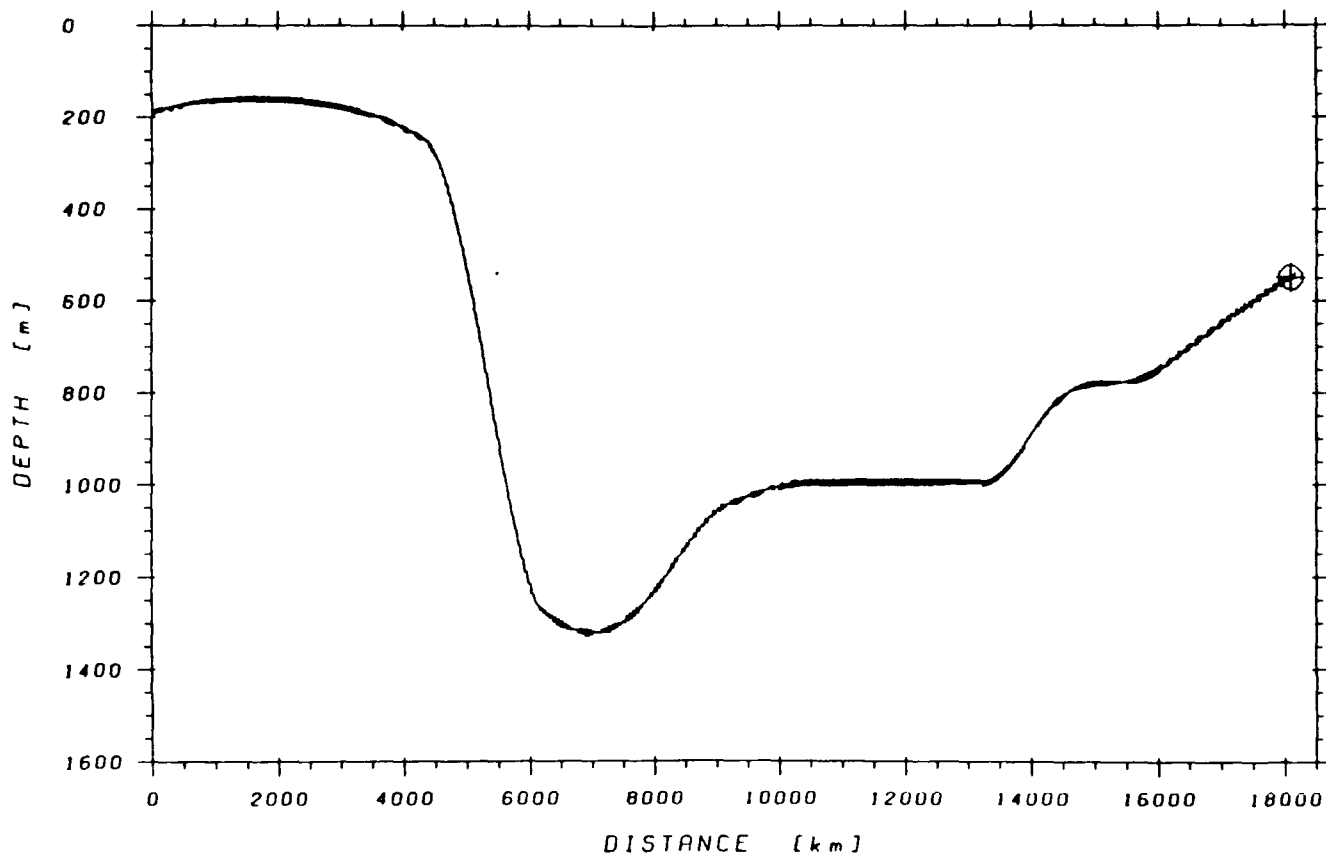


Figure 17. Vertical oscillations of the Tasman eigenpath, having an elevation angle of  $0^\circ$ , along the 18,000 km path.

consideration prevails and favors the shooting method alone.

The computational accuracy (2 m) of eigenpaths propagating over  $18 \times 10^6$  m is extraordinarily high, even for the "smooth ocean" problem (the search for effective sound paths in the "nonsmooth," possibly chaotic, case is addressed in Section 5). In relative terms, this is about 50 times more stringent than anything we had experienced before. It made us realize that search methods that are very efficient (Mercer et al., 1985) at intermediate precision levels (about 5 m on 1000 km) need further refinements.

First, it is necessary to defend the stated precision goal for eigenrays (stressing the computational rather than the physical aspect) against the argument that the targeted value is about 1000 times finer than the probable accuracy of our global travel time prediction. The answer is related to our plan to explore the expected variability of travel times for global paths. We know, for example, that mesoscale structures will cause large variations in the travel times, but that the potential annual trend from global warming is only about 100 ms. We want our estimates of variability from various sources to contain computational errors that are a small fraction of this, say 10 ms, or about 5 m or better.

Second, the eigenray search procedure must be described with sufficient precision to be implemented as an algorithm that can deal with any emerging pattern by itself, i.e., without assistance of human pattern recognition that characterized the developmental effort. The procedure relies on substantial software resources that reside on a standard library (LINPACK, Dongarra et al., 1979, or equivalent). This is in keeping with a view on computing that parallels the hardware notions of LSI and VLSI (large and very large scale integration): the software modules that are drawn upon are generic, but are the most potent one can access. We introduce this procedure by describing in

abstract terms the linearization of the inherently nonlinear relations for a ballistic targeting problem. Since the shooting method is already assumed, the ballistic notions of targeting corrections are appropriate to our underwater acoustic propagation problem.

There are two vector spaces:

- The "input" space at the transmitter, with dimensionality 3, where the variables are the launch azimuth  $\alpha$ , the launch elevation angle  $\eta$ , and the travel time  $\tau$ .
- The "output" space at the receiver. This is a real 3-D space defined in terms of latitude  $\chi$ , longitude  $\phi$ , and depth  $z$ .

It may be somewhat odd to visualize the travel time as part of the "input," rather than output, but the given allocation of variables is mathematically correct and posits the 3-D "forward" problem in clear terms. In 2-D eigenpath problems it is certainly not of any advantage to consider the travel time as an input because the ballistic analogy is for a target "on the ground," and the nearness of a miss is identified by a "spotter" (spotter algorithm) seeing the impact of the search trajectory. In the 3-D ballistic case, there is no easy way to set up the spotter algorithm, but the shooter controls the time at which the shell detonates.

This analogy carries directly over to the acoustic case in which the ray point becomes a tracer projectile that can telemeter its position at any time. However, a considerable complication arises in ray acoustics since the ray trajectory is "wavy" in the  $z$  direction due to the oceanic waveguide. This motivates a reduction of the 3-D target search to a 2-D targeting problem; however, the 3-D acoustic targeting problem is actually simpler in principle and is described first.

Consider a ray that is an eigenray. That is, in the input space there is a specific vector  $(\alpha_0, \eta_0, \tau_0)$  that corresponds to the vector  $(\chi_0, \phi_0, z_0)$ , the receiver position) of the output space.

The mapping  $(\alpha_0, \eta_0, \tau_0) \rightarrow (\chi_0, \phi_0, z_0)$  is highly nonlinear.

Now consider that the receiver is displaced a little, by  $\delta\chi = \chi - \chi_0$ , and similarly for  $\delta\phi$  and  $\delta z$ . Reestablish the eigenpath by changing the input parameters a little, by  $\delta\alpha = \alpha - \alpha_0$ , and similarly for  $\delta\eta$  and  $\delta\tau$ . Since this is done in the immediate neighborhood of an eigenpath, this mapping is linear, and is described by

$$\begin{bmatrix} \frac{\partial\chi}{\partial\alpha} & \frac{\partial\chi}{\partial\eta} & \frac{\partial\chi}{\partial\tau} \\ \frac{\partial\phi}{\partial\alpha} & \frac{\partial\phi}{\partial\eta} & \frac{\partial\phi}{\partial\tau} \\ \frac{\partial z}{\partial\alpha} & \frac{\partial z}{\partial\eta} & \frac{\partial z}{\partial\tau} \end{bmatrix} \cdot \begin{bmatrix} \delta\alpha \\ \delta\eta \\ \delta\tau \end{bmatrix} = \begin{bmatrix} \delta\chi \\ \delta\phi \\ \delta z \end{bmatrix}. \quad (25)$$

We call the Jacobian matrix on the left of Eq. (25)  $\mathbf{J}$ , and note that its elements can be estimated from information provided by three search rays in which a single input parameter is varied at a time. The finite difference estimates of the partials in  $\mathbf{J}$  are thought to be evaluated relative to a ray point that coincides with the receiver. But such a point is not available, and so some other close point must be used. Also, note that the initially perfect eigenpath condition satisfies Eq. (25) in the trivial but valid form

$$\mathbf{J} \cdot \vec{0} = \vec{0}.$$

One can reverse the reasoning and consider (25) not as a vehicle for restoring the eigenpath condition for a slightly displaced receiver, but as the means of establishing an eigenpath when a receiver in a fixed position was missed by a ray having nominal launch parameters (i.e., such that their deviation from the nominal value  $(\alpha_0, \eta_0, \tau_0)$  is the null-vector). Assume that the amount of miss is  $(\delta\chi, \delta\phi, \delta z)$ ; then the left-hand vector  $(\delta\alpha, \delta\eta, \delta\tau)$  of the nontrivial (25) is exactly the corrective amount to be applied to the launch parameters in order to exactly reach the receiver.

There is a vexing problem with (25) as it stands, because the matrix condition number of  $\mathbf{J}$  tends to be very bad unless  $\mathbf{J}$  is evaluated near the receiver. It easily exceeds  $10^4$ , and balancing it by scaling is not a practical option. Instead, one wants to reduce the dimensionality of the problem. This is why it is useful to have written (25) in full, to recognize that involving  $z$  and  $\tau$  in the scheme (one in the output space and the other in the input space) causes the trouble. For any given scaling, it turns out that  $\partial\chi/\partial\tau$  and  $\partial\phi/\partial\tau$  will be relatively small (because of  $\tau$ ), while  $\partial z/\partial\alpha$  and  $\partial z/\partial\eta$  will be relatively large (because of  $z$ ). To eliminate both, one sets  $\delta\tau = 0$  on the left and  $\delta z = 0$  on the right, which results in the reduced system

$$\begin{bmatrix} \frac{\partial\chi}{\partial\alpha} & \frac{\partial\chi}{\partial\eta} \\ \frac{\partial\phi}{\partial\alpha} & \frac{\partial\phi}{\partial\eta} \end{bmatrix} \cdot \begin{bmatrix} \delta\alpha \\ \delta\eta \end{bmatrix} = \begin{bmatrix} \delta\chi \\ \delta\phi \end{bmatrix}. \quad (26)$$

Two germinal ideas were introduced in the eigenray search scheme of Mercer et al. (1985). The first was to eliminate the dependence of the launch parameter correction on  $z$  at the onset. The second idea was to institute a nonlinear (global) procedure whereby a set of search rays (with associated "ridge" numbers) identifies a set of eigenrays.

The nonlinear procedure is very effective because it functions even for large "miss" distances; in our application this is about 30 km along-path and about 1 km across-path. However, on the 30 km scale the essence of the nonlinearity cannot be captured by just a few search rays, so the eigenray error after this zeroth iterate may be about 100 m. Then, the nonlinear algorithm must be repeated, or the linearization using (26) may be substituted.

The idea and execution of the nonlinear search procedure is described now in some detail. Figure 18 shows the regular pattern of 16 search rays at two closely spaced azimuths,  $110.50^\circ$  and  $110.51^\circ$ , and 4 eigenrays that were located by this search pattern. This is a diagram

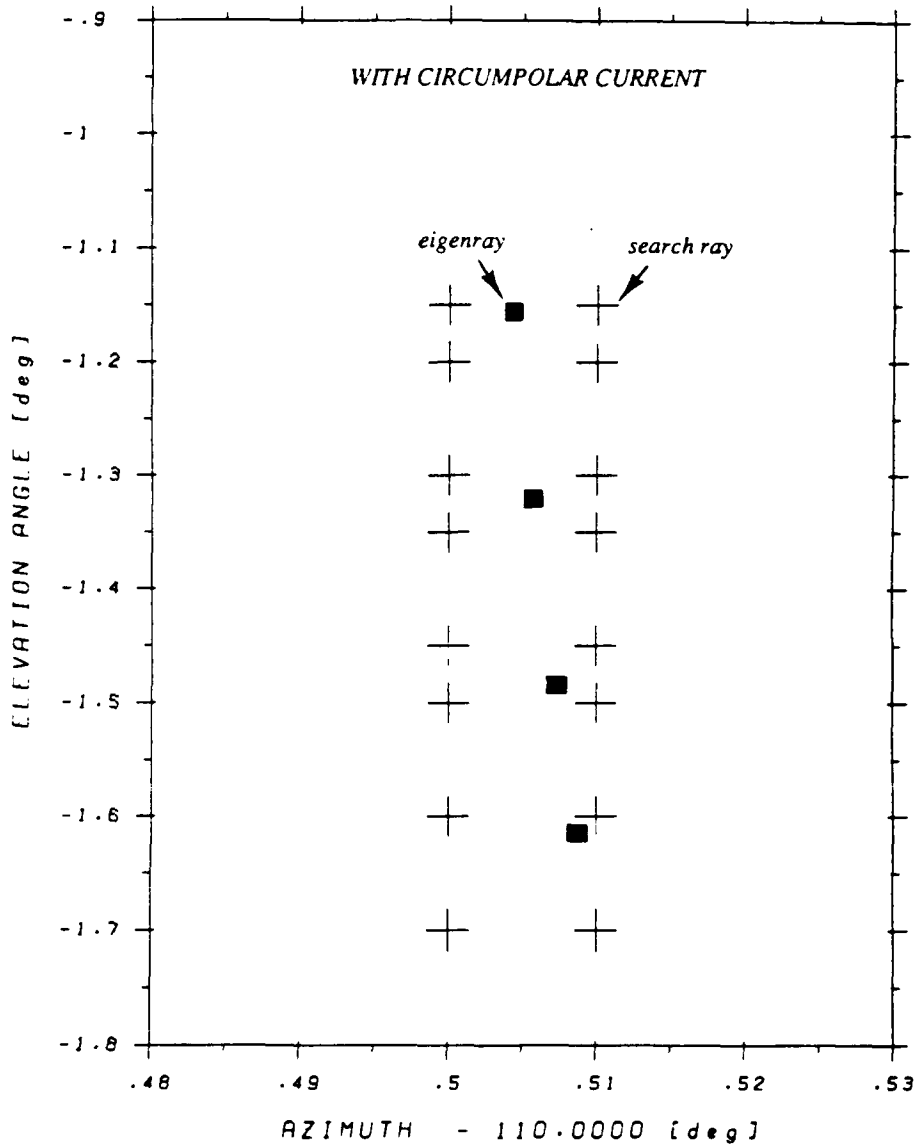


Figure 18. The initial elevations and azimuths of 16 search rays and 4 corresponding eigenrays through a Tasman window with circumpolar current.

for a "start and end result" of the eigenray search. It depicts exclusively the setup of parameters in the "input" space.

In adapting the nonlinear procedure of Mercer et al. (1985) to the very large distance and very high accuracy problem, we had to modify some of the assumptions:

- Two azimuthal search patterns, as shown in Fig. 18, are a minimum requirement. The rays have to straddle the receiver in the "output" space; i.e., their search ray parameters have to straddle the eigenray parameters in the "input" space. This is needed for interpolation, and with only two azimuths this interpolation will of necessity be linear.
- The idea of relating the "receive" azimuths to the "launch" azimuths, which enabled Mercer et al. to complete the search with only one azimuthal pattern, must be dropped. It worked for the specific propagation geometry there, but it does not work here, and so probably does not work under conditions that are sufficiently general.
- The "range" to the receiver is not defined for the precision computations. This is because in a strict 2-D acoustic problem the (horizontal) range to the receiver together with the depth of the receiver provides a complete and consistent specification of the geometry; in a 3-D problem, or even in a 2-D scheme that is derived from a 3-D problem, the eigenray paths are not in a single surface, so a unique horizontal range to the receiver cannot be defined with sufficient accuracy.

An "along-path" distance to aid the nonlinear search can be defined, but it has a slightly strange geometry as will seen in the discussion about "ridge" numbers. Also, a suitably defined "range" variable is still valuable for display of computed results. One must be cautious, though, how such a variable gets quantified by the set of ray tracing equations.

This along-path range is a parasitic variable (i.e., its coupling to the ray equations is

one-sided), but it should not be computed from the output of the ray equations. If this was done, accuracy would be lost because of the different rate of step convergence (i.e., the accumulation of output data is at most of first order, but the ordinary differential equation (ODE) solver is of higher order). Instead, an additional differential equation should be used that shares the internal linkages in the ODE solver but literally skims the surface of the earth's ellipsoid. HARPO, as available to us, does not have that equation.

#### *The "Ridge" Concept*

The elimination of the  $z$  dependence is obtained by saving the  $\chi$  and  $\phi$  coordinates of the ray point as a ray crosses the depth of the receiver—possibly many times for rapidly oscillating rays. Visualize now the surface (horizon) of the receiver depth over a wide area centered on the receiver's latitude and longitude; then imagine a fan of rays of constant launch elevation angle  $\eta$  being swept out by changing the launch azimuth  $\alpha$  in a continuous manner. Without loss of generality, let the ray paths oscillate as they would in the sound channel, and visualize the 3-D shape of the surface created by the ray points. It looks like a wavetrain inasmuch as it has pronounced crests and troughs, i.e., ray "turning" points. These need not be perpendicular to the propagation path. Now assign a sequential number to the consecutive turning points. This is customary practice, usually implemented by +/- numbers, but for the search algorithm to be presented it is more efficient (for use of lookup tables) that this numbering be simply by positive cardinals. We use the term "ridge numbers" to name these cardinals. The +/- convention, if desired, is inferred by the even/odd ridge numbers. For the Tasman window path, the neighborhood of the receiver off Oregon is reached by shallow angle ray paths after about 917 turning points, so some eigenrays can be expected when the ridge number counter displays values between 915 and 920.

Now visualize the intersection of the receiver horizon with the wavetrain surface (such a cut is almost assured by the usual geometries). The set of these cuts consists of distinctly separate smooth curves (with smoothly varying  $\chi$  and  $\phi$  coordinates) in the receiver horizon. Each of the curves is identified by the ridge number of the preceding turning point.

Keep in mind this characterization: the described wavetrain is associated with a single launch elevation angle  $\eta$ , and each curve is parameterized along the curve by a continuum of launch azimuths  $\alpha$ . What happens when the elevation angle changes a little? The wavetrain advances or recedes a little, and the cut curves advance or recede with it. This much visualization is essential for understanding the abstract scheme.

In the context of Eq. (26), and recognizing that the receiver is at a fixed  $\chi$  and  $\phi$ , the described cut curves are a *thin* solution subset in  $\delta\chi$  and  $\delta\phi$  (relative to the receiver position) that exactly satisfies  $\delta z = 0$ . Only a few discrete points on the cut curves are computed, and any collection of these points is referred to as a "cut set." There is a practical hierarchy in aggregating cut sets for efficient information processing. As will be shown, at the top is a chosen launch azimuth and at the bottom there are two typical groupings: several ridge numbers at a given launch elevation angle, or several elevation angles at a given ridge number. Now, the additional objective of the search procedure is to render  $\delta\chi = 0$  and  $\delta\phi = 0$ . If one were sure that some cut curve, and a known point on it, were in the linear neighborhood of the receiver, one could solve (26), evaluate the  $\delta$ 's, and estimate the partials at that point.

In the more general (nonlinear) geometry the search algorithm has a clearly definable task: it advances the cut curves (by changing the launch elevation angle) until one of them sweeps across the receiver position. The elevation angle at that moment becomes the eigenray

launch elevation angle, and the launch azimuth is read along the cut curve at the receiver position. Note that when we speak of angles we are strictly referring to the input space variables.

Graphically, this search procedure is easy, but computationally it is not so easy. The main problem is that the pattern recognition requires several azimuths and elevation angles, and this is expensive. Acquiring a number of ridge cut coordinates for a given elevation/azimuth is inexpensive, and they need to be stored because they are not going to be used in the sequence in which they were computed. The next six figures will explain in detail how the outlined algorithms are applied in practice.

Figure 19 displays cut sets for four ridge numbers (#916-#919) in the 30 km neighborhood about the receiver (which is taken as the origin of the local coordinates). Six ray trajectories are involved in this computation. The input space includes the two azimuths of Fig. 18 and the three bottom-most elevation angles in that figure ( $-1.5^\circ$ ,  $-1.6^\circ$ , and  $-1.7^\circ$ ).

Figure 20 is a detail of Fig. 19. It displays the cut set for ridge #917 at two elevation angles ( $-1.6^\circ$  and  $-1.7^\circ$ ). Four ray trajectories are involved in this display, but they are pairwise so close (at same azimuth) that only two traces are distinct. The displayed cut set of four points will help locate the bottom-most eigenray shown in Fig. 18. That eigenray is the one discussed in conjunction with Figs. 14 and 15. It has launch azimuth  $110.5087^\circ$  and launch elevation  $-1.6148^\circ$ . Note: When we cite eigenray angles to  $10^{-4}^\circ$ , the resolved values are at least 10 times finer because the sensitivity of the launch angles  $\alpha$  and  $\eta$  to a unit distance error is about  $3 \times 10^{-5} \text{ }^\circ/\text{m}$ .

While the foursome of search rays closest to that eigenray, in terms of launch parameters of Fig. 18, helps identify the approximate parameters for launching the eigenray, it does not provide sufficient information to attain the desired accuracy. The complete search pattern in Fig. 18 has to be used at once, but then one

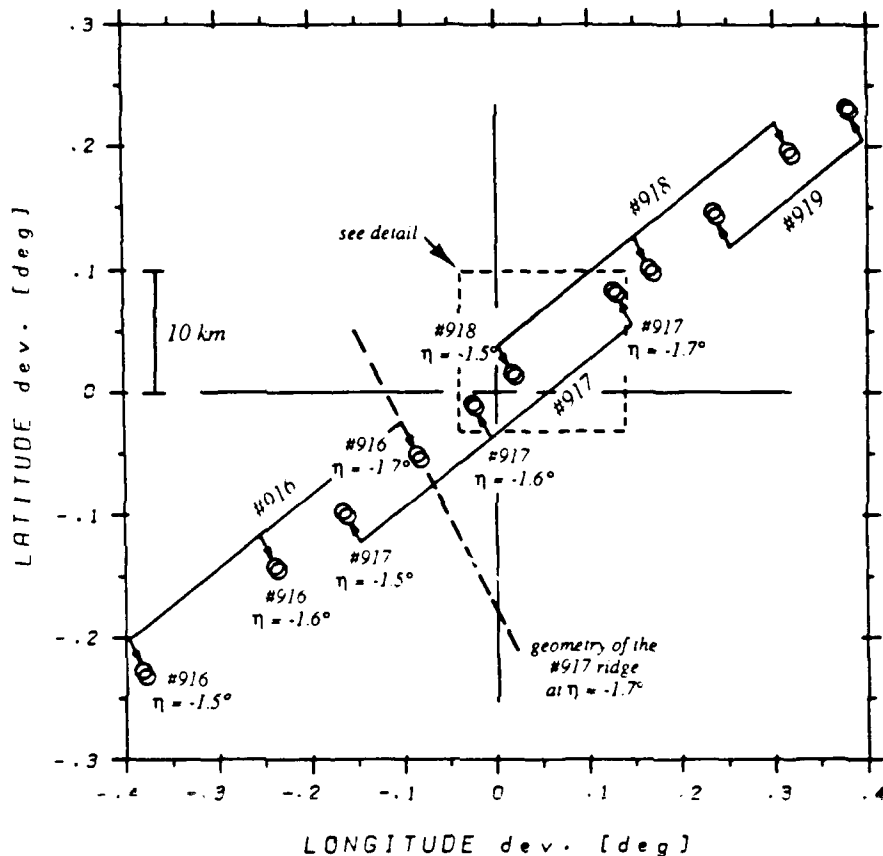


Figure 19. Positions at which various rays pass through the depth of the receiver in the vicinity of the receiver. Labels for the cumulative number of ray turnings help one visualize the formation of ridge cut sets.

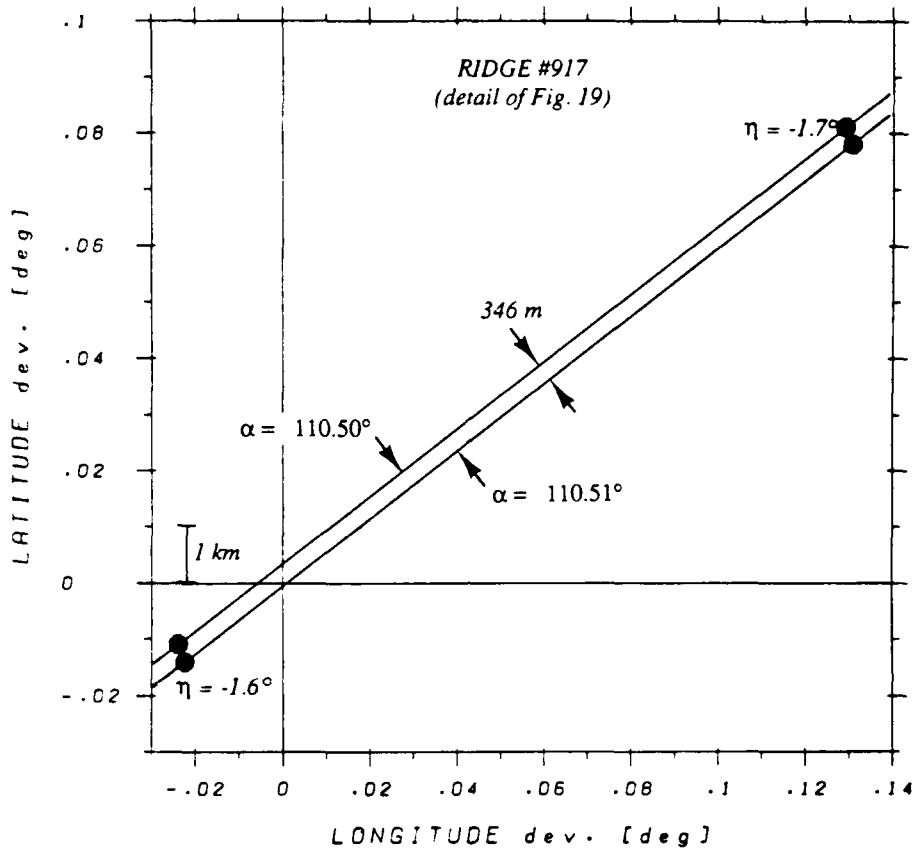


Figure 20. Blowup of the insert area from Fig. 19 showing the cut set for ridge #917 at elevation angles of  $-1.6^\circ$  and  $-1.7^\circ$ .

expects that several eigenrays can be identified in one operation. The geometrical idea of the combined procedure is to "advance" the ridges, find the appropriate launch elevation angles at a given azimuth, repeat the process for a different azimuth, correct the elevation angles if necessary, and determine the appropriate launch azimuth for each eigenray found.

The linear algebraic equivalent to the geometrical idea is not a direct one. This is because the geometry displayed in Figs. 19 and 20 is curved. The trajectories (Fig. 20) are curved, and the ridge (e.g., #917 in Fig. 19) is not orthogonal to the trajectories. The along-path miss distance of a cut set point  $(\chi, \phi)$  from the receiver at  $(\chi_r, \phi_r)$  should be parallel to the footprint of the ray trajectory, and the cross-path miss distance of the same point should be parallel to the ridge. A glance at Fig. 20, which is to scale, shows that this geometry describes a trapezoid with four slightly curved sides. The displayed 1 km bar in Fig. 20 shows that the curvature, slight to the eye, may not be slight when compared with a 2 m or even 5 m scale.

A formalism intelligible to the machine is needed to cope with this nonlinearity. The full formalism is too long to show here. Its main element computes *oblique projections*, and it does this by combining orthogonal projections, inner products, and trigonometry. The task becomes much simpler when there is no obliqueness; i.e., when the trapezoid in Fig. 20 becomes a rectangle. This variant is shown in full below. The relevant point is that while one could compute the along-path and cross-path miss distances from the "nearest" trapezoid to the receiver, these oblique projections are still linear entities. However, if one computes the miss distances based on many trapezoids, some of which are not near the receiver, one obtains inputs to construct the nonlinear curves that are the key to high accuracy in determining eigenrays. This will be discussed shortly. The simplified formalism follows.

The cut set point characterized by the  $i$ -th launch elevation angle  $\eta_i$ , and the  $j$ -th ridge number  $R_j$  (a single azimuth is assumed, and no special notation is assigned to it) maps the "descriptor"  $(\eta_i, R_j)_k$  into the latitude longitude position  $(\chi_k, \phi_k)$ , where  $k$  is an integer. To operate locally in a linear approximation, we limit  $k$  to  $(0,1)$ . The ridge numbers are by definition consecutive integers; i.e.,  $R_{j-1} = R - 1$ .

The procedure has the following steps:

- (1) for  $i = 1, 2, \dots$  choose  $\eta = \eta_i$ ,  
and for  $j = 1, 2, \dots$  choose  $R = R_j$ ,
- (2) define  $P_0 = (\eta, R) \Rightarrow (\chi_0, \phi_0)$ ,  
and define  $P_1 = (\eta, R-1) \Rightarrow (\chi_1, \phi_1)$ ,
- (3) define vectors  $a^T = -(\chi_1 - \chi_0, \phi_1 - \phi_0)$ ,  
and  $b^T = (\chi_r - \chi_0, \phi_r - \phi_0)$ ,  
{determine scalar  $\lambda$  such that  $a^T(b - \lambda a) = 0$ },
- (4) evaluate  $\lambda = (a^T b) / (a^T a)$ .

Steps (3) and (4) implement an orthogonal projection of  $\vec{b}$  onto  $\vec{a}$ .

This procedure yields the "status" of the cut set point  $P_0$  relative to the receiver.  $P_0$  exhibits an along-path miss distance  $\delta_r$ ,

$$\delta_r = |\lambda a|,$$

and a cross-path miss distance  $\delta_c$ ,

$$\delta_c = |b - \lambda a|.$$

The signs of  $\delta_r$  and  $\delta_c$  must be determined by the supervisory algorithm of the model such that  $\delta_r$  is positive when  $P_0$  "overshoots" the receiver, i.e., misses it in the direction of increasing range;  $\delta_c$  is positive when  $P_0$  misses the receiver in the direction of increasing azimuth.

A set containing 64 values of  $\delta_r$  is displayed by the curves in Fig. 21. This large number is accounted for by two azimuths, eight elevation angles ( $\eta_i$ ) for each azimuth, four ridges ( $R_j$ ) for each elevation angle. The four along-path miss values tend to be large, and the

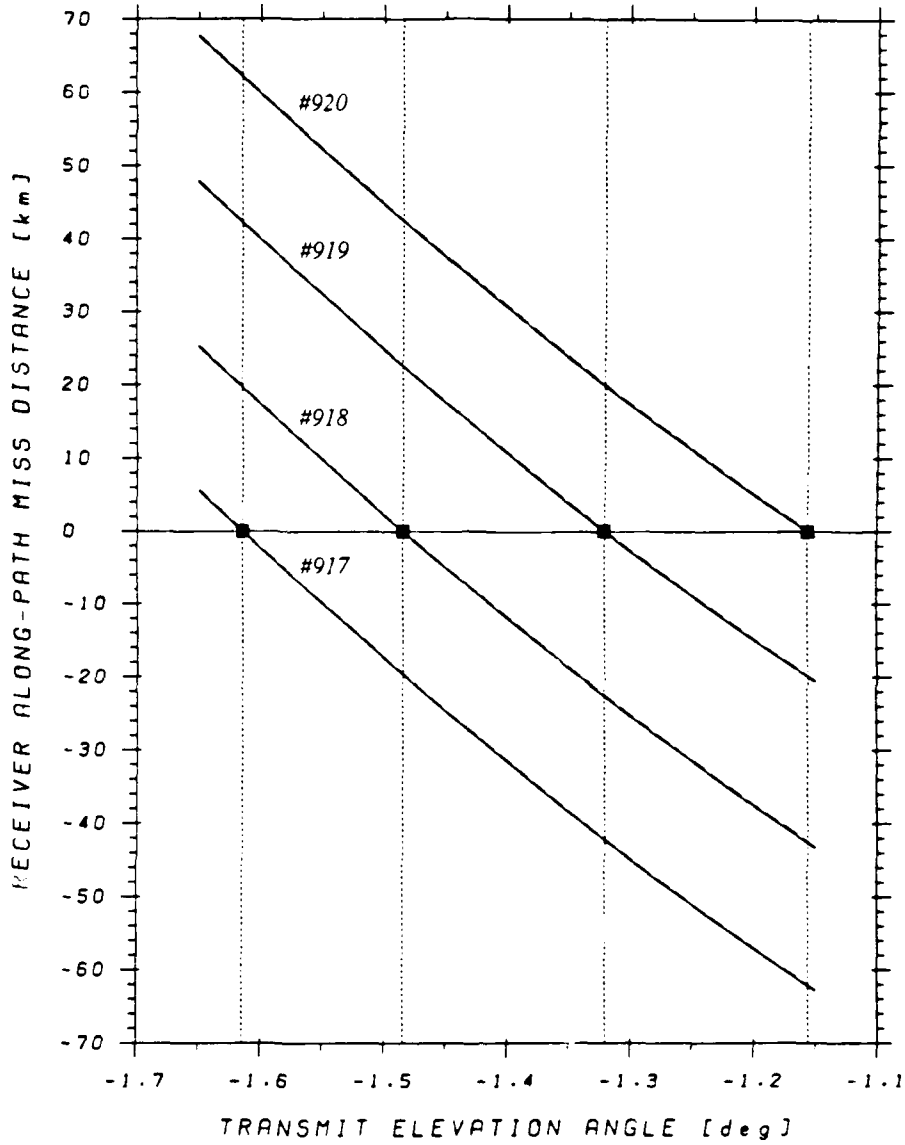


Figure 21. Along-path miss distance versus initial elevation angle for ridge numbers 917 through 920. The square blocks indicate proper choices for eigenray initial launch angles. Each ridge consists of data from two azimuthal angles  $0.01^\circ$  apart, but they are not visibly different on this plot.

two azimuths can hardly be separated in Fig. 21. There are eight curves in the figure, but only four are distinct. They link cut set points that are associated with the same ridge number. The intersections of the curves with the "zero miss" line yield the launch (transmit) elevation angles for the eigenrays.

Figure 22 displays the 64 values of  $\delta_c$  in two sets of 32 because the azimuthal dependence is well resolved here. Consequently, there are two distinct sets of four curves. Recall from the previous exposition that an intersection of these curves with the "zero miss" line cannot yield information about the launch elevation angles. The cross-path miss distances are parallel to the ridges, and the elevation angles were already determined from the construct of Fig. 21. By marking the eigenray elevation angles in Fig. 22, one can seek the intersection of each of these lines (vertical in Fig. 22) with a particular curve that carries exactly the same ridge number as the corresponding curve that gave the particular eigenray elevation angle in Fig. 21. For example, the two curves #917 are associated with the launch elevation angle  $\eta = -1.6148^\circ$ . The two  $\delta_c$  at that value of  $\eta$  show that the cross-path miss relative to  $\alpha = 110.51$  is small (about 50 m) and positive, while  $\delta_c$  relative to  $\alpha = 110.50$  is large (about 300 m) and negative. The appropriate azimuth for this eigenray is obtained by interpolation and is estimated at  $\alpha = 110.5086$ . This pair of values ( $\alpha, \eta$ ) is shown in Fig. 18 as the bottom-right eigenray.

Figure 23 corresponds to Fig. 18, except that the HARPO runs were made without including the Antarctic Circumpolar Current. The search ray parameterization was kept the same as in Fig. 18 (which did include the ACC). One reason for this setup was that switching the ACC on and off was much easier than changing search parameters; the other reason was to see whether the search procedure was robust enough to produce a good estimate of the eigenray parameters even when the receiver was not azimuthally bracketed. The results were good;

the eigenrays parameterized by Fig. 23 have a surprisingly small final error, less than 2 m.

The various segments of this eigenray parameter search procedure were implemented by calling a number of LINPACK routines, for linear algebra, root seeking, etc. They could not be used with HARPO on-line, and there was no sufficient reason to embed them in HARPO's modules. The implication is that the era of self-contained computer models is on the wane, because so much more can be done nowadays by adopting a software architecture that is loose and library oriented.

## 5. Discussion

### *Perspective*

The original intent of this work was to introduce earth ellipsoidal coordinates into a 3-D Hamiltonian ray tracer and suitably modify HARPO while maintaining its software architecture and I/O structures. After completing this task, the intent was to explore fundamental propagation conditions along the "Tasman" path, and possibly replace HARPO's integrator (a predictor-corrector) with a "marching" integrator that would be better suited for stiff problems. It was not the usual multiscale stiffness that was expected in future applications, but its equivalent that would accrue from using nonsmooth cellular data to characterize the ocean.

A number of additional and demanding tasks were on the horizon, all of them associated with developing modeling software for preparing and interpreting the Heard Island feasibility and long-term acoustic monitoring experiments. These considerations started to become dominant, not only because the prospective applications were important, but also because it became evident that HARPO was not a viable base for work on this second group of objectives no matter how much effort was spent on it.

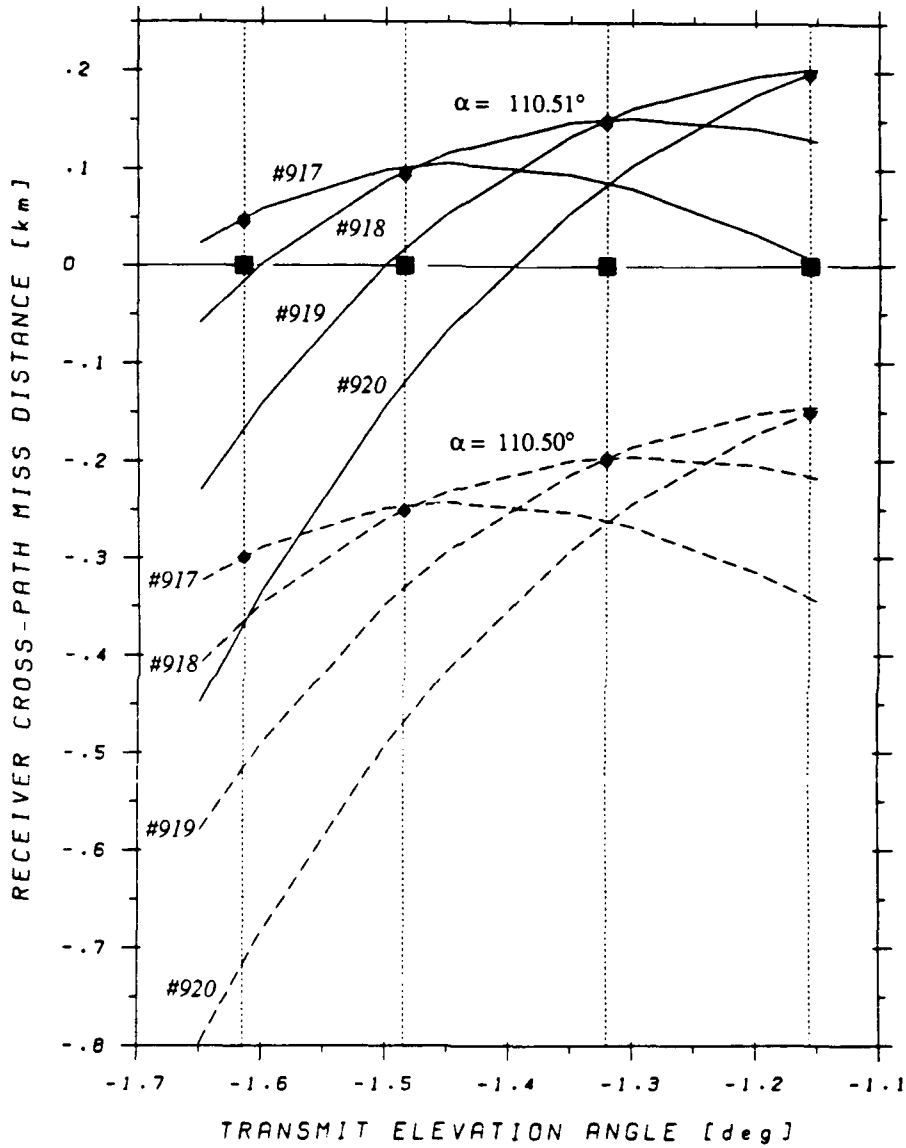


Figure 22. Cross-path miss distance versus initial elevation angle for ridge numbers 917 through 920. In this dimension the ridge cut sets for azimuths of  $110.50^\circ$  and  $110.51^\circ$  are clearly separable. The dashed vertical lines indicate the eigenray initial elevation angles from Fig. 21.

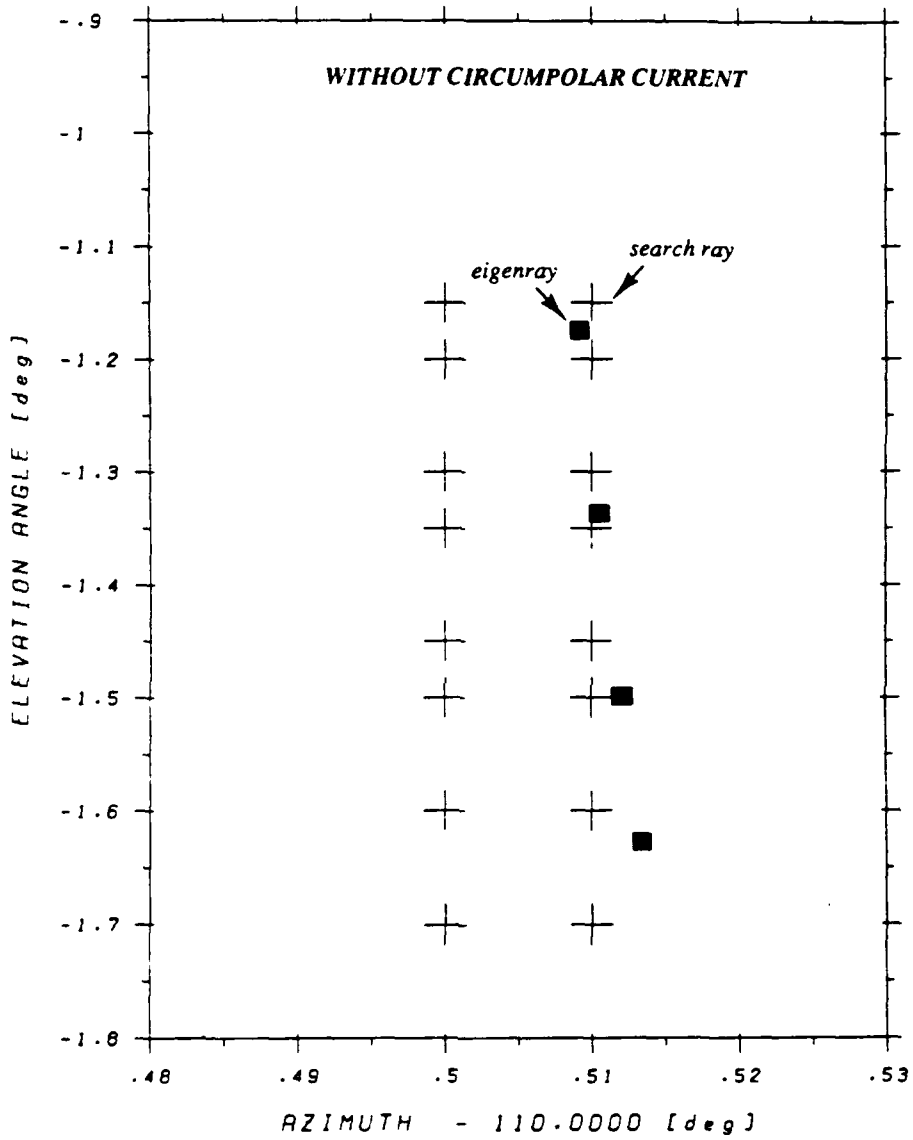


Figure 23. Initial elevations and azimuths of 16 search rays and 4 corresponding eigenrays through a Tasman window without the circumpolar current. (Compare with Fig. 18.)

This required a dual approach: an analytical effort, to absorb and adapt the most valuable part of HARPO, i.e., its mathematics, the Hamiltonian, and the dispersion relations; and a computational effort, to breadboard alternative software using HARPO as a gauge or demonstrator. This is the role that it has played historically.

As to applications such as the interpretation of the Heard Island feasibility and long-term acoustic monitoring experiment, a chasm-like conceptual gap developed relative to what is accepted as state-of-the-art in ray tracing. It can be safely said that most of the ray tracing literature is rooted in the 70's, 60's, and before. In much of this the medium is to be smooth, maybe undulating sinusoidally or meandering with a mesoscale eddy here and there. In addition, the integrators are to be of "high order," in the Taylor expansion sense.

Of course, the real ocean does not look that way. High order integrators are murderous on functions (without loss of generality, integrands) that do not have a rapidly converging Taylor expansion, or do not possess it at all. This we will explain later in some detail because it still seems to be regrettably novel. We owe much to the influential work of J.F. Kaiser of Bell Labs, who labeled, during the Summer Conference in Computer Science at Princeton University in 1966, the "high order" methods as "18th century mathematics, good for planetary orbits, and nearly worthless on noisy data" (see also Kuo and Kaiser, 1966), and to R. W. Hamming (1983), who states "the implications of what the formulas do to noisy (high frequency) data was intuitively understood in hand-calculating days but has not, generally speaking, appeared in modern textbooks." We recall that Hamming developed this theme (at least since 1970), but we could not locate the reference.

Last but not least comes the awareness that there is a contradiction in advocating on one hand ray techniques of wave propagation in

a realistically modeled ocean, and on the other hand applying to that objective inherently nonlinear ray tracing with the maximum possible degrees of freedom, i.e., three. This awareness is really a notion of the late 80's; it points not just to a possibility but also to the likelihood of chaotic behavior in long distance ray paths (Palmer et al., 1988). We did put some effort into analyzing the implications and into seeking ameliorating modeling compromises, such as reducing the freedom of the problem by visualizing sound propagation in the thin global boundary layer in which vertical and horizontal effects may be only weakly coupled. This is not an original idea; it has been practiced recently by Munk et al. (1988), and we will touch upon this too.

After addressing this emerging and important issue of nonlinear instability, we will summarize the work actually completed, in four categories: technical, software, geophysical, and oceanographic.

### *The "Classical" Chaos*

In Section 2, a ray-geometrical explanation of the notion "fully 3-D" was given, but there is also the notion of *classical chaos*. When the integration of 3-D ray equations is executed over large distances through a nonsmooth medium, the ray trajectories may exhibit a *deterministic chaos*. Since this chaos is associated with deterministic systems, it is simply called chaos (Jackson, 1989). The system here is an "IV (initial value) problem," consisting of an ODE (ordinary differential equation) set, subject to initial value conditions.

When these equations are thought to faithfully represent a modeled phenomenon, then the specific chaotic features (more about them later) are attributed to the phenomenon regardless of how the equations are numerically integrated. But poorly conceived integration may by itself add to the instability. For example, the Runge-Kutta "four," which is equivalent to the Simpson formula, is unstable on noisy data.

A fair number of modeling elements must contribute to the attainment of a chaotic threshold. The threshold itself is poorly defined because of nonlinearity. Most of the contributing elements, but not all, are beyond the modeler's control. They are the intrinsic nonlinearity of the problem, the long range to be modeled, and a rich wavenumber spectrum of a realistically described ocean. Two of these elements are somewhat under the modeler's control: the dimensionality of the *phase space* for the ODE system, and the inner structure of the integration algorithm.

Hamming (1983) has shown that the cause for instability of the Simpson formula is its particular form of recursiveness, which has a spectral transfer function that amplifies the (spectral content at) high wavenumbers. He considered this behavior mainly as an error, and did not address its unstable dependence on initial conditions. This latter effect requires consideration of spectral phases, and that was a topic of some interest in mechanical radiation along characteristics of internal waves in the ocean (Rattray et al., 1969). As with underwater acoustics, progress was evolving from a smooth representation of the ocean to one including finer structure. Dworski (1973) showed, in the form of a small theorem, that the internal wave characteristics are systematically steeper in the presence of thermohaline fine structure than they would be without it. This theorem is based on the fact that, during the integration, the Lebesgue measure of vertical intervals of weak static stability must be large compared with the Lebesgue measure of intervals where the stability is high. The theorem holds, of course, regardless of what spectrum the fine structure has, but to determine how much steeper the characteristics were, simulation of fine structure was used.

In this simulation the Simpson (Runge-Kutta four) integration showed large and, more importantly, erratic departures from the smooth case. The following dramatically illustrates the

behavior. Consider a function to be integrated as having  $10^3$  values that alternate between +1 and -1. One expects the integral to be zero, but Simpson returns the value -300 if the initial function value is +1, and the integral becomes +300 according to Simpson if the initial value is -1. It is absolutely warranted to call this unstable and huge error a "dependence on initial values" because the integral will change little if one repeats the thought experiment and changes a few values at the tail of the integration interval to arbitrarily distributed  $\pm 1$ s (even the entire tail to +1 or to -1). However, the trapezoidal integration (Heun's method in ODEs) returns the correct zero value. Fortunately, the stability of low order integration methods is beginning to be recognized in the nonlinear dynamics literature. For example, Jackson (1989) speaks about the desirability of modifying Runge-Kutta when the dynamics involves "fast" and "slow manifolds," and watching that the modification is adequate because "they can 'run away' in some cases." More to the point in chaos computations is the work of Parker and Chua (1989), who simply state that the trapezoidal integration is well suited for stiff problems.

We want to make clear that 3-D ray tracing on realistic data in long range propagation deserves a cost/benefit analysis. This analysis cannot be done unless one has 3-D capability with gridded data. This report is a foundation to that end. An optimization of the benefits/cost ratio seems to point toward a "boundary layer type" treatment in "2-D+" dimensions as a subject of future efforts. A short explanation on potential handicaps of the "fully 3-D" modeling is appropriate now.

Chaotic behavior is directly linked to the degree-of-freedom (DOF) of the ODE system, and not to the Hamiltonian from which the ODE system is derived. However, a better qualitative understanding of the specific type of classical chaos is facilitated by the assurance that the ODE system stems from a Hamiltonian; in brief,

the chaos will be more benign than it could be for an arbitrary nonlinear system of the same dimensionality. This dimensionality is reckoned either by DOF (our 3-D means DOF = 3) together with the statement that the system is autonomous or nonautonomous, or by the dimension of the *phase space*. The phase space of autonomous systems has dimension  $2 \times \text{DOF}$ , while the dimension of a nonautonomous system is  $2 \times (\text{DOF} - 1)$ . Keep in mind that the clear graphical displays are only possible for phase spaces up to dimension two, and that nonlinear systems with phase space of dimension larger than four will almost certainly display chaos for some range of parameters.

The "fully 3-D" treatment requires a phase space of dimension six. In the material discussed in this report no chaos was detected, but we attribute this primarily to the smoothness of the model ocean and of the modeled Antarctic Circumpolar Current, and to the very flat (low elevation angles) rays that were modeled because of site-specific (Heard Island) considerations. To better grasp the ray evolution in a simulated propagation problem of lower dimensionality, but in a peculiarly perturbed ocean, one can look at the work of Palmer et al. (1988). After numerically solving a 2-D Hamiltonian system, they illustrate a partly chaotic behavior for underwater acoustic rays. This system would evolve in a phase space of dimension four, but they ingeniously reduced the evolution to a phase space of dimension two (for ease of display), making the system nonautonomous by aliasing range into time.

The evolution of Hamiltonian trajectories in a phase space of dimension six is very rich, with 3-D structures named after Kolmogorov-Arnold-Moser KAM "surfaces" (3-D subspaces embedded into the 6-D phase space) that separate, but do not isolate, the trajectories (Rasband, 1990). Separation and isolation are distinct technical terms, and the trajectories undergo a so-called "Arnold diffusion" in patterns that are known as "Arnold webs." The

practical consequence from our viewpoint is that eigenpaths cannot be precisely determined.

Chaotic effects on underwater sound rays were the topic of several recent papers, in particular, Palmer et al. (1988), Brown et al. (1990), and Tappert et al. (1990). While chaoticity of rays is not evident in the material presented in this report, we think we understand why it did not occur and why it may occur once a detailed description of eddies, fronts, and other oceanographic structures is added to the model. Such a "detailed" description need be only relatively nonsmooth; that is, these structures may have length scales of  $10^2$  acoustic wavelengths, rather than  $10^4$  wavelengths. The latter is a typical horizontal length scale used in our computations with HARPO.

However, in some other work (Dworski, 1991), we have had fairly extensive experience with evaluating chaotic appearing ray propagation of short pulses riding on a short wavelength carrier. Unusually interesting results, and excellent correspondence to ground truth data, were obtained when the distribution of the refractive index was modeled using highly resolved "noisy" profiles from actual field data to a vertical length scale of only three acoustic wavelengths. There was no smoothing whatever. The discrepancies between hindcast and ground truth were small and could be attributed to lack of sufficient information about the horizontal distribution of the sound speed field. Because the propagation path was under the polar ice cap, this field was laminated, and the horizontal scales of the lamina were long. Looking at this experience in the context of the work of Palmer et al. (1988), one notices a pattern: when they introduce horizontal perturbations to the sound field, the flat rays (near elevation angle zero) do not get chaotic but the steep rays do. In the cited arctic experiment, the perturbation is in the vertical, and the flat rays get chaotic but the steep rays do not.

We summarize now our experience with eigenrays in the presence or absence of chaotic

behavior from both the physical and the mathematical viewpoint of a user who seeks primarily to characterize travel times. The longest underwater propagation paths on earth are those we are dealing with, and they are finite. The evolution time of the corresponding Hamiltonian system is also finite. The wavenumber spectrum of the sound speed disturbances to the waveguide is limited at both ends. The interesting one is the high wavenumber end, since a smooth integrator there may be a primary cause of computational instability. Also, the real ocean spectrum is much broader, with lots of possible out-of-phase "driving" terms for the Hamiltonian equations, than the line spectrum of the perturbations that Palmer et al. (1988) used in their simulation model. Aside from computational instabilities that can be avoided, we believe that the chaotic trajectories represent valid physics for specific representations of the medium. For this very reason, the Fermat principle remains "active," and we think that the travel times are not chaotic on scales of interest to us. This statement, in order not to become a contradiction, implies that clusters of initial conditions map into clusters of ray points with similar travel times at the receiver. If this materializes, then such a cluster-to-cluster mapping becomes a generalized eigenray. Its numerical signature, perfectly amenable to computational identification, is the clustering of travel times. The "ranging in" shooting of rays is then not appropriate; instead, a "shotgun blast" of many rays is applied with the somewhat sophisticated feature that the trajectories "report" to the supervisory algorithm the nearest "fly-by" travel time. The ray tracer must be very fast (we have some positive experience with that) as well as very flexible to integrate "backwards in time."

#### *Technical Results*

- The Hamiltonian equations, (15)–(20), were modified for use on the ellipsoidal earth.
- Differential geometry of the earth's ellipsoid was explored for practical near-antipodal conditions (Figs. 5 and 6). The astroid at the antipode was computationally outlined.
- Oblate spheroidal coordinates were analyzed for applicability, both in full form and in approximation. We conclude that the approximations are very accurate for oceanic ray tracing and moderately accurate for subacoustic ocean/crust ray tracing. The idea of a boundary layer ray tracer and a corresponding coordinate system gained in appeal because of the potential in reducing the phase space dimensionality of the Hamiltonian.
- The decoupling, or weak coupling, of the horizontal and vertical ray equations was construed as an extension of the concept of refracted geodesic, and the adiabatic invariance (Munk et al., 1988).
- Ray equations in cylindrical coordinates were derived (Appendix A), and their relation to the Hamiltonian equations clarified.
- A nonlinear search algorithm, Figs. 18–23, was developed for eigenrays. Its final iterate may use linearization by a 3-D or 2-D Jacobian, Eqs. (25) and (26).
- A formalism to generate smooth range-dependent sound field models based on Munk's canonical profiles was developed. Quasi-Hermite splines link the four parameters of the canonical profiles, not the data. Lookup tables of the spline expansion coefficients permit fast evaluation.

#### *Software Considerations*

- The 3-D smooth Hamiltonian ray tracer was identified as a good demonstration and calibration device but not a working model to support long range propagation experiments. We will write a library-based, 3-D, moderately stiff ray tracer (variable order Runge-Kutta-Fehls marching integrator)

using the ellipsoidal Hamiltonian equations. It will use both the quasi-Hermite splined representation of the ocean and the GFDL (Levitus) gridded data base. Its main purpose will be computational comparison with faster, possibly semianalytical on a cellular basis, ray tracers of "low-pass" wavenumber capability.

- One of our objectives was to modify HARPO for work with a Hamiltonian in spheroidal coordinates. When it became clear that an extensive modification of the HARPO architecture was also needed, an entirely different level of effort was indicated. Because that level could not be sustained with available resources, we reappraised the software architecture for ray propagation in general. The conclusions point away from the idea of integrated models (where the I/O and ray tracing codes are closely coupled). Even though a model is highly modular (HARPO has, including plotting, 81 modules), the information flow between modules may be so diffuse that the effect is strong coupling. This must be avoided.
- Sophisticated concepts of modern software development, e.g., those described in the MIT "weed eater" (Abelson et al., 1985) have now reached the early levels of undergraduate studies. This merely points to the extremely rapid development in computing. Most hardware people understand this, and it is up to us as model developers to follow suit. Models should be subjected to some form of "sunset law"; every five years or so, they ought to be completely disassembled, retaining the mathematics but reconstructing the I/O and the supervisory algorithms to match the data structures and the capabilities of the host computers. If this reconstruction turns out to be hard, then the original model architecture was most likely deficient.
- Specifically, the key emerging concepts are "abstraction barriers," and application of a

"data-directed style." One of the precepts of Abelson et al. (1985) is: "Encapsulation reflects the general system-design principle known as the hiding principle. One can make a system more modular and robust by protecting parts of the system from each other; that is, by providing information access only to those parts of the system that have a 'need to know'." Fortunately, ray modeling lends itself to these partitioning approaches because of its structural simplicity as an initial value problem in ordinary differential equations. This part is expressly suited for configuring it as a generic library, because the interfaces of ODE-IV software are by now nearly standardized. It is the data structures that present a real challenge, and probably no cure-all solutions are in sight—the more reason to insist on an adaptable I/O, and to make it as abstract as possible. We are in the process of doing this.

#### *Geophysical*

- The horizontal refraction of acoustic eigenpaths over distances of 18 Mm can be impressive (Fig. 14). The 500 km deviation of that eigenpath relative to either the unrefracted spherical or ellipsoidal geodesic is primarily due to the thermohaline circumpolar front, with the transmitter located on one side of it and the receiver on the other.
- While the front and the Antarctic Circumpolar Current are the two major zonal structures of the Southern Oceans, the current has a very small effect on the sound propagated across it. Neither the path nor the travel time is affected much. The sound path is displaced by no more than 300 m, as can be seen by comparing Figs. 18 and Fig. 23 for the effect on the launch azimuth, and then realizing from Fig. 20 that a launch azimuth difference of  $0.01^\circ$  produces paths that are less than 350 m apart at the receiver. Figure 24 shows the time delays. The circumpolar current

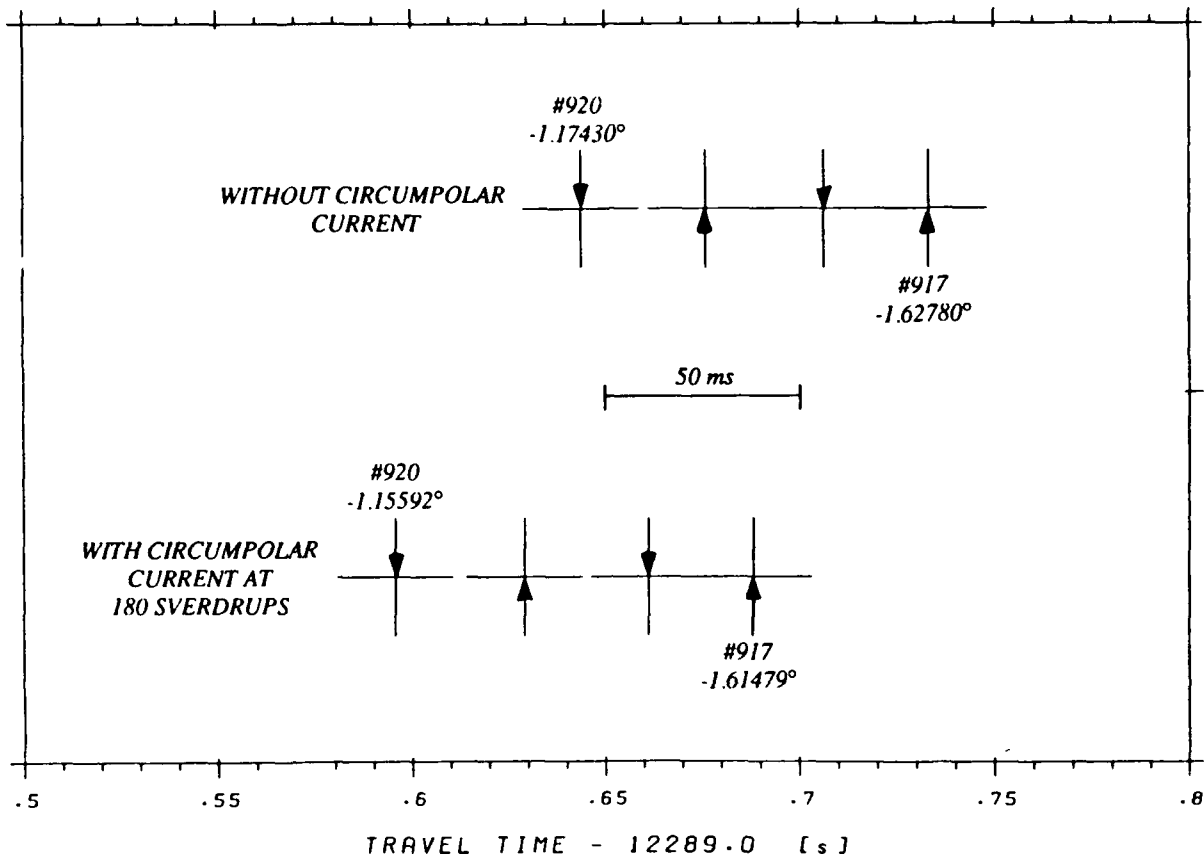


Figure 24. Reduced travel time comparison of eigenrays with and without the circumpolar current. Arrows indicate the direction of arrival at the receiver. Selected arrivals for each case are identified with the corresponding ridge number and the initial elevation angle.

speeds up acoustic paths through the Tasman window (it slows down the Atlantic window paths). But the speed-up in Fig. 24 amounts to a mere 55 ms. Both of these results confirm a "back of the envelope" calculation, for the sound is a fast "swimmer" traversing at 1450 m/s the "stream" that flows at 0.3 m/s. It is not advected much, because it takes no more than a few hundred seconds to get outside the influence of the stream.

- An antipodal geometry exists for underwater paths on earth, and it is most likely realizable only between the southern Indian Ocean and the North Atlantic. The interesting conjecture is that a horizontal caustic may develop at points between Bermuda and the U.S. mainland—from paths that originate at points between Perth and Antarctica—and vice versa (Fig. 6). The net azimuthal width of the acoustic window between Africa and Brazil is about  $20^\circ$ , and a reasonable part of the emitted acoustic energy may refocus along that caustic.

#### *Oceanographic*

- The vertical span of launch elevation angles for rays transmitted from Heard Island would be small if one could not count on paths that experience multiple interactions with the sea surface (about 100 surface reflections for the flattest rays of about  $\pm 1.7^\circ$ ).
- We had too little information about the actual sound channel at high southern latitudes. Because there is a consensus that the channel axis is shallow, we conjecture that the channel itself is weak. There is strong wind forcing at these latitudes most of the time, and particularly fierce forcing during the Austral winter. The Heard Island feasibility experiment will be staged in the favorable time of the year, but we are preparing to look early at as much time-dependent data as we can get hold of. The flexible modeling capability of looking at gridded or even randomly spaced

data becomes very important. Fortunately, the initial value problem acts to our advantage. The oceanic stretch over which wind forcing may control the presence or absence of the shallow channel is not extraordinarily long.

## References

- Abelson, H., G.J. Sussman, and J. Sussman, 1985: *Structure and Interpretation of Computer Programs*, The MIT Press, Cambridge, MA, 542 pp.
- Aki, K., and P.G. Richards, 1980: *Quantitative Seismology, Theory and Methods*, W.H. Freeman, San Francisco, vol. I, pp., 1-558, vol. II, pp. 559-932.
- Akima, H., 1970: "A New Method of Interpolation and Smooth Curve Fitting Based on Local Procedures," *J. Association for Computing Machinery*, 17, 589-602.
- Akima, H., 1974: "Algorithm 474. Bivariate Interpolation and Smooth Surface Fitting Based on Local Procedures," *Comm. Association for Computing Machinery*, 17, 26-31.
- Arfken, G. B., 1970: *Mathematical Methods for Physicists*, Academic Press, New York, 2nd ed., 815 pp.
- Baier, R. V., 1972: "Acoustic Radiation Impedance of Caps and Rings on Oblate Spheroidal Baffles" *J. Acoust. Soc. Am.*, 51, 1705-1716.
- Baker, D. J., R. B. Wearn, Jr., and J. G. Dworski, 1980: "Wind Computed from Australian Twice-Daily Sea Surface Pressure Maps, a Comparison with SEASAT Altimeter Wind Speed, July 7 - October 10, 1978," unpublished manuscript, Coll. of Ocean and Fishery Sci., U. of Washington, Seattle, WA 98105.
- Baxter, L., II, and M. H. Orr, 1982: Fluctuations in Sound Transmission through Internal Waves Associated with the Thermocline: A Computer Model for Acoustic Transmission Through Sound Velocity Fields Calculated from Thermistor Chain, CTD, XBT, and Acoustic Backscattering," *J. Acoust. Soc. Am.*, 71, 61-66.
- Bold, G. E. J., and T. G. Birdsall, 1986: "A Top-Down Philosophy for Accurate Numerical Ray Tracing," *J. Acoust. Soc. Am.*, 80, 656-660.
- Bomford, G., 1980: *Geodesy*, Clarendon Press, Oxford, U.K., 4th ed., 885 pp.
- Booker, H. G., and W. Walkinshaw, 1946: "The Mode Theory of Tropospheric Refraction and its Relation to Wave-Guides and Diffraction," in *Meteorological Factors in Radio Wave Propagation*, pp. 80-127, The Physical Society, London, UK.
- Brekhovskikh, L. M., 1960: *Waves in Layered Media*, Academic Press, New York, NY, 1st ed. [transl. from Russian].
- Brekhovskikh, L. M., 1980: *Waves in Layered Media*, Academic Press, New York, NY, 2nd ed. [transl. from Russian].
- Brown, M. G., K. B. Smith, and F. D. Tappert, 1990: "Sound Ray Chaos Induced by Oceanic Internal Waves and Mesoscale Structure," *J. Acoust. Soc. Am.*, 87, Suppl. 1, S55.
- Budden, K. G., 1961: *The Wave-Guide Mode Theory of Wave Propagation*, Logos Press/Prentice-Hall, London, U.K., and Englewood Cliffs, NJ, 318 pp.
- Budden, K. G., 1988: *The Propagation of Radio Waves*, Cambridge U. Press, Cambridge, U.K., 669 pp.
- Chelton, D. B., K. J. Hussey, and M. E. Parke, 1981: "Global Satellite Measurements of Water Vapor, Wind Speed and Wave Height," *Nature*, 294, 529-532.
- Conway, A. W., and J. L. Synge, Eds., 1931: *The Mathematical Papers of Sir W. R.*

- Hamilton*, Cambridge U. Press, Cambridge, U.K.
- Craig, H., W.S. Broecker, and D. Spencer, 1981: *GEOSECS Pacific Expedition*, U.S. Govmt. Printing Office, Washington, DC 20402.
- De Boor, C., 1978: "A Practical Guide to Splines," *Applied Mathematical Sciences*, 27, Springer-Verlag, New York, 392 pp.
- Dongarra, J.J., J.R. Bunch, C.B. Moler, and G.W. Stewart, 1979: *LINPACK User's Guide*, SIAM Publications, Philadelphia, PA.
- Dworski, J.G., 1973: "A Variable Aperture Recursive Filter for Estimation of the Brunt-Vaisala Frequency," in *Proceedings (supplement), Second S-T-D Conference January 24-26, 1973*, Plessey Environmental Systems, San Diego, Cal.
- Dworski, J.G., 1991: "FASTRAY Raytracer Resolves Spatial Fluctuations of High-Frequency Sound Propagation in the Arctic Ocean," APL-UW TM 2-91, Applied Physics Laboratory, University of Washington, Seattle, WA 98105 (in preparation).
- Eliseevnin, V. A., 1965: "Analysis of Rays Propagating in an Inhomogeneous Medium," *Soviet Physics-Acoustics*, 10, 242-245 [transl. from *Akust. Zh.* 10, 284-288 (1964)].
- Gibbons, A., 1990: "What's the Sound of One Ocean Warming?," *Science*, 248, 33-34.
- Gordon, A.L., E. J. Molinelli, and T. N. Baker, 1982: *Southern Ocean Atlas*, Columbia University Press, New York.
- Hamming, R. W., 1983: *Digital Filters*, Englewood Cliffs, NJ, 2nd ed., 257 pp.
- Haselgrove, J., 1954: "Ray Theory and a New Method for Ray Tracing," in *The Physics of the Ionosphere*, pp. 355-364, The Physical Society, London, U.K.
- Helmert, F.R., 1880: *Die Mathematischen und Physikalischen Theorien der Hoeheren Geodaesie, I. Teil*, Leipzig [Mathematical and Physical Theories of Higher Geodesy, Part I.]
- Herzberger, M., 1937: "Hamilton's Characteristic Function and Bruns' Eiconal," *J. Optical Soc. Am.*, 27, 133-137.
- IMSL, 1979: "IQHSCU: Quasi-Hermite Data Smoother Reference Manual," Edition 7, International Mathematical and Statistical Libraries, Inc., Houston, TX 77036.
- Jackson, E. A., 1989: *Perspectives of Nonlinear Dynamics*, Cambridge U. Press, Cambridge, U.K., vol. 1, 496 pp.
- Jones, R.M., J.P. Riley, and T.M. Georges, 1986: "HARPO, a Versatile Three-Dimensional Hamiltonian Ray-Tracing Program for Acoustic Waves in an Ocean with Irregular Bottom," NOAA Wave Propagation Laboratory, Boulder, CO, Nat. Tech. Information Service, Springfield, VA 22161, 455 pp.
- Jordan, W., O. Eggert, and M. Kneissl, Eds., 1956-1972: *Handbuch der Vermessungskunde*, J.B. Metzler Ver., Stuttgart, [Handbook of Geodesy] 10th ed., 6 vols.
- Kamenkovich, V.M., and A.S. Monin, 1978: *Fizika Okeana, Tom 1: Gidrofizika Okeana*, Nauka, Moskow, USSR [Physics of the Ocean, Vol 1., 455 pp.].
- Keller, J.B., 1954: "Geometrical Acoustics, I: The Theory of Weak Shock Waves," *J. Appl. Phys.*, 25, 938-947.
- Kuo, F.F., and J.F. Kaiser, Eds, 1966: *System Analysis by Digital Computer*, Wiley, New York, 438 pp.

- Lee, D., 1990: "Numerical Ocean Acoustic Propagation in Three Dimensions," in *Ocean Acoustics Program Summary for FY-89*, p. 23, ONR Code 11250A (Ocean Sciences Directorate) Arlington, VA 22217-5000.
- Lighthill, J., 1979: *Waves in Fluids*, Cambridge U. Press, Cambridge, U.K., 504 pp.
- Lynch, J.F., 1990: "HARPO-MOD1, Improvements to 3-D Raytracing Codes," in *Ocean Acoustics Program Summary for FY-89* (development status report), p. 25, ONR Code 11250A (Ocean Sciences Directorate), Arlington, VA 22217-5000.
- Madelung, E., 1957: *Die Mathematischen Hilfsmittel des Physikers*, Springer, Berlin, [Mathematical Tools for the Physicist] 6th ed., 535 pp.
- Mercer, J.A., W.J. Felton, and J.R. Booker, 1985: "Three-Dimensional Eigenrays Through Ocean Mesoscale Structure," *J. Acoust. Soc. Am.*, 78, 157-163.
- Morse, P.M., and H. Feshbach, 1953: *Methods of Theoretical Physics*, McGraw-Hill, New York, 623 pp.
- Munk, W.H., 1974: "Sound Channel in an Exponentially Stratified Ocean, with Application to SOFAR," *J. Acoust. Soc. Am.*, 55, 220-226.
- Munk, W.H., and A.M.G. Forbes, 1989: "Global Ocean Warming: An Acoustic Measure?," *J. Phys. Oceanogr.*, 19, 1765-1778.
- Munk, W.H., W.C. O'Reilly and J.L. Reid, 1988: "Australia-Bermuda Sound Transmission Experiment (1960) Re-visited," *J. Phys. Oceanogr.*, 18, 1876-1898.
- Ostashev, V.E., 1985: "Theory of Sound Propagation in an Inhomogeneous Moving Medium (Review)," *Izvestiya, Atmospheric and Oceanic Physics*, 21, 274-285.
- Palmer, D.R., M.G. Brown, F.D. Tappert, and H.F. Bezdek, 1988: "Classical Chaos in Nonseparable Wave Propagation Problems," *Geophys. Res. Lett.*, 15, 569-572.
- Parker, T.S., and L.O. Chua, 1989: *Practical Numerical Algorithms for Chaotic Systems*, Springer-Verlag, New York, 348 pp.
- Pekeris, C.L., 1946: "Accuracy of the Earth-Flattening Approximations in the Theory of Microwave Propagation," *Phys. Rev.*, 70, 518-522.
- Pierce, A.D., 1981: *Acoustics*, McGraw-Hill, New York, 642 pp.
- Podeszwa, E.M., 1976: "Sound Speed Profiles for the North Pacific Ocean," NUSC Technical Document 5271, Naval Underwater Systems Center, New London, CT 06320.
- Rasband, S.N., 1990: *Chaotic Dynamics of Nonlinear Systems*, Wiley-Interscience, New York, 230 pp.
- Rattray, M., Jr., J.G. Dworski, and P.E. Kercala, 1969: "Generation of Long Internal Waves at the Continental Slope," *Deep-Sea Res.*, 16, 179-195.
- Shockley, R.C., J. Northrop, P.G. Hansen, and C. Hartdegen, 1982: "SOFAR Propagation Paths from Australia to Bermuda: Comparison of Signal Speed Algorithms and Experiments," *J. Acoust. Soc. Am.*, 71, 51-60.
- Synge, J.L., 1937: "Hamilton's Method in Geometrical Optics," *J. Optical Soc. Am.*, 27, 75-82.
- Tappert, F.D., G.J. Goni, and M.G. Brown, 1990: "A Search for Wave Chaos in a Simple Range-Dependent Underwater Acoustic Waveguide," *J. Acoust. Soc. Am.*, 87, Suppl. 1, S55.

- Vinti, J. P., 1959: "New Approach in the Theory of Satellite Orbits," *Phys. Rev. Lett.*, 3, 8.
- Weinberg, H., 1981: "Generic Sonar Model," NUSC Technical Document 5971C, Naval Underwater Systems Center, New London, CT 06320.
- Whitham, G. B., 1961: "Group Velocity and Energy Propagation for Three-Dimensional Waves," *Commun. Pure Appl. Math.*, 14, 675-691.
- Wyrki, K., 1988: *Oceanographic Atlas of the International Indian Ocean Expedition*, Amerind Co., New Delhi, India, Sect. 7, pp. 431,432.
- Zakatov, P. S., 1962: A Course in Higher Geodesy; Spheroidal Geodesy and Fundamentals of Gravimetry and Practical Astronomy, U.S. Dept. Commerce, Off. Tech. Serv., Washington, DC, 2nd ed., 457 pp. Kamenkovich, V.M., and A.S. Monin, 1978: *Fizika Okeana, Tom 1: Gidrofizika Okeana*, Nauka, Moskow, USSR [Physics of the Ocean, Vol 1., 455 pp.].

## APPENDIX A

## Reduced Dimensionality Ray Tracers and the Hamiltonian

*Vertically Refracted Paths on the Spheroid*

To gain flexibility in using environmental data, such as those given along a transect, numerical codes can be based on special versions of the ray tracing equations. In the Hamiltonian vs eikonal debate (Synge, 1937; Herzberger, 1937), one of the arguments concerned the number of variables (and equations) needed to describe ray propagation in geometrical optics: six (Hamiltonian) or only four-to-six (Bruns' eikonal). From the modern computational viewpoint it may matter less how many equations are integrated than how "convenient for the user" are the variables in the equations. For example, the local elevation angle of the ray path is a dependent variable that the user may want computed directly, because integration step adjustment criteria can be coupled to its evolution (e.g., fine stepping near turning points). The elevation angle is directly computed in Eqs. (A4) and (A12) here.

A fringe benefit of having specialized versions of ray equations available is that certain propagation features may become particularly clear. An illustration that shows the effective axis of the sound channel to be systematically offset relative to the geometrical axis will be given as a by-product of the development below.

Regarding data utilization, a relevant example of ray propagation modeled through sound velocity fields calculated from thermistor chain, CTD, XBT, and acoustic backscattering is given by Baxter and Orr (1982). They integrate range dependent ray equations in a Cartesian frame, focusing on ranges where the earth curvature is not important. These equations were derived from the eikonal by Eliseevnin (1965), where he numerically treated a strongly range dependent problem. Also, he

gave the 3-D Cartesian version of the equations without derivation.

Recognizing the future potential of interfacing our long range calculations with the type of field data Baxter and Orr (1982) worked with, we include the earth's curvature in these equations. While Eliseevnin's equations are correct, the derivation was not entirely straightforward (at least in the translation). Thus we compactly re-derive these equations from the eikonal, and then proceed to cast them into the desired curved coordinate frame. If we assume that the vertical and horizontal equations are separable, and that the horizontal equations are the refracted geodesics of Munk et al., the vertical equations need be defined in only a cylindrical two-space.

*Range-Dependent Cartesian 2-D Equations*

Let  $n = c_0/c$  be the refractive index, with  $c_0$  a constant and  $c$  the variable sound speed. Using the same notation as in the Hamiltonian equations, the relation between travel time  $t$  and the path length  $s$  is given by

$$\frac{d}{ds} = \frac{1}{c} \frac{d}{dt}$$

The eikonal can be written with  $w$  as the phase variable so that its intrinsic geometry of direction cosines are highlighted:

$$\left[ \frac{\partial w / \partial x}{n} \right]^2 + \left[ \frac{\partial w / \partial y}{n} \right]^2 = 1.$$

The two terms on the left are direction cosines of the ray wrt (with respect to) the  $x$  and the  $y$  axis. The  $x$  axis is the horizontal range axis, and  $y$  is along the vertical axis. If  $\alpha$  denotes the ray elevation angle wrt the  $x$  axis, the first term is  $\cos\alpha$  and the second term is  $\sin\alpha$ . Multiply these trigonometric functions by  $n$  and then

cross-differentiate, the first wrt  $y$  and the second wrt  $x$ . Since the two mixed second partials of  $w$  must be equal, set

$$\partial(n \cos\alpha)/\partial y - \partial(n \sin\alpha)/\partial x = 0. \quad (A1)$$

The ray path element is  $\vec{ds} = (dx, dy)$ , and the first two differential equations for the ray become simply

$$\begin{aligned} dx/ds &= \cos\alpha \\ dy/ds &= \sin\alpha. \end{aligned} \quad (A2)$$

From the definition of the refractive index as  $n = c_0/c$ , one obtains by logarithmic differentiation the generic form

$$\frac{\partial n}{\partial(\cdot)} = -\frac{n}{c} \frac{\partial c}{\partial(\cdot)}. \quad (A3)$$

By using the chain rule on (A1) one can segregate to the left the terms that do not feature  $\partial n/\partial(\cdot)$ , and to the right those that do. Then replace the trigonometric functions on the left by substituting (A2), but leave the trigonometric functions on the right alone. The intermediate result is

$$n \frac{\partial \alpha}{\partial x} \frac{dx}{ds} + n \frac{\partial \alpha}{\partial y} \frac{dy}{ds} = \frac{\partial n}{\partial y} \cos\alpha - \frac{\partial n}{\partial x} \sin\alpha.$$

Use (A3) on the right-hand side of the above, and notice that each term on both sides includes  $n$  as a factor. Since  $n$  is never zero, cancel  $n$  everywhere. Note that the left side is the total derivative of  $\alpha$  wrt the path length  $s$ , so that the third equation of the ray trajectory in a range dependent medium is

$$d\alpha/ds = \frac{1}{c} \left[ \frac{\partial c}{\partial x} \sin\alpha - \frac{\partial c}{\partial y} \cos\alpha \right]. \quad (A4)$$

#### Range-Dependent Cylindrical 2-D Equations

Equations (A2) and (A4) are to be cast into a cylindrical coordinate frame to account for the earth's (spherical) curvature. Thereupon, they can easily be adapted to the spheroidal curvature.

Let the sound speed gradient vector be  $\nabla c$ , the unit vector tangent to the ray path be  $\vec{s}$ , and the unit vector perpendicular to the propagation surface be  $\vec{k}$ . In subsequent matrix operations, vectors are considered as one-column matrices even when they are written in transposed (horizontal) form. Two of the vectors are

$$\nabla c = \begin{bmatrix} \partial c/\partial x \\ \partial c/\partial y \end{bmatrix},$$

and

$$\vec{s} = \begin{bmatrix} \cos\alpha \\ \sin\alpha \end{bmatrix} = \begin{bmatrix} dx/ds \\ dy/ds \end{bmatrix}. \quad (A5)$$

Equation (A4) can now be written as a triple scalar product

$$d\alpha/ds = \frac{1}{c} \left[ \vec{k} \cdot (\nabla c \times \vec{s}) \right]. \quad (A6)$$

The relation between the Cartesian and the cylindrical coordinate system is shown in Fig. A1. The ray point vector  $\vec{r}$  is defined by its magnitude  $r$  and the angle  $\beta$  in the cylindrical system, so

$$\vec{r} = \begin{bmatrix} x \\ y \end{bmatrix} = \begin{bmatrix} r \sin\beta \\ r \cos\beta \end{bmatrix}.$$

The unit vectors of the coordinate axes transform by rotation:

$$\begin{bmatrix} \vec{i} \\ \vec{j} \end{bmatrix} = \mathbf{A} \begin{bmatrix} \vec{e}_\beta \\ \vec{e}_r \end{bmatrix},$$

where  $\mathbf{A}$  is the orthonormal rotation matrix

$$\mathbf{A} = \begin{bmatrix} \cos\beta & \sin\beta \\ -\sin\beta & \cos\beta \end{bmatrix},$$

such that its transpose is also its inverse,

$$\mathbf{A}^T = \mathbf{A}^{-1}.$$

Note from Fig. A1 that the ray elevation angle in the (global) cylindrical system is no longer  $\alpha$  but  $\eta$ :

$$\eta = \alpha + \beta. \quad (A7)$$

The gradient vector of the sound speed in the two systems is

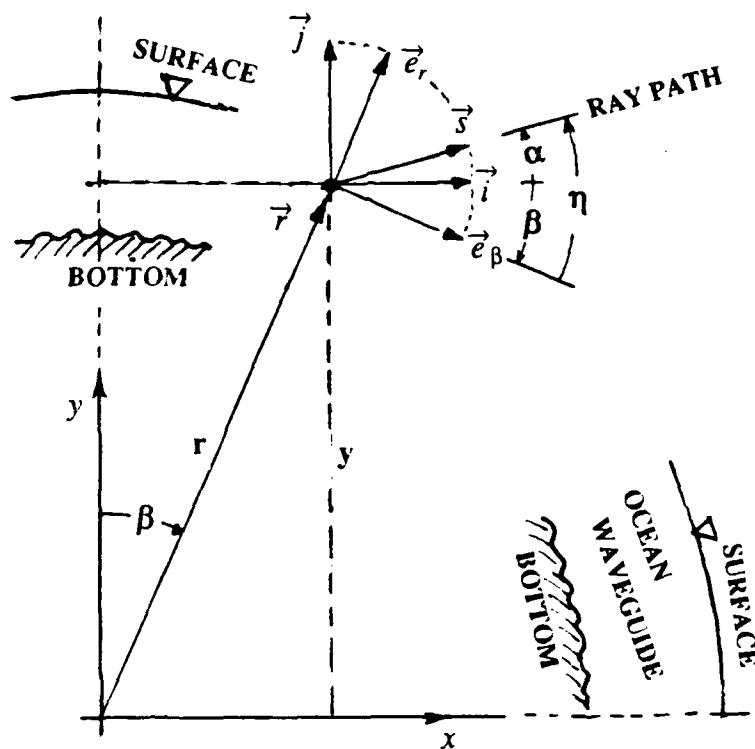


Figure A1. Cartesian and cylindrical coordinate ray parameters.

$$\nabla c = (\partial c/\partial x, \partial c/\partial y) \triangleq \left( \frac{1}{r} \partial c/\partial \beta, \partial c/\partial r \right),$$

and its components transform in the same way as do the unit vectors:

$$\begin{bmatrix} \partial c/\partial x \\ \partial c/\partial y \end{bmatrix} = A \begin{bmatrix} \frac{1}{r} \partial c/\partial \beta \\ \partial c/\partial r \end{bmatrix}. \quad (\text{A8})$$

Take the  $d/ds$  derivative of the components of  $\vec{r}$  to obtain

$$\begin{bmatrix} dx/ds \\ dy/ds \end{bmatrix} = A \begin{bmatrix} r d\beta/ds \\ dr/ds \end{bmatrix}. \quad (\text{A9})$$

Invert (A9) and expand  $A^{-1}$ . Use the addition formulas for the sine and cosine of  $(\alpha + \beta)$  and substitute (A7) to obtain the first two equations:

$$d\beta/ds = \frac{1}{r} \cos \eta, \quad (\text{A10})$$

and

$$dr/ds = \sin \eta. \quad (\text{A11})$$

Consider (A6) again. Substitute (A7) on the left, and work on the right-hand side by substituting (A8) for  $\nabla c$ , and the trigonometric form of (A5) for  $\vec{r}$ . Use again the addition formulae for the sine and cosine of  $(\alpha + \beta)$  and substitute (A7) to obtain the third equation, after transposing  $d\beta/ds$  from the left to the right side:

$$\begin{aligned} d\eta/ds &= \frac{1}{r} \cos \eta \\ &+ \frac{1}{c} (\sin \eta \frac{1}{r} \partial c/\partial \beta - \cos \eta \partial c/\partial r). \quad (\text{A12}) \end{aligned}$$

Equations (A10) through (A12) completely describe ray trajectories for which the horizontal path is independently specified. An interesting special case exists when one demands that  $\eta \equiv 0$  all along the path on the curved earth. Equation (A12) then is

$$0 = \frac{1}{r} - \frac{1}{c} \partial c/\partial r,$$

or, alternatively, this ray can materialize only at such  $r$  where

$$\frac{\partial c}{\partial r} = \frac{c}{r}.$$

This means that a ray launched with  $\eta = 0$  elevation at the geometrical axis of the sound channel, where  $\partial c/\partial r = 0$  by definition, cannot maintain  $\eta \equiv 0$ . It will oscillate about a lesser depth (larger  $r$ ) than the channel axis depth, because  $c/r$  is inherently positive, and  $\partial c/\partial r$  is positive above the axis (and negative below).

We first noticed this behavior numerically from HARPO's runs, but could not immediately say that it represented a correct outcome. After concluding that it does, we were satisfied with an approximate analysis that produces the above quantification. The Hamiltonian equations produce the correct result, but (A12) is more amenable to simple limiting analyses.

This appendix has emphasized, in addition to geodesic issues, the communality of various formulations of the ray equations in geometrical acoustics. It ends with an illustration of how this communality can be exploited. The Hamiltonian equations (15) through (20), together with the various dispersion relations defining  $H$ , are a rich source for the extraction of new relations, or validation of existing ones. An instructive and simple example is the derivation of (A11) from (15).

Let  $H$  be the Hamiltonian for the dispersion relation defined as acoustic waves, no current, no losses. Then, from Eqs. (6.21), (6.29), and (6.30) in Jones et al. (1986) one gets

$$\begin{aligned} \kappa^2 &= \omega^2/c^2, \\ \partial H/\omega &= 2\omega, \\ \partial H/\partial \kappa_r &= -2c^2 \kappa_r. \end{aligned}$$

Use (15) in conjunction with the definitions for  $F$  and  $d/ds$  that precede it. Then

$$\frac{dr}{ds} \equiv \frac{c_0}{c} \frac{dr}{dp} = \frac{c}{\omega} \kappa_r = \frac{\kappa_r}{\kappa} \triangleq \sin \eta.$$

Though exceedingly simple (Eq. (A1) is self-evident from Fig. 7), this example is still instructive. It shows the Hamiltonian machinery in action: some variables ( $\omega$  and  $c$ )

that do not affect the answer are nonetheless carried along in the Hamiltonian function. There is the necessary cancellation of factors to attain the correct result, but in an application this cancellation is numerical instead of being analytical before the run.

Hence, in general, there are a number of operations that can be eliminated by reformulating the ray equations. The following pattern is associated with all ray equations, regardless of what approximation to the wave equation they involve:

- The "position evolution" equations (e.g., (15) through (17), (A2), (A10), and (A11)) are always simple.
- All the physics and all the complexity are in the "direction evolution" equations (e.g., (18) through (20), (A4), and (A12)).

## APPENDIX B

## Effective Axis of Sound Channel

*Newton's Apple of the Second Kind*

Recall Newton's second apple? Not the one that fell on his head, but the one he imagined tossing on a tangent to the earth with velocity  $V = [rg(r)]^{1/2}$ . It kept smoothly falling and falling because its trajectory exactly matched the earth's curvature. The situation with an acoustic "axial" ray in the oceanic sound channel is somewhat similar, except it does not involve gravity.

This ray has to be launched tangentially to the channel axis, and the curvature radius of its trajectory must equal the along-path curvature radius of the channel. For a range independent channel, the launch must be parallel to the sea surface, and the trajectory curvature radius must equal the geocentric radius to the ray point. Moreover, the trajectory must be concave toward the earth's center.

We did not say whence to launch the "axial" ray. From the axis of the sound channel? Not really, because there the local vertical curvature radius of the trajectory is, by definition, infinite.

If the ray is launched with elevation angle zero from a point below (i.e., deeper than) the geometrical axis of the sound channel, one can match the desired magnitude of the curvature radius, but the sign will be wrong; the trajectory will be convex toward the earth's center. Thus, only points above the geometrical axis qualify as potential source points for the "effective" axial ray in a sound channel. By "effective" axial ray we mean a ray that does not oscillate at all, or, if the sound channel is range dependent, oscillates least. Then, that appropriate depth can be termed the effective axis depth of the sound channel, and it will always be smaller than the depth of the sound speed minimum.

Why bother? In our case, it was to test the integrity of the 3-D ray tracing codes. But it is useful to know, more generally, that in sound channels in which the minimum velocity is "smeared" over a wide depth interval the effective channel axis is at the upper (shallow) end of that interval.

*Numerical Experiment*

The diagnostic potential offered by a sharp test of an "axial" ray became evident during our changes in the HARPO code to introduce the modified ellipsoidal Hamiltonian. Far from anticipating the qualitative behavior of the axial ray as explained above, we were worried that the obvious oscillation of the nominally axial ray implied some deficiency in specifying the permissible integration error (i.e., we thought that the oscillation would disappear if the error criterion were made more stringent).

To explore this issue, the following test configuration was run with the spherical version of HARP66 (the FORTRAN 66 version of HARPO). The range independent sound speed profile was a canonical profile, Eq. (21). ( $c_0 = 1500$  m/s, nominally centered on  $z = 1000$  m, but relocated to the sea surface,  $z = 0$ ; thus it was located partly in the "air" (negative depths), with a perturbation parameter  $\epsilon = 0.005$  and a "scale height"  $H_c = 1$  km.) The ray was shot at zero elevation angle from a transmitter point chosen realistically in the Indian Ocean (Perth or Heard Island), unrealistically at the sea surface (the geometrical axis of this "channel"), and at an initial azimuth of interest for subsequent simulation of the actual propagation. Such a run exercised the whole HARP66 code, using its complex linkages.

The results turned out to be independent of the specified computational accuracy levels, but they were weakly dependent on the launch azimuth (in a way that will be explained). The finding of a fortuitously "clean" run is illustrated in Fig. B1, in which the described ray oscillates about a position 7.8 m above the nominal axis  $z = 0$  for a few hundreds of kilometers and then stabilizes to that constant height for the rest of nearly 20,000 km. Other runs (other initial azimuths) would make the ray oscillate forever with small amplitudes about the mean position of about 7.8 m.

To summarize,

*The effective sound channel axis is always at a lesser depth than the depth of the sound speed minimum (the nominal sound channel axis). The effective axis is exactly at that point "q" above the nominal axis at which*

$$\frac{1}{c_q} \frac{dc}{dz} \Big|_q = \frac{1}{a_q}, \quad (\text{B1})$$

where  $c$  is the sound speed and  $a_q$  is the geocentric radius to  $q$ .

Keep in mind that the transmit depth was at the geometrical channel axis (minimum sound speed). The explanation for the 7.8 m displacement was sought only after it became obvious that the resulting trajectories were not an artifact of the code (spherical Hamiltonian) or of the run configuration. The exceptionally clean result in Fig. B1 seems to come about because the ray path starts to satisfy the conditions of Eq. (B1) more and more, and the oscillation appears to be damped even though there is no explicit damping mechanism. An intriguing question remains: not only is there no apparent damping mechanism, but there is no "restoring force" to the apparent oscillator in Fig. B1a, because the oscillation never crosses the nominal axis  $z = 0$ , and consequently  $dc/dz$  never changes sign. The upper turning points have an explanation based on refraction: the path reached a higher sound speed region. This is not true for the lower turning points; the

sound speed keeps decreasing before and at the lower turning point. Why the turning of the path under these circumstances?

A qualitative explanation lies in the inherent nonlinearity: preceding a lower turning point, the ray path has a depressed elevation angle and the path tends toward  $z = 0$ , but its curvature radius grows rapidly. The ray path radius becomes much larger than the curvature radius of the channel axis, and this axis literally "sinks" in front of the ray point. Consequently, the ray path "turns" and gets to the "up-swing" again.

Details of this behavior seem to depend on small changes in initial conditions, but on the spheroidal earth and in a slowly varying range dependent sound channel, the least oscillation of a ray path can be expected when the ray is launched from a point above the nominal sound channel axis with an elevation angle that is parallel to that axis. Equation (B1), with a minor adjustment to the meaning of  $a_q$ , can be used to estimate the best height above the axis for placement of the transmit point.

Thus, one infers that the results displayed in Fig. B1 are a correct interpretation (by the HARP66 code) of one of the effects of the Earth's curvature on ray propagation. This is discussed by Brekhovskikh (1960) in his classic book on waves in random media. He points out that the original work on this problem was done by Pekeris (1946), by the method of successive approximation.

However, radio waves are not usually visualized in a parabolic channel, and the exact position of the channel axis is not discussed by Brekhovskikh even though he presents an extensive section on the underwater sound channel.

On the other hand, underwater sound propagation is often best listened to at or near the channel axis, so we thought the channel axis would be worth explaining analytically, in addition to offering the plausibility arguments.

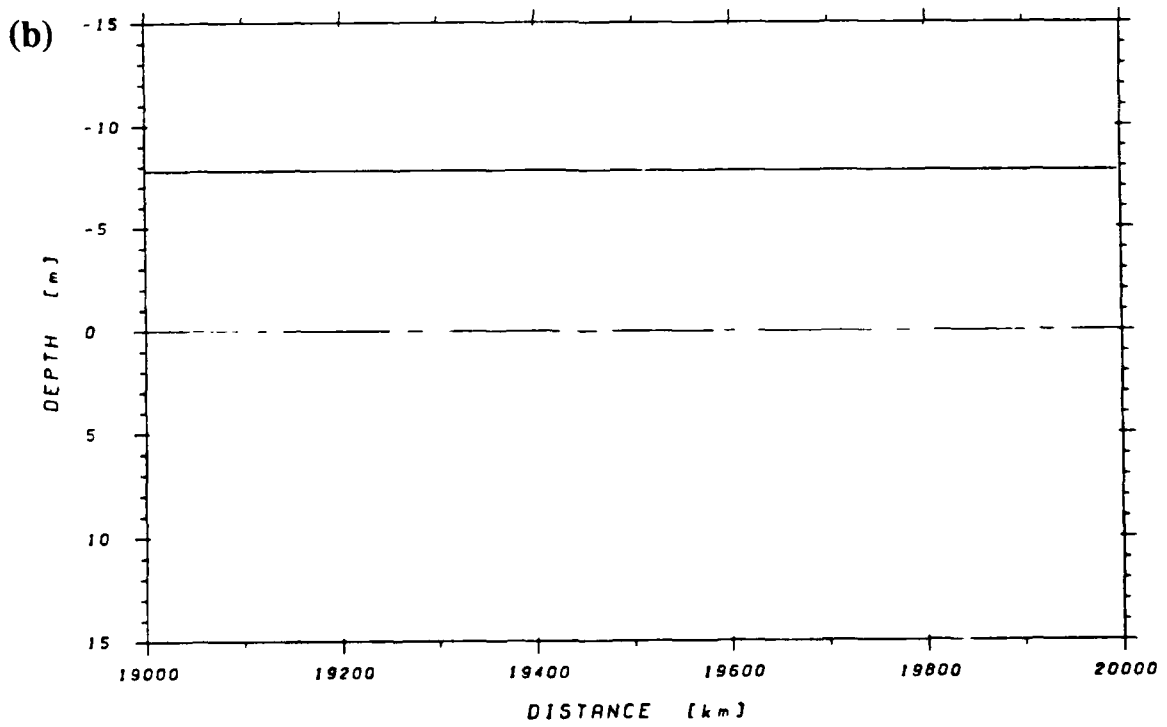
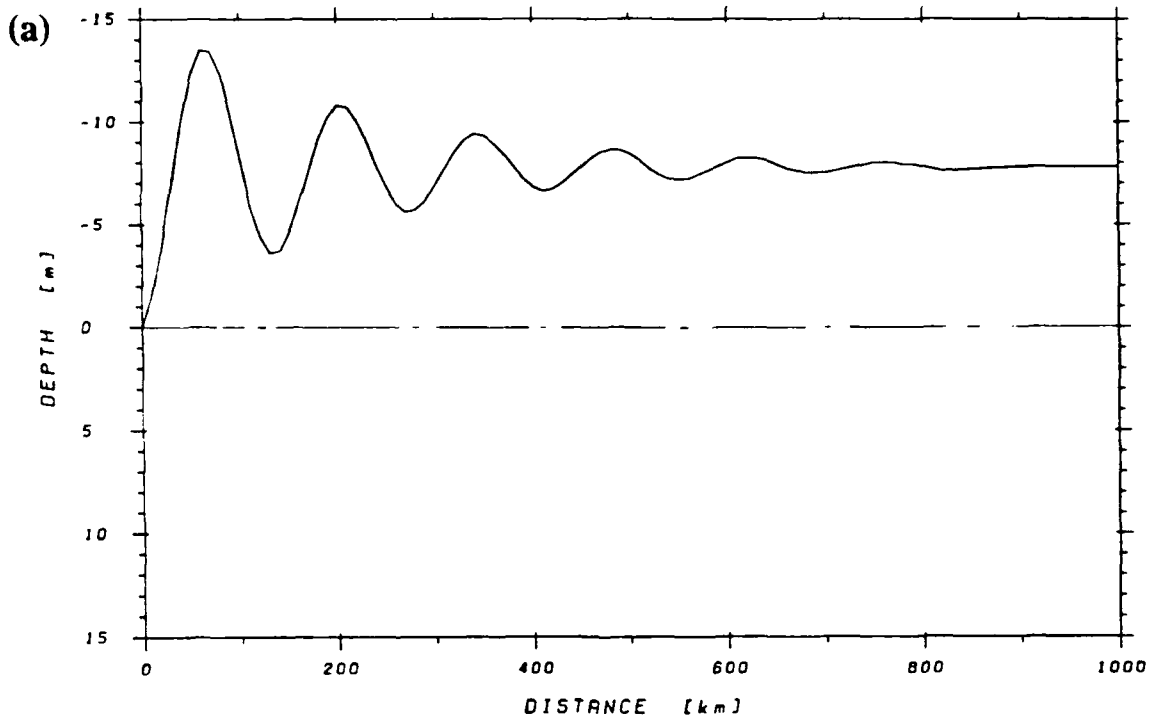


Figure B1. Example of ray trajectory during the first 1000 km (a) and near 20,000 km (b).

*Using approximations to the full wave equation*

Brekhovskikh (1960), following Pekeris (1946), summarizes the analysis of the two scalar functions that satisfy the wave equation, introduces spherical coordinates, and looks for a "modified" refractive index that would approximate the same results in a Cartesian framework.

This idea used to be common in the radio-wave propagation literature, and it conjures an observer at a virtual position who does not know that the earth is curved, but observes that radio waves emanating at zero elevation from a distant transmitter reach his station considerably above the height they were sent from. The ionosphere has a uniform refractive index (the isovelocity acoustic analogue) in this conceptualization, but the naive observer concludes that the refractive index is nonuniform and that it has caused the waves to be refracted upward. He then sets out to find the functional form for the refractive index that would explain the observations.

Unlike the naive observer, we do not seek a "modified" index but try to show that the deduced analysis accurately describes the channel axis displacement for any refractive index.

Brekhovskikh, in an unnumbered equation after his Eq. (40.8), writes

$$k^2 n^2(z) + 2k_m^2 \frac{z}{a} = k^2 n_{mod}^2(z) \quad (B2)$$

in which the wavenumbers  $k$  and  $k_m$  are close and can be canceled on both sides. Introduce into Eq. (B2) the refractive index  $n$  by its velocity ratio equivalent

$$n = \frac{c_0}{c(z)},$$

where  $c_0$  is a fixed reference velocity, close in value to  $c(z)$  over the  $z$ -interval of interest. The radius of the earth is  $a$ , and  $n_{mod}$  is the "modified" refractive index that will, we hope, undo the effects of the earth's curvature.

We conclude from the above, and from our parochial viewpoint, that the effective channel

axis is not where  $c(z)$  is minimum (i.e.,  $n$  is maximum) but where  $n_{mod}$  has a maximum. A necessary condition for this is that its  $z$ -derivative be zero.

Take a  $d/dz$  of (B2) and set it to zero, making use of the fact that  $z/a$  is small while taking the derivative of reciprocals. After dividing by factors that cannot materially affect the zero condition, we conclude that the effective channel axis is where

$$\frac{dc}{dz} = \frac{c_0^2}{c a} \equiv c_0/a. \quad (B3)$$

This is equivalent to Eq. (B1).

*Using the ray invariant (the vertex velocity)*

This second analysis uses the ray invariant (valid only for propagation in a range independent medium) that prescribes, on a flat earth, where the rays have an upper and a lower vertex; it demands that they occur at depths having the same local sound speed, regardless of the sound speed gradient there. On the curved earth, the ray invariant points to other relations.

The ray invariant  $\Sigma$  is defined by (variational principle)

$$\Sigma := \frac{\cos\phi}{c} = \text{const} = \sigma \cos\phi, \quad (B4)$$

where  $\sigma = 1/c$  is the wave "slowness" and  $\phi$  is the elevation angle.

From the constancy of  $\Sigma$  one obtains  $d\Sigma = 0$ , and differentiating (B4) one has

$$\frac{d\sigma}{d\phi} = \sigma \tan\phi. \quad (B5a)$$

Considering the geometry of a path element of length  $ds$ , one obtains

$$\sin\phi = \frac{dz}{ds} = \frac{d\sigma}{ds} / \frac{d\sigma}{dz}. \quad (B5b)$$

The curvature of the ray path is

$$\frac{1}{\rho} := \frac{d\phi}{ds} = \frac{d\sigma}{ds} / \frac{d\sigma}{d\phi}, \quad (B6)$$

which upon substitution of Eq. (B5) becomes

$$\frac{1}{\rho} = \frac{1}{\sigma} \frac{d\sigma}{dz} \cos\phi. \quad (\text{B7})$$

These are generally valid statements for any point of the ray path.

We are interested in a level ray,  $\phi = 0$ , near the channel axis, at a point for which  $1/\rho = -(1/a)$ , and where  $a$  is the local, along-path radius of curvature of the axis (the azimuthally weighted combination of the two principal radii of curvature for the spheroid, decreased by the depth). Equation (B7) now becomes

$$\frac{d\sigma}{dz} = -\frac{\sigma}{a} \quad (\text{B8})$$

and, because the product  $\sigma c = 1$ ,

$$\frac{dc}{dz} = \frac{c}{a}. \quad (\text{B9})$$

This result replicates Eq. (B1), as expected.

UNCLASSIFIED

SECURITY CLASSIFICATION OF THIS PAGE

REPORT DOCUMENTATION PAGE				Form Approved OMB No 0704-0188	
1a REPORT SECURITY CLASSIFICATION Unclassified		1b RESTRICTIVE MARKINGS			
2a SECURITY CLASSIFICATION AUTHORITY		3 DISTRIBUTION/AVAILABILITY OF REPORT  Unlimited			
2b DECLASSIFICATION/DOWNGRADING SCHEDULE					
4 PERFORMING ORGANIZATION REPORT NUMBER(S)  APL-UW TR8929		5 MONITORING ORGANIZATION REPORT NUMBER(S)			
6a NAME OF PERFORMING ORGANIZATION Applied Physics Laboratory University of Washington		6b OFFICE SYMBOL (If applicable)	7a NAME OF MONITORING ORGANIZATION		
6c ADDRESS (City, State, and ZIP Code)  1013 NE 40th Street Seattle, WA 98105-6698		7b ADDRESS (City, State, and ZIP Code)			
8a NAME OF FUNDING / SPONSORING ORGANIZATION  ONR		8b OFFICE SYMBOL (If applicable)  11250A	9 PROCUREMENT INSTRUMENT IDENTIFICATION NUMBER  Grant N00014-89-J-1979		
8c ADDRESS (City, State, and ZIP Code) Office of Naval Research 800 N. Quincy Street Arlington, VA 22217-5000		10 SOURCE OF FUNDING NUMBERS	PROGRAM ELEMENT NO	PROJECT NO	TASK NO
					WORK UNIT ACCESSION NO
11 TITLE (Include Security Classification)  Hamiltonian 3-D Ray Tracing in the Oceanic Waveguide on the Ellipsoidal Earth					
12 PERSONAL AUTHOR(S) J. George Dworski and James A. Mercer					
13a TYPE OF REPORT Technical		13b TIME COVERED FROM _____ TO _____		14 DATE OF REPORT (Year, Month, Day) December 1990	15 PAGE COUNT 77
16 SUPPLEMENTARY NOTATION					
17 COSATI CODES			18 SUBJECT TERMS (Continue on reverse if necessary and identify by block number)		
FIELD	GROUP	SUB-GROUP	Hamiltonian 3-D ray tracing sound speed model oceanic waveguide ellipsoidal earth antarctic circumpolar current		
19 ABSTRACT (Continue on reverse if necessary and identify by block number)  Ray equations based on an acoustic Hamiltonian, and formulated by Jones et al. (1986) for spherical coordinates in NOAA's 3-D ray tracer HARPO, are adapted to ellipsoidal coordinates in the oceanic waveguide. The ensuing modified HARPO is used to model very long range (up to antipodal) acoustic paths in which the difference between geodesics and great circles is measurable. The eventual objective of this modeling is to extract the predictable part of the travel-time trend and fluctuations along several long paths that will be used to monitor hypothetical global warming effects. The requirements for easy assimilation and representation of realistic environmental inputs are discussed. These requirements, when coupled with the possibility of classical chaos in the ray paths, dictate a new software architecture. We use the existing software, however, to breadboard and test features of new ray tracers in the global boundary layer, and to support the experimental design of a forthcoming pilot experiment that will use a transmitter located at Heard Island in the Indian Ocean near Antarctica. A path of particular interest links Heard Island, through the Tasman gap, to the Washington-Oregon Coast in the northeast Pacific. A 3-D sound speed model is formulated for the Indian/Pacific Ocean in the region of this path, and a 3-D antarctic circumpolar current model with 180 Sverdrup transport is specified to cross the path. Eigenrays are computed to within 2 m error on 18 Mm in the presence or in the absence of currents. We draw conclusions specific to the acoustic communication channel on this path. In particular, we infer a significant out-of-(geodesic)-plane deflection (of about 500 km) of the acoustic eigenpaths. This 3-D deflection is due to the thermohaline structure and can be quantified, at the present time, only by ray tracing.					
20 DISTRIBUTION/AVAILABILITY OF ABSTRACT <input checked="" type="checkbox"/> UNCLASSIFIED/UNLIMITED <input type="checkbox"/> SAME AS RPT <input type="checkbox"/> DTIC USERS			21 ABSTRACT SECURITY CLASSIFICATION Unclassified		
22a NAME OF RESPONSIBLE INDIVIDUAL Marshall Orr, Office of Naval Research			22b TELEPHONE (Include Area Code) 703-226-6994	22c OFFICE SYMBOL 11250A	